Universitetet i Stavanger

FACULTY OF SCIENCE AND TECHNOLOGY

MASTER'S THESIS

Study programme/specialization: MSc Petroleum Geosciences Engineering	Spring Semester, 2017 Open
Author: Ushah Ranchod	(Signature of author)
Faculty Supervisor: Wiktor Waldemar Weibull External Supervisor: Olav Inge Frette (*Sharp Reflections*)	
Title of master's thesis: **Comparing AVA character between well derived 3D synthetic models and real seismic together with extended elastic impedance studies of the Agat Formation in the Northern Viking Graben**	
Credits:	
Key Words: Agat Formation North Viking Graben 3D Parametric Modelling Amplitude versus Angle (AVA) Extended Elastic Impedance (EEI)	Number of pages: 112 + supplement material/other: USB Stavanger, 21st June 2017 Date/year

Title page for Master's Thesis
Faculty of Science and Technology

Comparing AVA character between well derived 3D synthetic models and real seismic together with extended elastic impedance studies of the Agat Formation in the North Viking Graben

By

Ushah Ranchod

MSc Thesis

Presented to the Faculty of Science and Technology

University of Stavanger

University of Stavanger

2017

Acknowledgements

This thesis is submitted in partial fulfilment of the requirements for the Master of Science degree in Petroleum Geosciences Engineering. The work has been carried out at *Sharp Reflections* office in Stavanger, Norway.

The author would like to acknowledge *Sharp Reflections* for the use of their *Pre-Stack Pro* software for this thesis. Special thanks to Dr. William Shea, Olav Inge Frette and Morten Sola for their assistance and mentorship. Many thanks to *VNG Norge* and Gisle Mjøen for generously allowing the use of their data. Further thanks to Wiktor Waldemar Weibull for supervising the study on behalf of the University of Stavanger.

Comparing AVA character between well derived 3D synthetic models and real seismic together with extended elastic impedance studies of the Agat Formation in the North Viking Graben

Ushah Ranchod [1]

Department of Petroleum Technology, University of Stavanger, 4036 Stavanger, Norway

Abstract

This thesis provides the first detailed approach to understanding and comparing amplitude variation with angle (AVA) character between well derived 3D synthetic models and real seismic of the Agat sands in wells 35/3-1, 35/3-2, 35/3-4 and 35/3-7 S in the Northern North Sea. It also investigates the sensitivity in AVA behaviour to varying physical parameters such as: porosity, P-wave velocity, mineral bulk modulus and thickness. These were plotted against hydrocarbon saturations where key relationships were observed. Altogether a clear Class IV AVA Top Agat response prevailed when comparing well derived 3D synthetic models against real seismic data, which remained consistent for all fluid substituted brine, oil and gas scenarios. Furthermore, brine saturated sands characteristically showed little to no variation in AVA effect when physical parameters were varied, whereas gas saturated sands were significantly softer with a greater sensitivity to AVA changes. Minor reductions in the P-wave velocity of the overlying shale by as little as 7.5% revealed polarity reversals whereas as a similar increase changed the AVA class from IV to III. Moreover, enhanced porosities created a more prominent AVA class IV response with the same also being true for a reduced mineral bulk modulus scenario or in other words a shaley sand scenario. Extended Elastic Impedance (EEI) volumes were generated and proved to be a predictive tool for extrapolating lithology and fluid effects away from well data. Although sand bodies were identified as relatively isolated, upside potential was identified to the southwest of well 35/3-7 S where undrilled fluid and lithology anomalies prevailed.

Table of Contents

1 Introduction

A large part of Norwegian North Sea exploration has been focused on structural traps, particularly Jurassic fault blocks of the prolific Brent Group. Cretaceous deposits in the Norwegian North Sea have been relatively minor plays for exploration, primarily due to only one significant Lower Cretaceous discovery, the 35/3-2 Agat discovery. However, the recent 36/7-4 Cara discovery by Engie, in Production License (PL) 636, encountered 4-11 MSm^3 of recoverable oil equivalent in the Agat Formation, which has reignited interest in the Lower Cretaceous in the Norwegian North Sea. Furthermore, the proximity of the reservoir fairway to both the Agat discoveries and Gjøa Field, makes the Agat play great for infrastructure-led exploration (ILX). However, the Agat Formation poses geological challenges that can be attributed to several factors: (1) subtle stratigraphic traps; (2) isolated turbidite lobe complexes; (3) thin and shaley sands; (4) poor seismic imaging; and (5) a lack of geophysical understanding. Such complexity makes the Agat play a difficult one to predict. However, if resolved, the potential from unlocking such an under-explored play is significant and one which this thesis begins to unravel, particularly with regards to point (5) above.

Despite a number of offshore exploration wells targeting the Agat Formation for oil and gas over the past three decades and numerous publications on topics such as: lithostratigraphy, stratigraphic models, sedimentary facies and biostratigraphy; there still remains to be no published literature that geophysically assesses the Agat wells and relates their synthetic response and AVA effect to real seismic data. A concise and detailed documentation addressing this point would therefore be greatly beneficial and would assist ongoing Lower Cretaceous exploration in the Norwegian North Sea. Furthermore, such work may also be the catalyst for more detailed geophysical studies on the Agat Formation.

This MSc thesis presents the results obtained from elastic and physical property analysis of several wells targeting the Agat Formation in Block 35/3. The main constituents include a comparison between modelled and well synthetic seismograms to real pre-stack gathers; fluid substitution; and 3D parametric/AVA modelling. The lattermost incorporates 2D plots and gather maps to illustrate how variations in porosity, p-wave velocity, mineral bulk modulus and thickness against hydrocarbon saturation affect the amplitude and AVA response of the Agat Formation. Lastly, Extended Elastic Impedance (EEI) lithology and fluid

cubes were generated to investigate lateral continuity of sands and extent of hydrocarbon accumulations. The results demonstrate a quantitative geophysical workflow for assessing the amplitude and AVA character variation within the Agat Formation and how sensitive these are to varying physical parameters (porosity, mineral bulk modulus, P-wave velocity, thickness and hydrocarbon saturation) using state-of-the-art interpretation tools in *Pre-Stack Pro*; a pre-stack seismic analysis software developed by *Sharp Reflections*.

2 Geological Background

2.1 Location

The study area is located in the Northern North Sea (Norwegian sector) in Block 35/3, PL 884, approximately 60 km's west of the Norwegian coastline (Figure 1a). Two gas/condensate discoveries have been made within the area of interest: the 35/3-2 Agat and 35/3-7 S discovery wells. One block west of the Agat discovery lies the Peon 35/2-1 well – a gas discovery within the Nordland Group. The nearest field is the Gjøa Field located in Block 35/9 approximately 50 km's to the south, which is producing from the Jurassic sands of the Viking, Brent and Dunlin Groups. The study area is located within the Måløy Terrace and is bound to the east by the Øygarden Fault Complex and to the west by a major normal fault bounding the eastern margin of the Sogn Graben (Figure 1b and Figure 2).

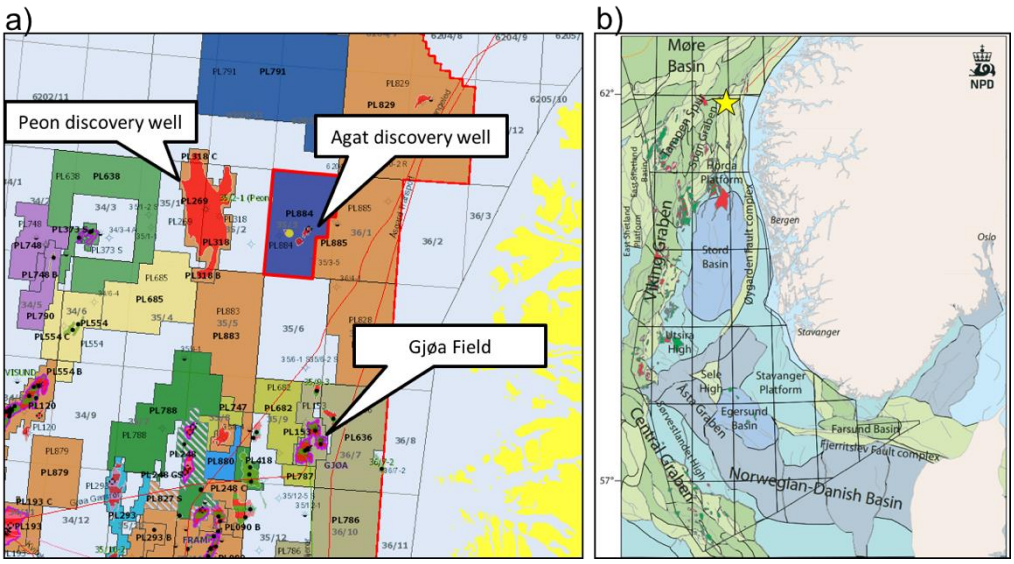

Figure 1: a) Location of study area in Block 35/3. Study area is outlined in red and now includes Production License 884; b) Highlights the location of the study area (marked with a yellow star) in the northern part of the Viking Graben adjacent to the Sogn Graben (*NPD FactPages*).

2.2 Tectonic Events

The North Sea is an epicontinental basin, located between southern Scandinavia and northern Britain and is composed of several Mesozoic sub-basins and highs (Øvrebø et al., 2001). The basic structural framework of the North Sea is mainly the result of Upper Jurassic/Lower Cretaceous rifting. However, to gain an understanding of the Cretaceous development of the North Sea it is important to familiarise with the pre-Cretaceous geological history (Isaksen & Tonstad, 1989).

The first major rift phase for the formation of the North Sea rift occurred in the Late Permian to Early Triassic and relates to the breakup of the supercontinent Pangea (Ziegler, 1975; Badley et al., 1989; Gabrielsen et al., 1990; Færseth, 1996). A second major rift episode occurred in the mid to late Jurassic (Badley et al., 1988; Gabrielsen et al., 1990; Rattey & Hayward, 1993; Færseth, 1996; Færseth & Ravnås, 1998). This is believed to have resulted in the deflation of a central North Sea thermal dome (Ziegler, 1990; Underhill and Partington, 1993, 1994). Collapse of this dome is believed to have exerted regional tension and resulted in the development of the North Sea triple junction (Bell et al., 2014). Most of the major faults active during the Jurassic rifting were probably reactivated faults formed during the earlier rift phase (Badley et al., 1988; Færseth, 1996).

Structural mapping has shown thickness variations within the upper Jurassic syn-rift strata which indicates that during the main Late Jurassic to Early Cretaceous extensional phase, the Måløy Slope was compartmentalised into a series of rotated half-grabens bounded by a series of N-S to NNW-SSE trending normal faults (Gabrielsen et al., 2001). The Early Cretaceous transition from syn-rift to post-rift saw a marked change in the structural configuration of the North Sea basin with a reduction in the rate of normal faulting and a marked increase in basin subsidence. This overall change in structuration combined with ongoing sedimentation resulted in the filling-in and smoothing of the existing rift-related topography (Bugge et al., 2001; Gabrielsen et al., 2001).

The Late Cretaceous has been interpreted as a structurally quiescent period, although it is possible that the Øygarden fault zone was active at this time (Martinsen et al., 2005). A

simplified map and regional geo-section across the Viking Graben, Sogn Graben and Måløy Slope are illustrated in Figure 2.

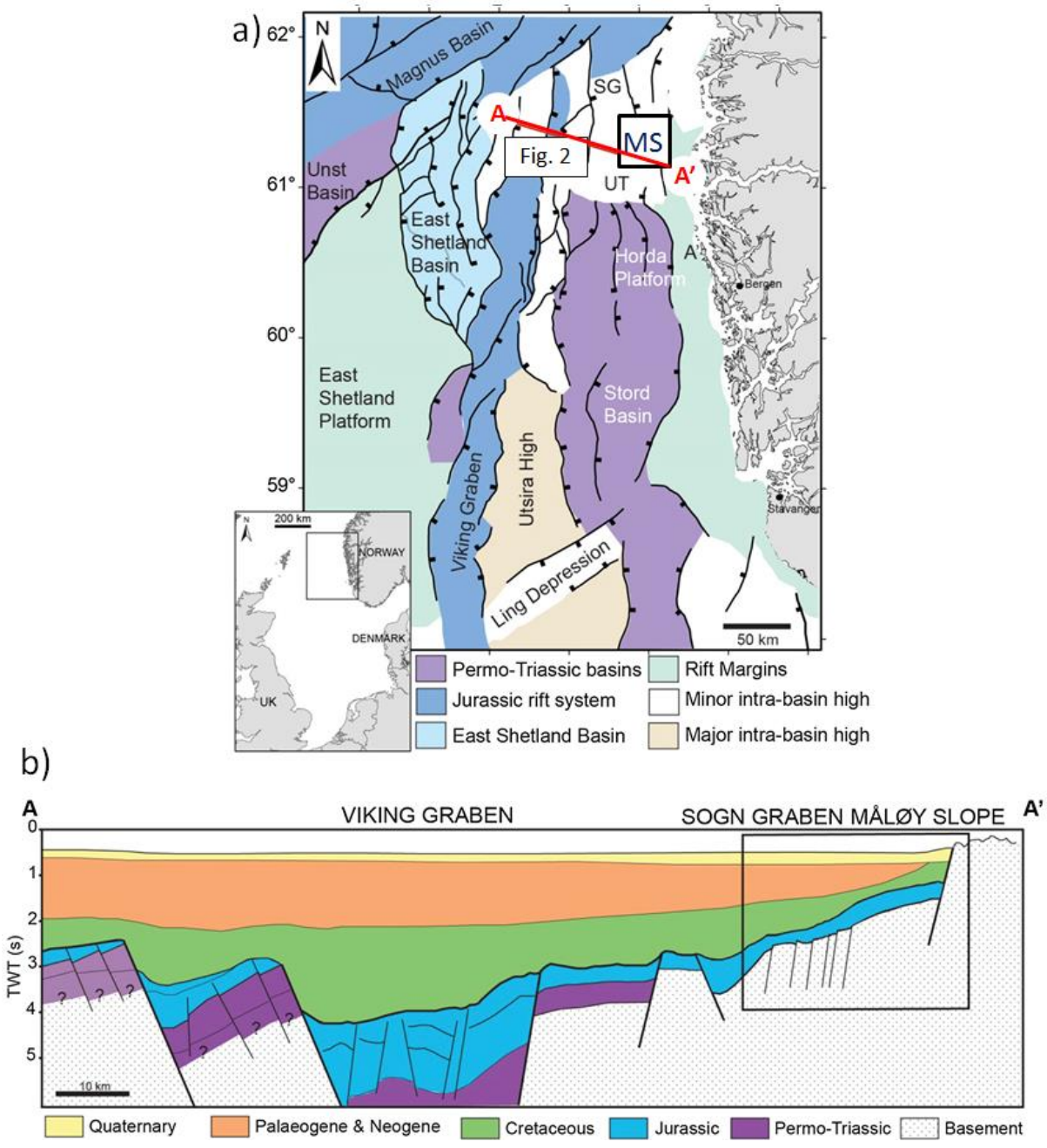

Figure 2: a) Simplified map of the main structural elements of the Northern North Sea, after Færseth et al (1997). MS = Måløy Slope; SG = Sogn Graben; UT = Uer Terrace. Black box indicates the location of the Sogn Graben and Måløy Slope highlighted in Figure 2b. b) Simplified regional W-E geo-section along A-A' across showing the generalized structure of the Viking Graben, Sogn Graben and Måløy Slope. After Reeve et al (2015).

2.3 Depositional Setting

Early Cretaceous deposition in the North Sea was strongly influenced by the basin topography created by Late Jurassic rifting. Western grabens and eastern terraces/highs controlled accommodation, transport directions and available source areas (Martinsen et al., 2005). During the late Early Cretaceous the Måløy Terrace had a low-gradient slope towards the deeper Sogn Graben in the west (Shanmugam et al., 1995; Bugge et al., 2001).

Sediments deposited during the Cretaceous in the Northern North Sea are mainly marls, clays and fine-grained silts. However, distributed on the mud-dominated slope system are several hemi-pelagic sandy mass flow events sourced from the Norwegian hinterland and best known as the Agat Formation that lies within the Lower Cretaceous Cromer Knoll Group and is of Aptian/Albian age (Isaksen & Tonstad, 1989; Skibeli et al., 2005; Nystuen, 1999; Bugge et al., 2001) (see Figure 3).

Few other well cores from the North Sea area have been studied so carefully by so many sedimentologists as the Agat cores. Published and unpublished interpretations of depositional processes and environments vary greatly (Nystuen, 1999). The history of this debate is magnificently documented by Vergara et al (2006) and will now be briefly summarised.

Gulbrandsen (1987) was the first to document a sedimentological model, interpreting the sediments as being transported down-slope from the east through submarine canyons. Since then, core analysis by Shanmugam et al (1994); Shanmugam (1995); and Skibeli et al (1995) resulted in the identification of secondary features such as injected sands suggesting slumping and sandy debris flows on an upper slope setting. However, this has since been rejected by Nystuen (1999), who interpreted the depositional process of the Agat as turbidity currents. Bugge et al (2001) then presented a similar interpretation describing the Agat sands as sandy mass-flow turbidite deposits. Lastly Vergara et al (2006) published 3D bathymetry reconstructions on behalf of RWE DEA as well as palaeoecological interpretations of the Agat, all of which support Bugge et al (2001) and Nystuen (1999) as turbidite sand deposits in an upper bathyal setting.

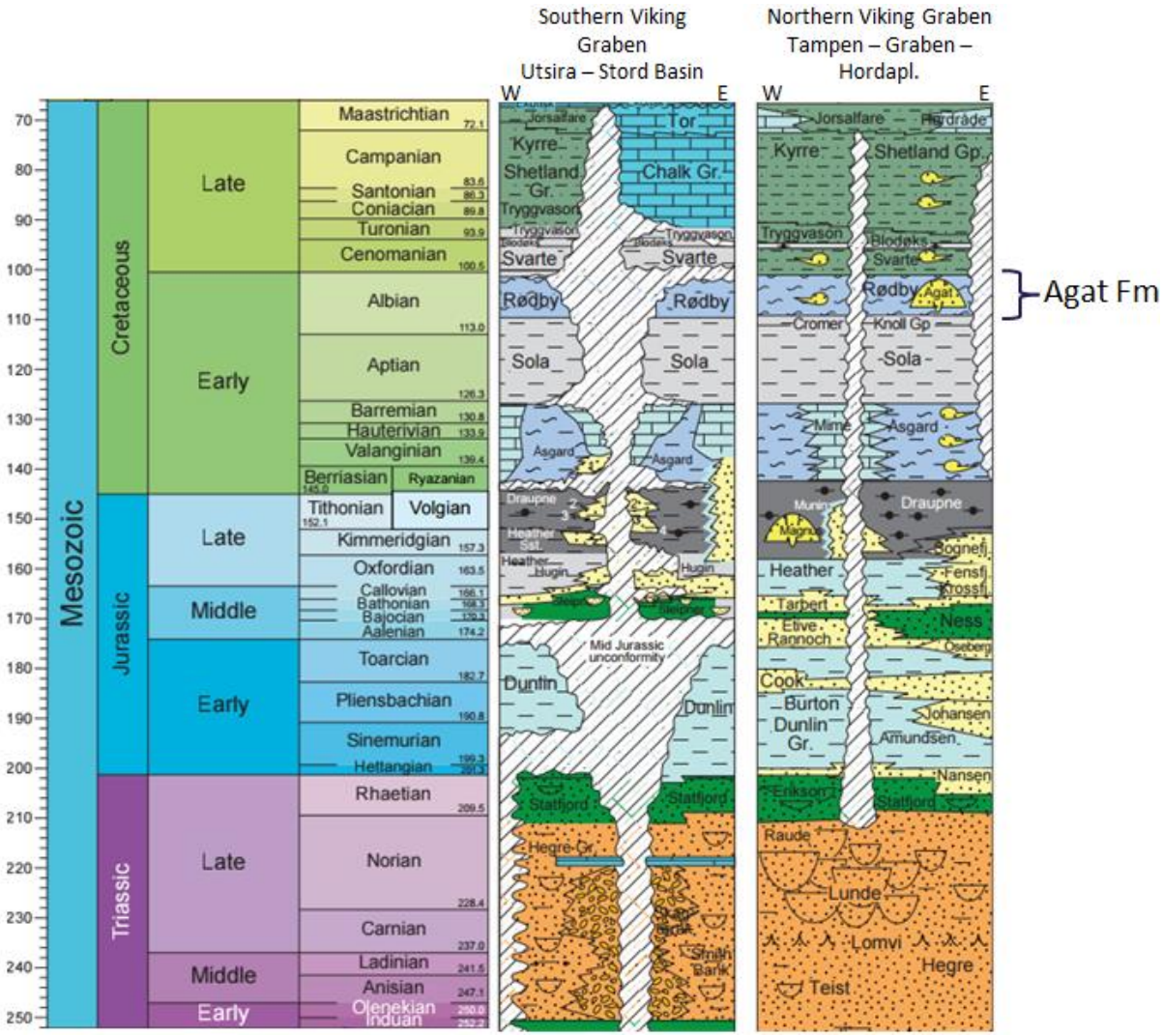

Figure 3: Lithostratigraphy of offshore Norway. The Agat Formation is highlighted. Modified from NPD.

2.4 Exploration History

The Lower Cretaceous is a proven and successful play in the area of interest with a total of 16 wells targeting the Agat Formation, 12 of which are dry and 4 of which are discoveries (35/3-2, 35/3-4, 35/3-7 S, and 35/9-3). Hydrocarbon exploration began in block 35/3 (see Figure 4) with the drilling of wells 35/3-1 (1976) and 35/3-2 (1980), by Saga Petroleum, targeting Jurassic rotated fault blocks as primary targets. Both wells encountered Albian/Aptian sandstones. The unexpected occurrence of hydrocarbon bearing sands in the Cretaceous section led Saga Petroleum to drill well 35/3-4 (1981), which discovered gas bearing sands that were successfully tested. Following this, Saga Petroleum's exploration efforts were less successful with well 35/3-5 (1982) proving weak shows and brine-filled sands with the off-trend well 35/3-6 also being unsuccessful. However, VNG Norge later

proved gas in the Agat reservoir in 2009 with well 35/3-7 S and the more recent 36/7-4 Cara discovery well by Engie further proved the significant potential of the Agat Formation. Looking back on the exploration history it is evident that the Agat Formation has been in and out of the spotlight. It has long been considered as enigmatic with poor seismic imaging and subtle stratigraphic trapping mechanisms being seen as key obstacles, which if overcome can unlock the potential of the Agat Formation. This thesis provides advances in maximising well and seismic data and presents a geophysical approach that anatomises the complexities of the data in order to reconstruct an informative story of the Agat Formation.

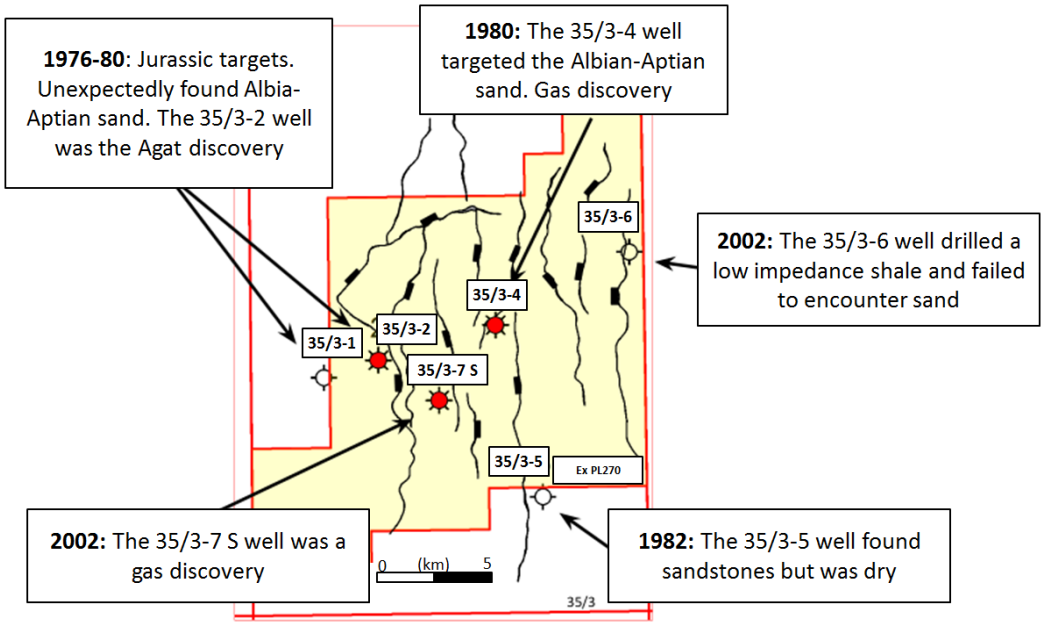

Figure 4: Exploration History of the Agat Formation. Wells 35/3-1, 35/3-2, 35/3-4, 35/3-5 and 35/3-6 were operated by Saga Petroleum, whereas well 35/3-7 S was operated by VNG in what was PL270.

3 Database

3.1 Seismic and Well Data

The 3D seismic dataset utilised over Block 35/3 was the IPN1201 which covers an area of 1066 km^2 and was acquired over the now relinquished PL270. The frequency of the data is approximately 18 Hz and thus the vertical stratigraphic seismic resolution is estimated at around 24 m. The raw offset gathers underwent a series of processing sequences by *Sharp Reflections* that resulted in post-migrated pre-stacked data. This showed an improved alignment of events from near to far offsets, better structural definition within the Agat Formation and a strong noise reduction. The seismic offset gathers were converted to angle gathers in *Pre-Stack Pro* that ranged from 0-35°. From the angle gathers typical stacked near, mid and far volumes were created. A time-slice through the IPN1201 survey along with the position of the studied wells is shown in Figure 5. The American polarity convention has been adopted where a red peak is a "hard" or "positive" event, whilst a blue trough is a "soft" or "negative" event. On a near-offset stack section a "hard" event will correspond to an increase in acoustic impedance with depth, whereas a "soft" event will correspond to a decrease in acoustic impedance with depth.

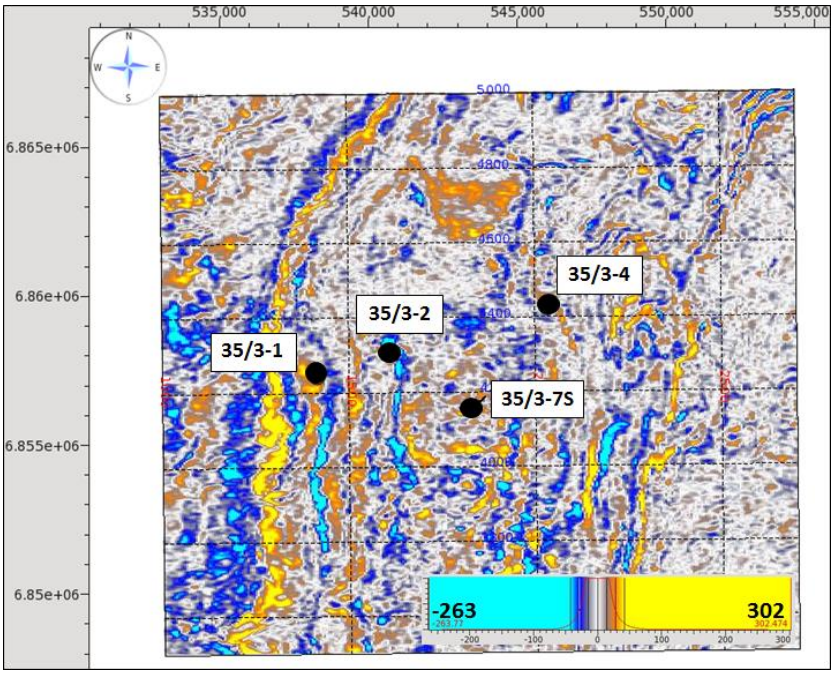

Figure 5: Example time-slice through the IPN1201 survey. The position of the studied wells 35/3-1, 35/3-2, 35/3-7 S and 35/3-4 are also shown.

Four exploration wells were used for the evaluation: 35/3-1, 35/3-2, 35/3-4 and 35/3-7 S (Figure 6). The well log data consists of both standard electrical logging data and lithological mud logs. The log data was provided by VNG Norge who performed their own in-house petrophysical analysis and log quality control. The wireline logs include the gamma ray (*GR*), spontaneous potential (*SP*), density (*RHOB*), neutron (*NEU*), resistivity, and sonic (*DT*). It is important to note that only the 35/3-7 S well contained shear sonic (*DTS*) data. For the other wells, shear-velocity had to be predicted and is further discussed later in *Section 4.3*. Computed petrophysical interpretations (CPI's) from VNG include: volume shale (*Vshale*), effective and total porosity (*PHIE* and *PHIT*, respectively), and water saturation (*Sw*).

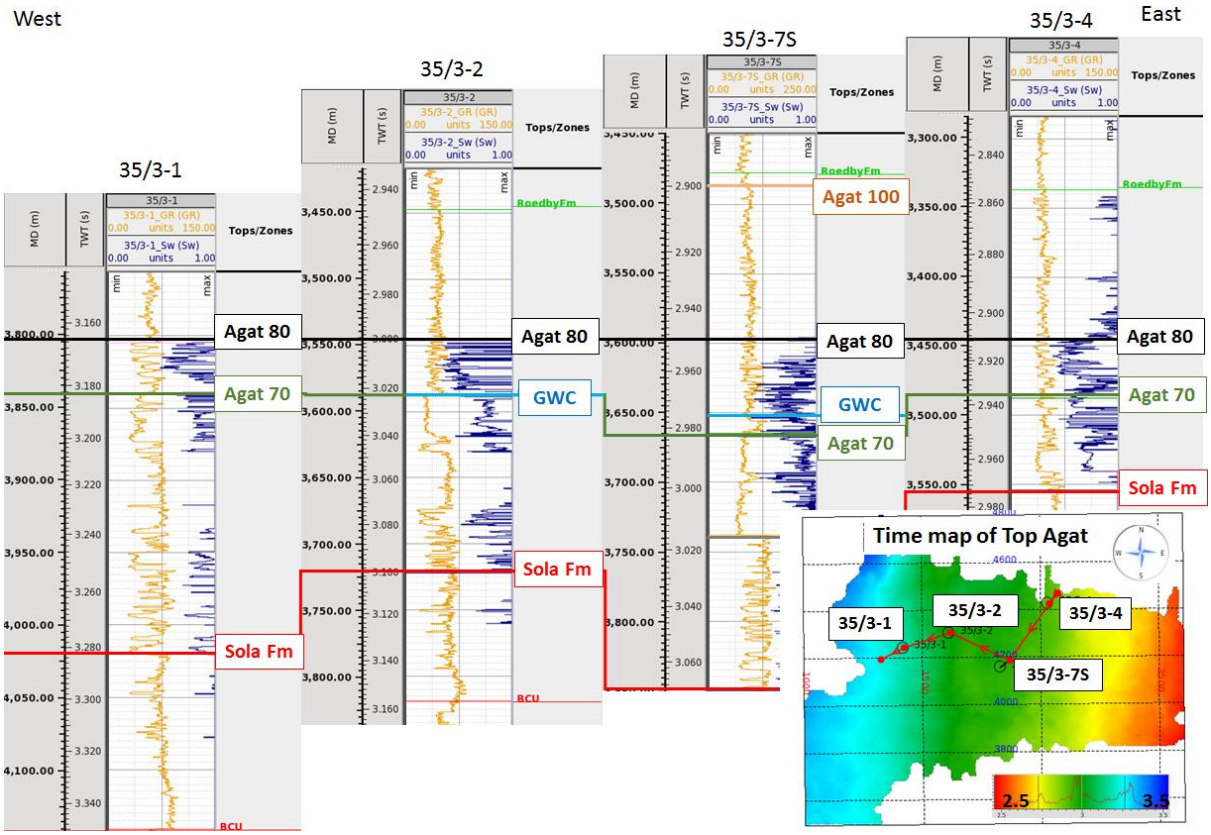

Figure 6: West-East Correlation Panel. Flattened on the Agat 80 Member and highlighting the subdivision of the Agat Formation into various Members as well as the gas-water contacts (GWC) encountered in well 35/3-2 and 35/3-7 S.

Geological horizon picking on the IPN1201 survey was done by VNG. A total of 4 horizons were interpreted: Top Svarte, Top Agat, Top Åsgard and Base Cretaceous Unconformity (BCU). However, to further understand the AVO response of the Agat sands, the Base Agat

was interpreted in *Pre-Stack Pro* as part of this study. The well tops used were also provided by VNG. These differ from NPD tops primarily in the Agat Formation where VNG has subdivided the Agat succession into various members based on seismic reflectors, some of which have geological significance (Figure 7):

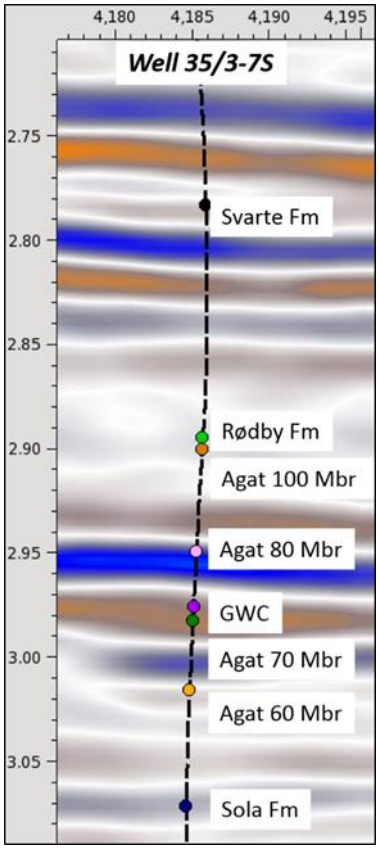

Agat 100 – Youngest sand system

Agat 80 – Main reflector

Agat 70 – Top of clean sands in the well, no reflector

Agat 60 – Base of Agat 70 and transition to shaley sequence

Figure 7: Subdivision of the Agat Formation based on seismic reflectors.

3.2 Seismic Characteristics

To illustrate the seismic characteristics of the Agat Formation in relation to the study wells, a composite seismic section is presented in Figure 8. This shows the Agat Formation and its associated intra Members and gas-water contacts (GWC) along with the Sola Formation, Åsgard Formation and BCU. Figure 8 elucidates the complexity of the seismic facies and lack of defined reflectivity within the Agat Formation. The poor imaging of the Agat Formation therefore makes it challenging to characterise with seismic methods.

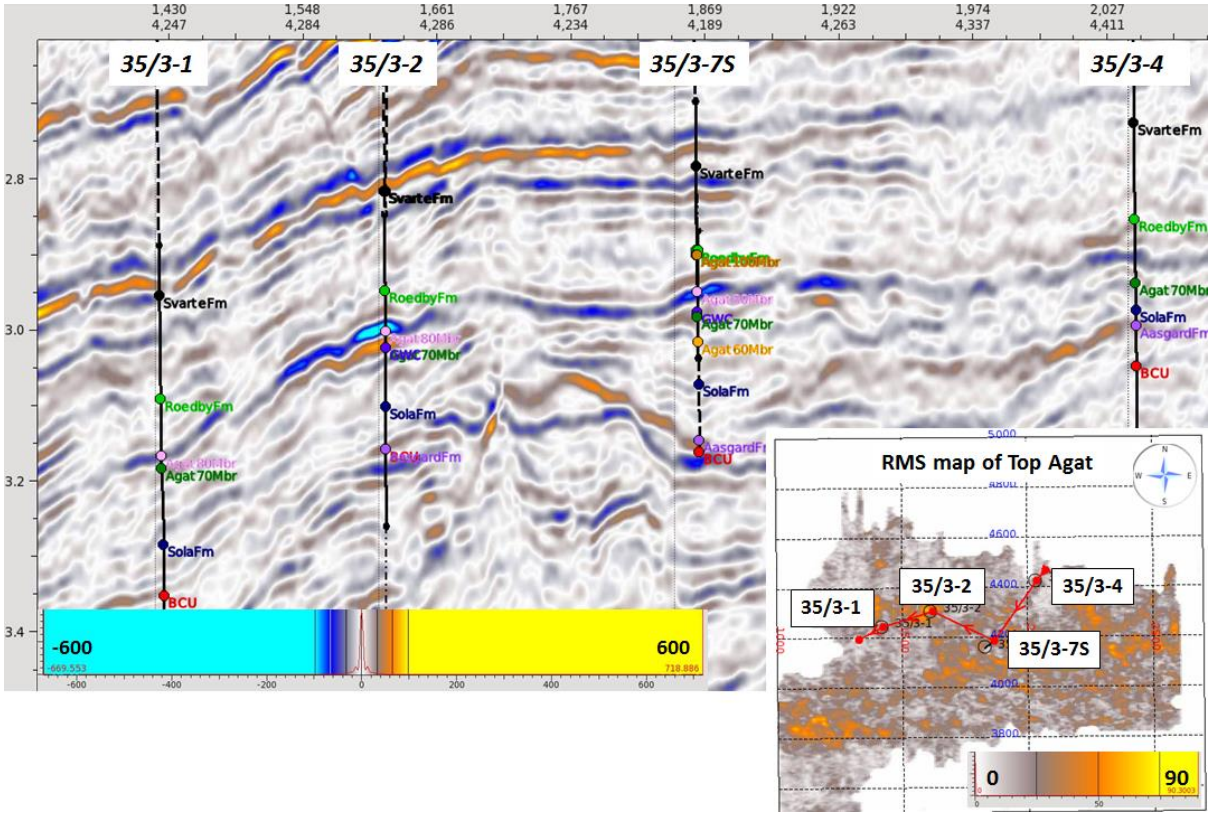

Figure 8: West-East Composite Seismic Section. Showing the complexity and poor quality imaging of the Agat Formation across the studied wells - 35/3-1, 35/3-2, 35/3-7 S and 35/3-4. The insert map displays a RMS amplitude map of the Top Agat Formation along with the composite line and well locations.

3.3 Software

The software used for this thesis was *Pre-Stack Pro* developed by *Sharp Reflections*. *Pre-Stack Pro* is a pre-stack seismic analysis software that enables the combined use of pre-stack visualisation, processing, and interpretation in one platform. The tools used were *Horizon*

tool, Wavelet Tool, Generate Synthetic Gathers, 3D Parametric Synthetic Model Builder, AVO and *Amplitude Maps, Cross-plots, AVA Attributes, Chi Angle Volume and Phase Rotation.*

The focus for the thesis was using the 3D Parametric Synthetic Modelling tool, which is essentially a forward modelling tool with capabilities to incorporate 1D, 2D and 3D modelling aspects as well as fluid substitution (Gassmann or Castagna methods) in the pre-stack domain. The additional dimensions show parametric changes where variables such as density (*Rho*), P-wave velocity (*Vp*), S-wave velocity (*Vs*), porosity (*PHIE* and *PHIT*), mineral bulk modulus (*Kmin*) and thickness, amongst others are changed. This should not be mistaken for modelling 3D geological structure. Intuitive modelling such as varying the *Vp* of the cap rock combined with changing thickness of the reservoir and resultant AVO effects is just one example of the modelling options available to the user. Furthermore, pre-stack wedge models, amplitude maps and pre-stack volumes can be produced which all give insight into the AVA expression and reservoir character that is ultimately the goal of this thesis.

4 Theoretical Framework

4.1 Amplitude versus Offset (AVO/AVA)

Amplitude variation with offset (AVO) or amplitude variation with angle (AVA) has become an essential tool in the petroleum industry for hydrocarbon detection (Rutherford and Williams, 1989). The purpose of AVO analysis is to explain changes in seismic signature in terms of fluid and rock variations (Simm & Bacon, 2014).

4.1.1 Seismic Energy Partitioning

When seismic waves travel through the earth and encounter layer boundaries, having velocity and density contrasts, the energy of any incident wave is partitioned. Figure 9 illustrates this wave partitioning and highlights an important AVO occurrence: the conversion of P-wave energy to S-wave energy.

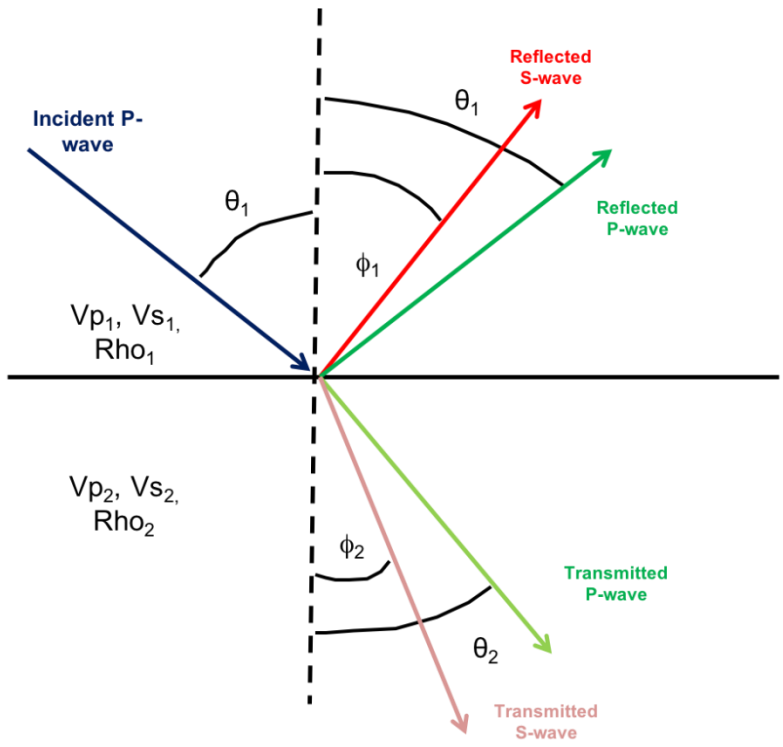

Figure 9: P-wave Partitioning. A P-wave propagating through a medium of density, Rho_1, P-wave velocity, Vp_1, and S-wave velocity, Vs_1, is incident upon an interface with a medium of density, Rho_2, P-wave velocity, Vp_2, and S-wave velocity, Vs_2, at an angle, ϑ_1. Mode conversions occur resulting in reflected P- and S-waves and transmitted (refracted) P- and S-waves. After Castagna and Backus (1993).

The relationship of incident, reflected and transmitted waves at the layer boundary are described simply by Snell's law:

$$\frac{\sin\theta_2}{Vp_2} = \frac{\sin\theta_1}{Vp_1} = \frac{\sin\phi_1}{Vs_1} = \frac{\sin\phi_2}{Vs_2} \qquad \textit{(Eq. 1)}$$

In this equation, θ_1 is the angle of the incident P-wave; it equals the reflection angle of the P-wave. ϕ_1 is the angle of reflection S-wave in medium 1. The angle θ_2 and ϕ_2 are the transmitted angles of the P- and S-waves in medium 2 respectively. The velocities of medium 1 are Vp_1 and Vs_1. In medium 2 the velocities are Vp_2 and Vs_2.

AVO responses vary depending on the physical parameters of the reflection interface (layer boundary) and incidence angle (Shuey, 1985). Analysis of reflection amplitudes as a function of incidence angle can be used to detect changes in elastic properties of reservoir rocks, which may suggest the change in the ratio of P-wave velocity to S-wave velocity (*Vp/Vs*). The change of *Vp/Vs* can be an indicator of fluid saturation changes within reservoir rocks. The fundamental value of AVO analysis is the fact that seismic amplitudes at the boundaries are affected by the the variations of the physical properties across the reflectivity boundary.

4.1.2 Zoeppritz Equation and its Approximation

As discussed in the previous section: when a P-wave hits an interface (e.g. rock-rock boundary), both reflected P- and S-waves, and transmitted (refracted) P- and S-waves are produced (Figure 9). Zoeppritz's (1919) equations determine the amplitudes of these reflected and transmitted waves at the layer boundary between two elastic media and are shown in Equation 2:

$$\begin{bmatrix} R_p\vartheta_1 \\ R_s\vartheta_1 \\ T_p\vartheta_1 \\ T_s\vartheta_1 \end{bmatrix} = \begin{bmatrix} -\sin\vartheta_1 & -\cos\phi_1 & \sin\vartheta_2 & \cos\phi_2 \\ \cos\vartheta_1 & -\sin\phi_1 & \cos\vartheta_2 & -\sin\phi_2 \\ \sin 2\vartheta_1 & \frac{Vp_1}{Vs_1}\cos 2\phi_1 & \frac{\rho_2 Vs_2^{\,2} Vp_1}{\rho_1 Vs_1^{\,2} Vp_2}\cos 2\phi_1 & \frac{\rho_2 Vs_2 Vp_1}{\rho_1 Vs_1^{\,2}}\cos 2\phi_2 \\ -\cos 2\vartheta_1 & \frac{Vs_1}{Vp_1}\sin 2\phi_1 & \frac{\rho_2 Vp_2}{\rho_1 Vp_1}\cos 2\phi_2 & -\frac{\rho_2 Vs_2}{\rho_1 Vp_1}\sin 2\phi_2 \end{bmatrix}^{-1} \begin{bmatrix} \sin\vartheta_1 \\ \cos\vartheta_1 \\ \sin 2\vartheta_1 \\ \cos 2\phi_1 \end{bmatrix}$$

(Eq. 2)

Where R_p and R_s are the reflection coefficients and T_p and T_s are the transmission coefficients for a specific incident angle (ϑ_1). The amplitude of the reflected waves is the product of these reflection coefficients and the incident amplitude.

However, Zoeppritz equations are not the most straightforward and insightful. As a result numerous simplified computations have been developed (e.g. Aki and Richards (1980); Shuey (1985); Hilterman (1990); Smith and Gidlow (1987); and Fatti et al (1994). These approximations allow AVO analysis to be applied without difficulty. However. only the Aki and Richards (1980) and Shuey (1985) will be breifly discussed:

Aki and Richards (1980) introduced a three term approximation for R_{pp} (reflected P-wave). The three terms relate to density, P-wave and S-wave components (Equation 3):

$$R_{pp}(\vartheta) = \frac{1}{2}(1-4Vs^2\rho^2)\frac{\Delta\rho}{\rho} + \frac{1}{2\cos^2\vartheta}\frac{\Delta Vp}{Vp} - 4Vs^2\rho^2\frac{\Delta Vs}{Vs}$$

(Eq. 3)

Where:

$\Delta Vp = ½ (Vp_1 + Vp_2)$

$\Delta Vs = ½ (Vs_1 + Vs_2)$

$\Delta p = ½ (p_1 + p_2)$. Note p is density (Rho).

Shuey (1985) approximation is also a three term equation which uses Poisson's ratio ($\Delta\sigma$) and is derived from Aki and Richards (1980). The equation is given by:

$$R_{PP}(\vartheta) = R_0 + \left[A_0R_0 + \frac{\Delta\sigma}{(1-\sigma)^2}\right]\sin^2\vartheta + \frac{1}{2}\frac{\Delta Vp}{Vp}(\tan^2\vartheta - \sin^2\vartheta)$$

(Eq. 4)

Where:

$\sigma = (\sigma 1 + \sigma 2)/2$

$\Delta\sigma = \sigma 2 - \sigma 1;$

$$A_0 = B - 2(1 + B)\frac{1 - 2\sigma}{1 - \sigma}$$

$$B = \frac{\Delta Vp/Vp}{\Delta Vp/Vp + \Delta\rho/\rho}$$

The approximation is often expressed in a more simplfied form, where *A*, *B* and *C* are known as AVO coefficients:

$$R_{PP}(\vartheta) = A + B\,sin^2(\vartheta) + C(tan^2(\vartheta) - sin^2(\vartheta))$$

(Eq. 5)

The first term *(A)* is the zero angle reflection coefficient (or *Intercept*) related to the contrast of acoustic impedance. The second term *(B)* introduces the effect of shear wave velocity at intermediate angles. It has the effect of amplitude change with offset and is also known as the *Gradient*. Lastly, the third term *(C)* determines the curvature of the amplitude response near to the critical angle.

At intermediate angles, i.e. between *0* and *30°*, the third term of the equation may be dropped, thus leaving a two-term approximation. At large angles beyond *30°*, the third term in the equation becomes more dominant. Shuey's equation played a key role for analysing AVO data for fluid and lithology effects as it's simplicity meant that the regression coefficients for A and B (intercept and gradient, respectively) could be derived easily. In this thesis all three scenarios were tested and displayed similar results (described further in *4.11*), therefore the full Zoeppritz equation was used.

4.2 AVO Classes

In the 1970's, high amplitude anomalies (bright spots) were recognised as gas indicators (Chiburis et al., 1993). However, it was not until 1989 that the classification of AVO sands was first done by Rutherford and Williams (1989). They first classified shale/gas sand interface responses into three types/classes (I, II and III) (Figure 10):

Class I – high impedance sands (i.e. the sand impedance is larger than the shale impedance), together with a negative AVO gradient, so that the reflection coefficient is positive and decreases with angle (dimming with offset/angle).

Class II - responses have small normal incidence reflection coefficients (which may be positive or negative) with a negative gradient so that the AVO effect leads to a large negative reflection coefficient at far offsets. Ross and Kinmann (1995) suggested that the small positive normal incidence coefficient Class II responses, which become negative with offset, be termed Class IIp. In this case, a phase reversal occurs.

Class III – low impedance sands and a negative gradient, leading to increasing amplitude with angle (bright spots).

Class IV - A further class of AVO, Class IV, was introduced by Castagna and Swan (1997) who showed that gas saturated sands can produce various AVO behaviours depending on the overlying shale properties. Class IV has a large negative normal incidence reflection coefficient and overall decreasing amplitude with offset (Figure 10).

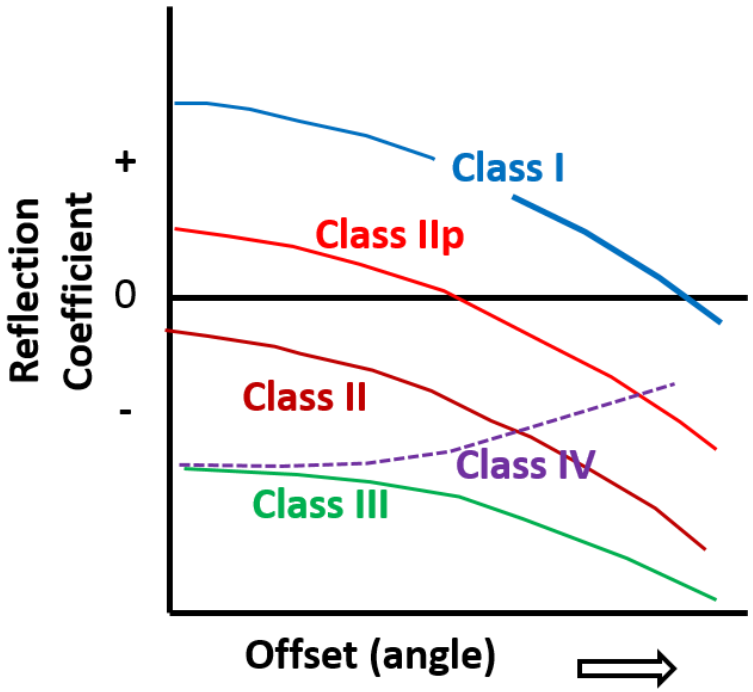

Figure 10: Amplitude vs. Offset (AVO) classifications. Adapted from Rutherford and Williams (1989).

A further summarization of this is highlighted in Table 1 which shows typical seismic reflectivity and AVO behaviors for the various classes.

Class	Seismic Reflectivity	Amplitude vs. Offset
I	Higher than overlying unit	Decreases
II	Approximately the same as the overlying unit	Increases or decreases; may change sign (IIp)
III	Lower than overlying unit	Increases
IV	Lower than overlying unit	Decreases

Table 1: AVO class characteristics.

4.2.1 Introducing the Intercept vs. Gradient Cross Plot

Whilst Figure 10 gives a nice visualisation of AVO responses it does not take into account the multitude of responses from seismic data (Simm and Bacon, 2014). These limitations are overcome by plotting intercept versus gradient on an AVO cross plot (Castagna and Swan, 1997). As a reminder, the terms Intercept (*A*) and Gradient (*B*) were introduced previously in *section 4.1.2.*

The intercept and gradient are very useful products for seismic analysis. Amplitude versus offset (AVO) interpretation may be facilitated by cross plotting the AVO intercept (*A*) and gradient (*B*) (Castagna and Swan, 1997) as highlighted in Figure 11. In general, brine-saturated sandstones and shales will plot on a well-defined "background" trend in the *A*-*B* plane. Deviations from this background trend may be indicative of hydrocarbons or lithologies with anomalous elastic properties. However, oil or gas sands can exhibit a variety of AVO behaviours as discussed above.

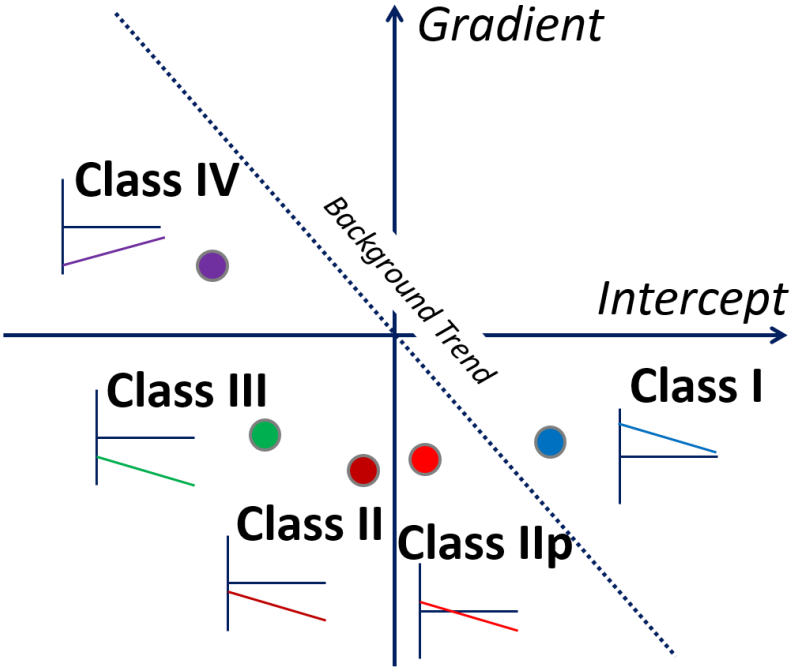

Figure 11: Hydrocarbon sand classifications. Adapted from Castagna and Swan (1997).

4.3 Shear Wave Prediction

Although log measured shear-velocity (*Vs*) is commonly recorded today, this is not always the case. Many of the wells in this study date back to the 1980's and only one well, the 35/3-7 S, contains recorded *Vs* data. As a result, shear-velocity had to be predicted for the remaining wells. An accurate prediction is of utmost importance for a robust AVO analysis to be later achieved since *Vs* is a key parameter controlling the dynamic response characteristic of AVO behaviour. Fortunately, there is usually a strong lithology dependent, but pressure independent, positive correlation between compressional (*Vp*) and shear (*Vs*) velocity (Castagna et al., 1985).

A common method for calculating absent shear-velocity data is by using the Greenberg and Castagna (1992) equations. Their empirical equations are based on a variety of data types from the Gulf Coast and onshore United States where four trends were identified:

Sandstones: $Vs = 0.8042Vp - 0.8559$

Limestones: $Vs = 0.0551Vp^2 + 1.016Vp - 1.0305$

Dolomites: $Vs = 0.58321Vp - 0.07775$

Shales: $Vs = 0.7697Vp - 0.8673$ (*Eq. 6*)

However, these equations are only viable for brine sands and are therefore valid for wells 35/3-1 and 35/3-4. A modified Biot-Gassmann's method (Lee, 2008) was used for the 35/3-2 discovery well. This is the same method as the Greenberg and Castagna (1992) method but in this case the hydrocarbon component of the input *Vp* log is removed using Gassmann's (1951) equation. The *Vs* prediction is next performed using the Greenberg-Castagna method on the now brine saturated *Vp* log. Finally, the original hydrocarbon component is added to the predicted brine saturated *Vs* log. It is important to note that the *Vs* prediction was performed in-house by VNG Norge, although this was thoroughly quality controlled as described later in section 5.2.

4.4 Gassmann's Fluid Substitution

Rock physics is an essential link connecting seismic data to the presence of in situ hydrocarbons and reservoir characteristics (Han & Batzle, 2004). Modelling the effects of fluid on rock velocity and density is a method used to ascertain the influence of pore fluids on seismic data. Gassmann's (1951) equations are the relations most widely used to calculate seismic velocity changes resulting from different fluid saturations in reservoirs. These equations predominate in the analysis of direct hydrocarbon indicators (DHI), such as amplitude "bright spots", amplitude variation with offset (AVO) and time-lapse reservoir monitoring (Han & Batzle, 2004).

The seismic response of reservoirs is directly controlled by compression (P-wave) and shear (S-wave) velocities *Vp* and *Vs*, respectively along with densities. However, neither P- nor S-wave velocity is the best indicator of any fluid saturation effect because of the coupling between P- and S- waves through the shear modulus and bulk density (see explanation by Han & Batzle, 2004). Bulk modulus is far more sensitive to water saturation. As a seismic wave propagates through a rock, which contains pore fluid, bulk volume deformation is produced which results in a pore volume change causing a pressure increase in pore fluid (water). This induced pore pressure resists the compression of the rock as the wave passes causing an increase in rock frame stiffness and an increase in bulk modulus.

Gassmann's equations (Equation 10) provide a simple model for estimating the fluid saturation effect on bulk modulus.

$$\frac{K_{sat}}{K_m - K_{sat}} = \frac{K_{dry}}{K_m - K_{dry}} = \frac{K_f}{\Phi(K_m - K_f)}$$

(*Eq. 10*)

Gassmann's equation estimates saturated bulk modulus (K_{sat}) through the bulk modulus of the forming minerals (K_m), the bulk modulus of the frame or dry rock (K_{dry}), the bulk modulus of the fluid (K_f) and the rock porosity (ø) (Gassmann, 1951).

Calculating fluid substitution on the density and shear log is relatively simple:

$$\rho_{b2} = \rho_{b1} - (\Phi \rho_{f1} - \rho_{f2})$$

(*Eq. 11*)

Where ρ_{b1} is the initial rock bulk density, ρ_{b2} is the bulk density after fluid substitution, ρ_{f1} is the initial fluid density, ρ_{f2} is the density of the substituting fluid, and ø is the porosity.

Given the fact that shear modulus μ is independent of pore fluid, the substituted *Vs* depends only on the change in density:

$$Vs_{sat} = \sqrt{\frac{\mu_{sat}}{\rho_{sat}}}$$

(*Eq. 12*)

Where $V_{S\,(sat)}$ is the saturated shear wave velocity, ρ_{sat} is the saturated density of the rock and μ_{sat} shear modulus.

Calculating fluid substitution on the compressional wave velocity *Vp* log is not as straightforward as it is dependent upon the substituted density (ρ_{sat}), shear modulus (μ_{sat}) and saturated bulk modulus (K_{sat}):

$$Vp_{sat} = \sqrt{\frac{K_{sat} + \frac{4}{3}\ \mu_{sat}}{\rho_{sat}}}$$

(*Eq. 13*)

However, it is important to remember that there are some key assumptions in the Gassmann model (Wang & Nur, 1992; Figure 12).

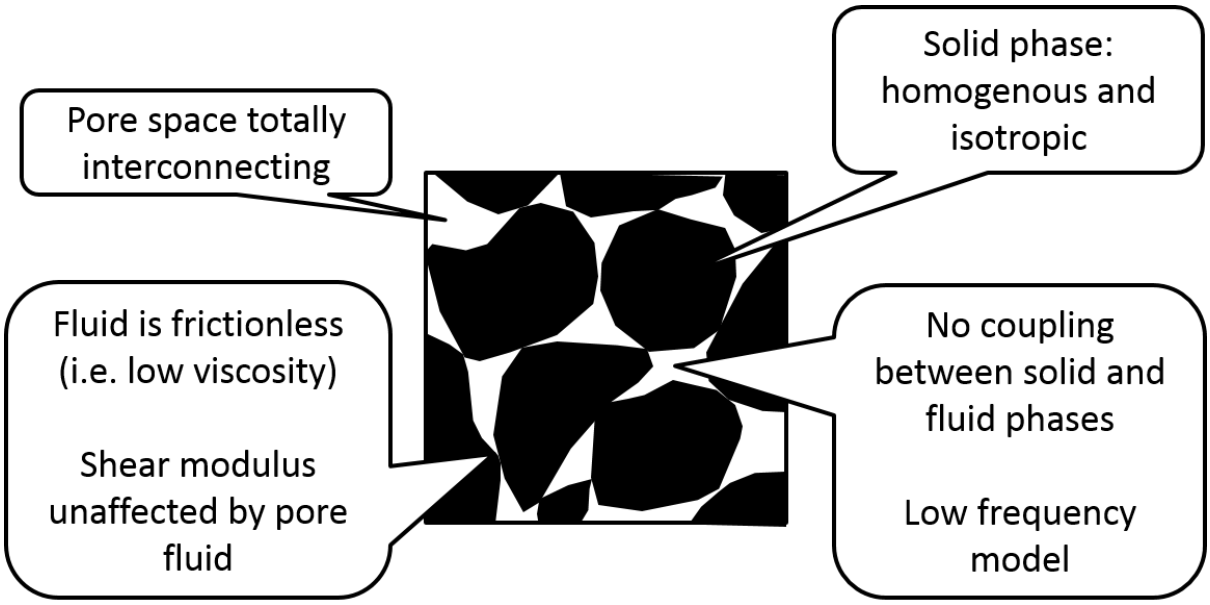

Figure 12: Key Gassmann fluid substitution assumptions. Modified from Wang and Nur (1992).

- The solid is homogeneous and isotropic
- All the pore space is in communication
- Wave-induces pressure changes through the pore space have time to equilibrate during a seismic period (low-frequency assumptions). In other words, wavelengths that are very large compared to the pore spaces
- The fluid that fill the pore space is frictionless (i.e. low viscosity)
- No coupling between solid and fluid phases

4.5 Batzle and Wang Fluid Property Calculation

Pore fluids strongly influence the seismic properties of rocks for e.g. a reservoir containing very light oil with a high gas-oil-ratio may give a different amplitude anomaly or AVO effect than heavy, low GOR oil. Therefore, understanding pore fluid properties is essential for examining seismic data more effectively.

When performing Gassmann's fluid substitution, the fluid properties of brine and hydrocarbons needs to be determined and can be achieved by using the Batzle and Wang (1992) equations. The Batzle and Wang (1992) fluid property model uses a combination of thermodynamic relationships and empirical trends to predict the effects of pressure, temperature and composition on seismic properties of fluids. Their models examine the properties of gases, oils and brines, the three primary types of fluids in most reservoirs. The fluid properties predicted are velocity, density and bulk modulus, which are estimated from the following input parameters:

- Reservoir temperature (°C)
- Reservoir pressure (bar)
- Water salinity (ppm)
- Gas-oil-ratio (GOR)
- Gas gravity
- Oil gravity (g/cm^3)

In this study the input parameters were taken from the publicly available completion reports of the Agat and Gjøa discovery wells and are summarised in Table 2:

Well	Field	Test	Fluid	GOR (Sm^3/Sm^3)	Gas Gravity	Cond. Gravity (g/cm^3)	Oil Gravity (g/cm^3)	Water Salinity (ppm)
35/3-4	Agat	DST 1	Gas/Cond		0.62	0.77		
35/3-2	Agat	DST 1	Gas/Cond		0.62	0.81		9000
35/9-1	Gjøa	DST 1	Oil	284	0.705		0.815	
	Gjøa	DST 2	Gas/Cond	3014	0.681		0.728	
	Gjøa	DST 3	Gas/Cond	5098	0.705		0.749	
35/9-2	Gjøa	DST 1	Oil	714	0.608		0.826	
	Gjøa	DST 2	Gas/Cond	4276	0.668	0.72		
	Gjøa	DST 3	Gas/Cond	3897	0.664	0.732		
	Gjøa	DST 4	Gas/Cond	4717	0.664	0.726		

Table 2: Fluid property summary of the Agat discovery wells and Gjøa Field. Data sourced from publicly available completion reports. Gas, condensate and oil gravities are all at reservoir conditions.

An assumption of the Batzle and Wang (1992) equations are that they are only suitable for gases and oils in the range of 15-40 API, which is perfectly suitable for this thesis (Table 2). For the sake of brevity, a detailed presentation of the equations will be omitted.

4.6 Tuning Effect on the AVO Response

A recurrent challenge encountered when interpreting seismic data is vertical resolution. When two closely spaced features can be distinguished from each other they are said to be resolved (Sheriff, R.E, 1991). The aim for obtaining good resolution seismic, particularly in the petroleum industry, is to define true geological features such as faults and sand beds to enhance prospectivity of the area (Sheriff, 1997; Brown, 2011). However, it is the deeper targets that are affected the most by poor resolution due to a loss of high frequencies with depth as shorter wavelengths are attenuated first (Brown, 2011). It is then important to consider that it is not only hydrocarbons that are contributing to thin-bed amplitude anomalies but variations in bed thickness (Simm, 2009).

Seismic vertical resolution is described as the minimum bed thickness, in other words where the top and base of a bed is distinguishable (Sheriff, 1997). A general guide for estimating seismic vertical resolution is the Rayleigh limit of resolution which reveals that layers are discernable at ¼ of the dominant wavelength (Widess, 1973; Sheriff, 1997). However, dependent on the embedded wavelet, discrete events can be detected below the tuning thickness (Simm and Bacon, 2014). Processes such as deconvolution and frequency filtering aid in the enhancement of seismic imaging and removal of composite effects.

Widess (1973) developed the concept of the wedge model to advance our understanding of amplitudes of reflection events of a bed as it thins below the tuning thickness. The wedge model is based on a hypothetical thinning bed with equal but opposite reflection coefficients at the top and the base. With a decrease in bed thickness amplitudes begin to interfere until a ¼ wavelength where maximum constructive interference is observed known as amplitude tuning or tuning thickness (Cooper et al., 2007). Furthermore, Widess demonstrated that below ⅛ of a wavelength the amplitude and bed thickness displays a linear relationship. The simple wedge model is most applicable where a low-impedance sand encased in shale exists (Figure 13a) but note that it is also wavelet dependent (Simm,

2009). When the sand thickness is thin, analyzing the seismic loops will result in an overestimation of its thickness but when it is above the tuning thickness can result in a slight underestimation (Widess, 1973). The tuning curve in (Figure 13b) demonstrates how the trough-peak composite amplitudes will change with real sand thickness variation as well as apparent sand thickness variation. The graph also shows that maximum amplitude occurs when peak and trough separation is constant after which a thinning sand correlates to a decrease in amplitude. Considering the complexity of geological features, the wedge model and its simplified interference effects are most likely to represent isolated homogenous sand bodies (Simm, 2009) but as seen later in this thesis the interbedding of sandy and shaley layers may add to a convoluted outcome.

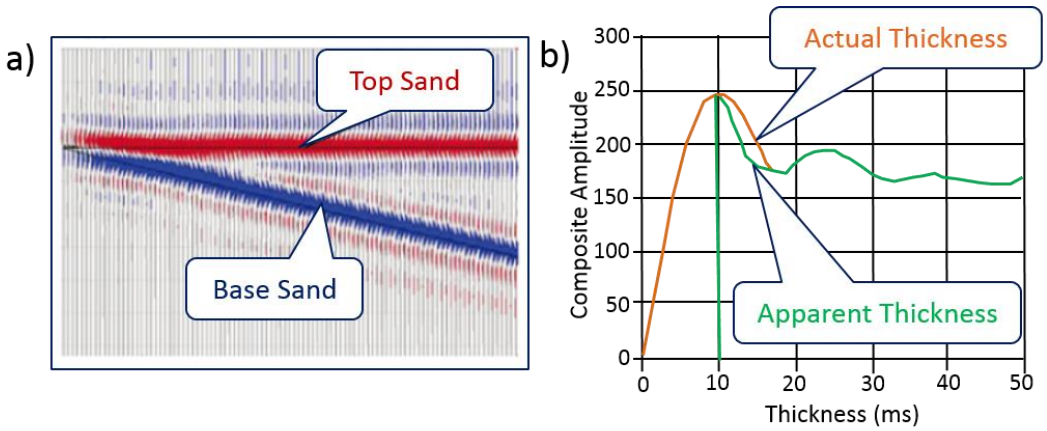

Figure 13: Wedge Model. a) 2D reflectivity display; b) cross plot of thickness versus composite amplitude. Adapted from Simm (2009).

4.7 Extended Elastic Impedance (EEI)

Extended Elastic Impedance (EEI) described by Whitcombe et al (2002) was introduced to improve the limitation on the Elastic Impedance (EI) theory (Connolly, 1999) for rock property predictions. Connolly's (1999) EI theory is a generalization of acoustic impedance for variable incidence angle and is based on the 2-term AVO equation:

$$EI(\vartheta) = Vp^{a} V_S^{b} \rho^{c} \qquad (Eq.7)$$

Where,

$\mathbf{a} = 1 + tan^2\theta$; $\mathbf{b} = -8(V_S/V_P)\, sin^2\vartheta$; and $\mathbf{c} = 1 - 4(V_S/V_P)^2 sin^2\vartheta$

The introduction of EI meant that elastic impedance could be calculated at any angle of incidence not just at zero offset. Connolly (1999) also noticed that at some other angle, EI correlates with rock physics and petrophysical properties. However, the problem with EI is that it does not scale correctly for different angles. Secondly EI is only valid over the 0-30° angle range, even though mathematically it is valid up to 90° (0-1 for $sin^2\vartheta$).

The limitations of EI were overcome by Whitcombe (2002) who modified the equation by normalizing with average values of *Vp*, *Vs* and *Rho* (ρ). This allowed visual comparisons to be made easily between EI logs calculated at different values and thus eliminated the scaling problem. Furthermore, Whitcombe et al (2002) extended the 0-30° angle range to -90°and +90°, hence the name Extended Elastic Impedance. This may sound complicated but it is done rather simply by replacing $sin^2\vartheta$ with a new function, $tan\chi$. The variable ϑ is now a new function called χ (chi angle). The EEI equation is expressed as:

$$EEI(\chi) = Vp_0\rho_0\left[\left(\frac{Vp}{Vp_0}\right)^p\left(\frac{Vs}{Vs_0}\right)^q\left(\frac{\rho}{\rho_0}\right)^r\right] \qquad (Eq.8)$$

where,

p = $cos\,\chi + sin\chi$

q = $-8k\,sin\chi$

r = $cos\,\chi - 4k\,sin\chi$

Vp_0, Vs_0, and ρ_0 are normalisation constants.

For reflectivity data (seismic), relative EEI can be defined using intercept and gradient which are the seismic intercept and gradient traces with -90° phase rotation applied. In terms of intercept (*A*) and gradient (*B*), relative EEI can be written as (Whitcombe et al., 2002):

$$EEI(\chi) = A + B\,tan(\chi) \qquad (Eq.\ 9)$$

EEI can be viewed as the perpendicular distance from a point to a straight line defined by χ. EEI logs are a step ahead of reflectivity EEI in that they proved a means of calibrating well to seismic data. It is of great use to the petroleum industry as the chi angle can be selected to

optimise the correlation of the EEI curves with petrophysical parameters such as shale volume, water saturation and porosity or with elastic parameters such as bulk modulus, shear modulus and lamé etc. (Whitcombe et al., 2002). EEI logs can be calculated using the EEI equation (Equation 9) for specific chi angles that correspond to petrophysical parameters of interest. Real logs and EEI logs can be compared and if a good match exists then EEI volume attributes can be generated and used as a tool for exploration.

5 Methodology and Results

5.1 Proposed Workflow

A proposed workflow is suggested in Figure 14, which encapsulates the step-by-step methodical approach behind this thesis. The dark blue boxes illustrate the work done as part of this thesis, whereas the light blue boxes highlight the work done by *VNG* Norge and *Sharp Reflections* prior to this thesis. The main parts of this workflow and the results will now be discussed in this chapter.

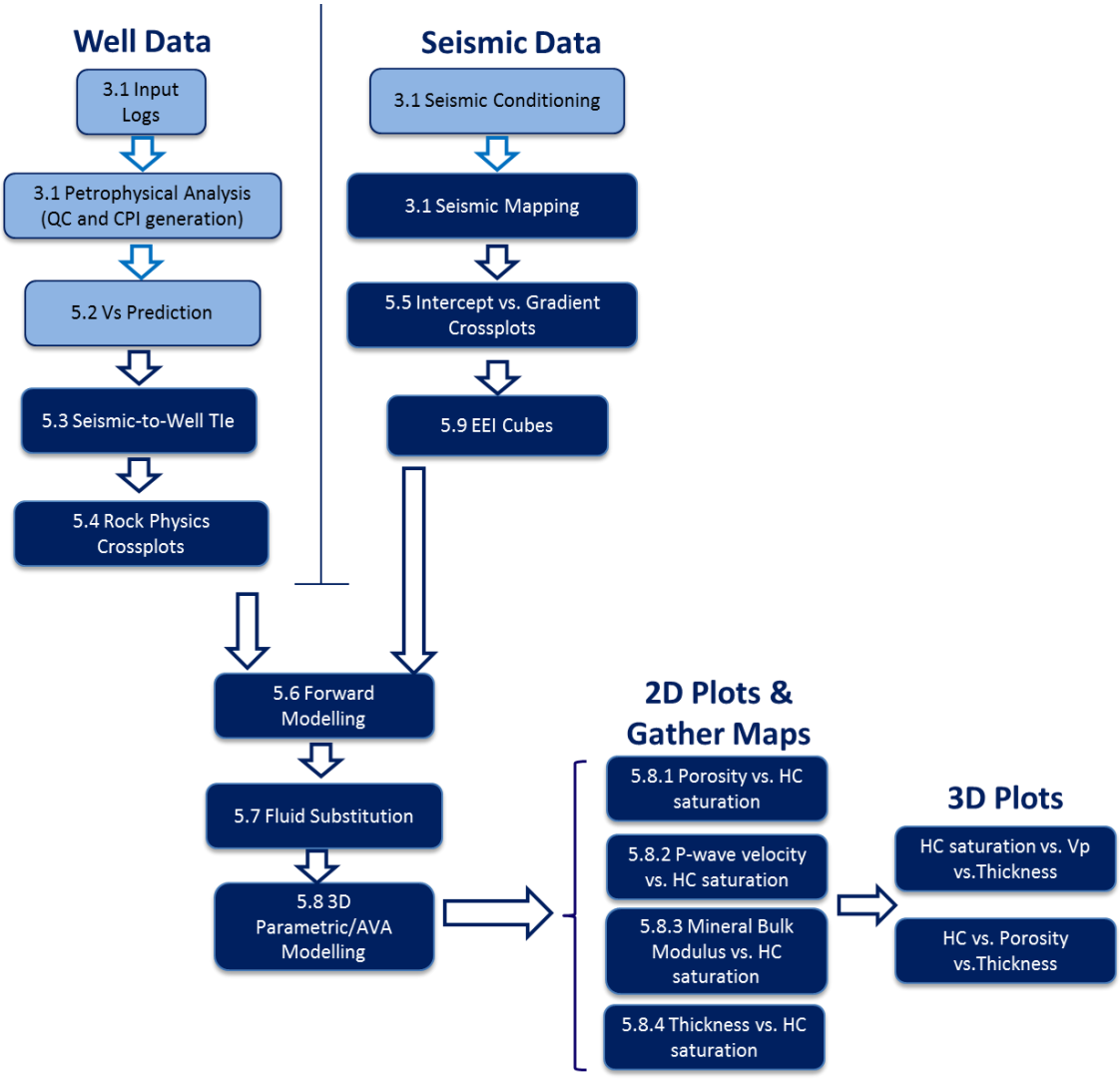

Figure 14: AVA Modelling Workflow. Light blue boxes highlight the work already done by VNG Norge and Sharp Reflections prior to this thesis. Dark blue boxes show the work done as part of this thesis. Section numbers are indicated within each workflow box for the readers' reference.

5.2 Shear Wave Prediction Quality Control

Since an accurate prediction of shear wave velocity is of great importance for a robust AVO analysis to be later achieved, it was deemed necessary to quality control the prediction done by *VNG Norge*. As *Pre-Stack Pro* is not a petrophysical software and *VNG Norge* performed their own petrophysical analysis and shear wave prediction, Excel was used to quality control the *Vs* logs. The method implemented was Greenberg and Castagna's relations for sandstone and shale as described in the Theoretical Framework section. This method is applicable in areas where the *Vp* is >2.6 km/s. The approach was rudimentary but nonetheless served the purpose. A feasible assumption is that VNG Norge would have applied modified Gassmann's method for hydrocarbon-bearing zones in some of the wells.

Well 35/3-7 S is the only well that contains measured Vs data and so therefore was the starting point. A Vp vs. Vs plot was created from log data for each formation and member and then a best fit linear line (black) fitted through the data points. On the same plots, Greenberg and Castagna's coefficients were used to create a linear line relationship (red) for both sandstones of the Agat 70 Member and shales of the Sola Formation (Figure 15):

- Sandstones: Vs = 0.8042Vp – 0.8559
- Shales: Vs = 0.7697Vp – 0.86735

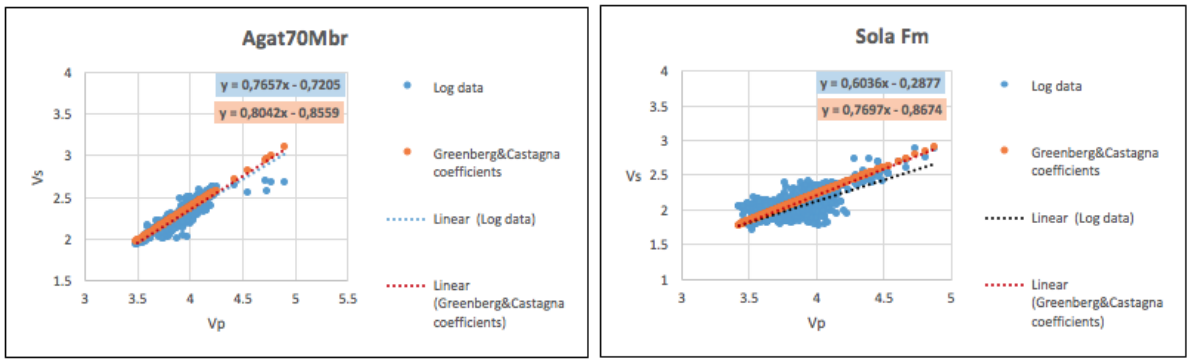

Figure 15: Vp versus Vs cross plots for well 35/3-7 S for the Agat 70 Member and Sola Formation. A trend line was created using the Greenberg & Castagna coefficients where a close match to the real log data was observed.

The cluster of outlier points is likely attributed to gas zones of the Agat 70 Member of well 35/3-7 S. Overall there is a good match between real data coefficients and that of Greenberg and Castagna's coefficients but they are not expected to be identical since

formations are not pure lithologies. The modelled brine substituted log data for well 35/3-7 S was also plotted and the coefficients extracted by fitting a trend line through the data points and later compared to other wells. In addition, Greenberg and Castagna's relations using fractions was tested. The idea is similar to the previous equations except volume fractions are specified in order to introduce a mixture of lithologies. Many sand shale mixtures were evaluated for each formation but as Figure 15 shows the trend line (grey) consistently lies to the top left out with the log data points.

$$V_S = \frac{1}{2}\left\{\left[\sum_{i=1}^{L} X_i \sum_{j=0}^{N_i} a_{ij} V_P^j\right] + \left[\sum_{i=1}^{L} X_i \left(\sum_{j=0}^{N_i} a_{ij} V_P^j\right)^{-1}\right]^{-1}\right\}$$

$$\sum_{i=1}^{L} X_i = 1$$

where

L	number of monomineralic lithologic constituent
X_i	volume fractions of lithological constituents
a_{ij}	empirical regression coefficients
N_i	order of polynomial for constituent i
V_p, V_s	P and S wave velocities (km/s) in composite brine saturated, multimineralic rock

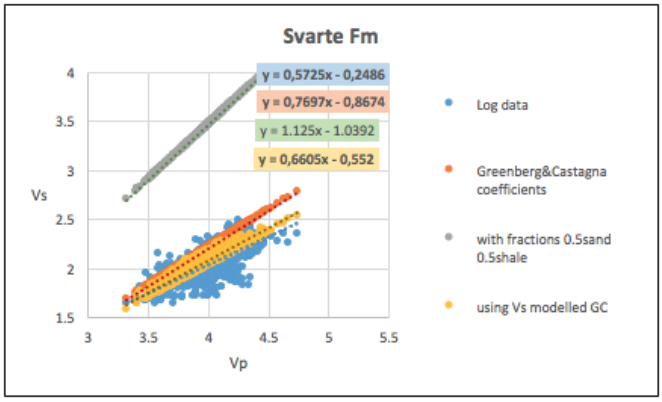

Figure 16: Greenberg and Castagna method using fractions for the Svarte Formation in well 35/3-7 S. This proved unsuccessful as predicted points in grey plot to the top left, far from the well log data.

Well 35/3-1 is a dry well and a similar quality control approach was done where log data was plotted and fitted with a best fit linear line (red) (Figure 16). The brine coefficients from the trend line of well 35/3-7 S were then used to fit a line (black) in the 35/3-1 well data points for the corresponding formations to see if a match existed. For most of the formations, the trend lines of the well 35/3-7 S brine coefficients and the other wells brine coefficients are in close range of each other and indicate sandstone and shale properties are similar across all the wells. For brevity, only the selected plots are shown but the same method was applied to all wells. In conclusion, a close correlation was found between the predicted *Vs* logs using the 35/3-7 S brine Greenberg and Castagna coefficients and VNG Norge's actual *Vs* estimations. Thus, the quality control proved the *VNG's Vs* prediction was robust.

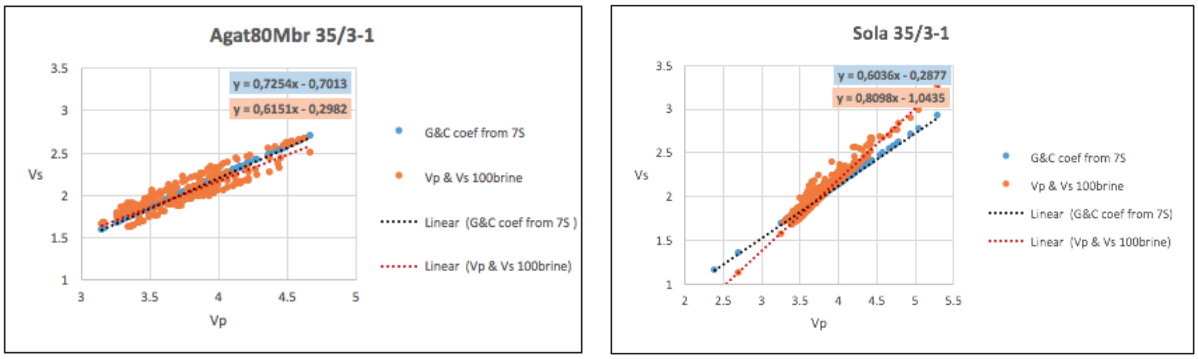

Figure 17: Vp versus Vs cross plots of the Agat 80 Member and Sola Formation for the 35/3-1 well. 35/3-1 log data is in orange with a red best fit line. This coincides closely with the Greenberg and Castagna coefficient trend line derived from the 35/3-7 S brine logs (blue).

5.3 Seismic-to-Well Tie

A seismic to well tie not only ensures accurate horizon picking but it is also essential for calibrating log data to models as log data provides a worthy estimate of subsurface parameters such as velocity and density. The seismic well tie is generated by creating a synthetic seismogram. This was done for all the wells in the study (35/3-1, 35/3-2, 35/3-4, and 35/3-7 S). An example seismic to well tie is shown in Figure 18 of the 35/3-2 Agat discovery well. To achieve an accurate well tie, it is fundamental that the shape of the wavelet is correctly determined. To achieve this, a spectral analysis was performed on the seismic data using a Fourier transform so that the actual seismic amplitude spectrum could be obtained. A time window was specified over the target interval (2.3 seconds to BCU) in order to mitigate the risk of phase changes with depth. This amplitude spectrum was then saved as a wavelet in the time domain. The wavelet tool in *Pre-Stack Pro* was then used to convert the wavelet/time signal in the time domain into the frequency domain using the

Fourier transform (Figure 19). A dominant frequency is observed at approximately 18 Hz.

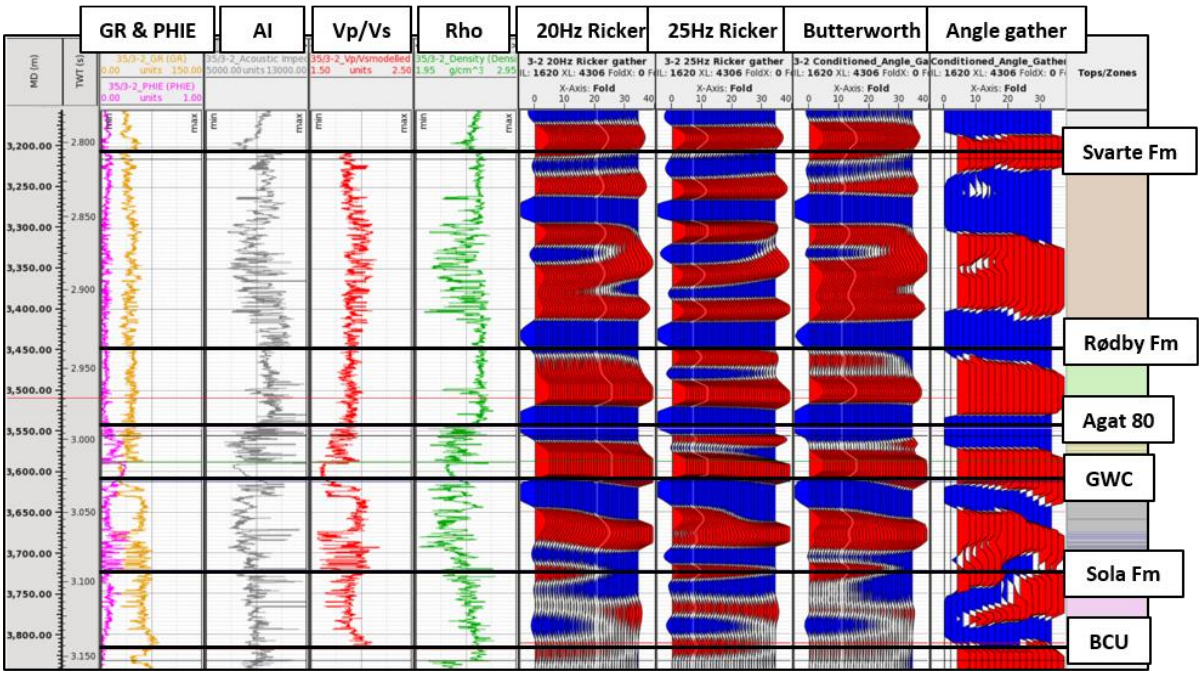

Figure 18: Seismic-to-well tie for the 35/3-2 Agat discovery well.

In addition to the amplitude spectrum another key piece of information needed to define the shape of the wavelet is the relative shift of the sine wave at each frequency (i.e. the phase). The wavelets shown in Figure 19 are all centred at time zero and are thus deemed zero phase. There are also many idealised wavelets that can be used to make well synthetics. Two types of Ricker wavelets and a Butterworth wavelet were used and the results compared as shown in Figure 18. The Ricker wavelet (Ricker, 1940) is defined by a central frequency and has only two side-lobes thus giving a “cleaner” reflectivity response than reality. Whereas, the Butterworth wavelet can be “shaped” to the frequency spectrum of the seismic data by manipulating lower- and upper-bandpass frequency limits and adjusting the slope of the spectrum (Figure 19). Although both methods gave good well tie results the Butterworth was observed to be moderately better and more representative of the conditioned angle gathers. This is most likely due to the Butterworth wavelet better matching the seismic frequency spectrum. Whereas, the Ricker wavelet has a peaked amplitude spectrum and doesn’t match the flat topped real seismic spectrum. Hosken (1998) has also advised not to use Ricker wavelets due to this fact.

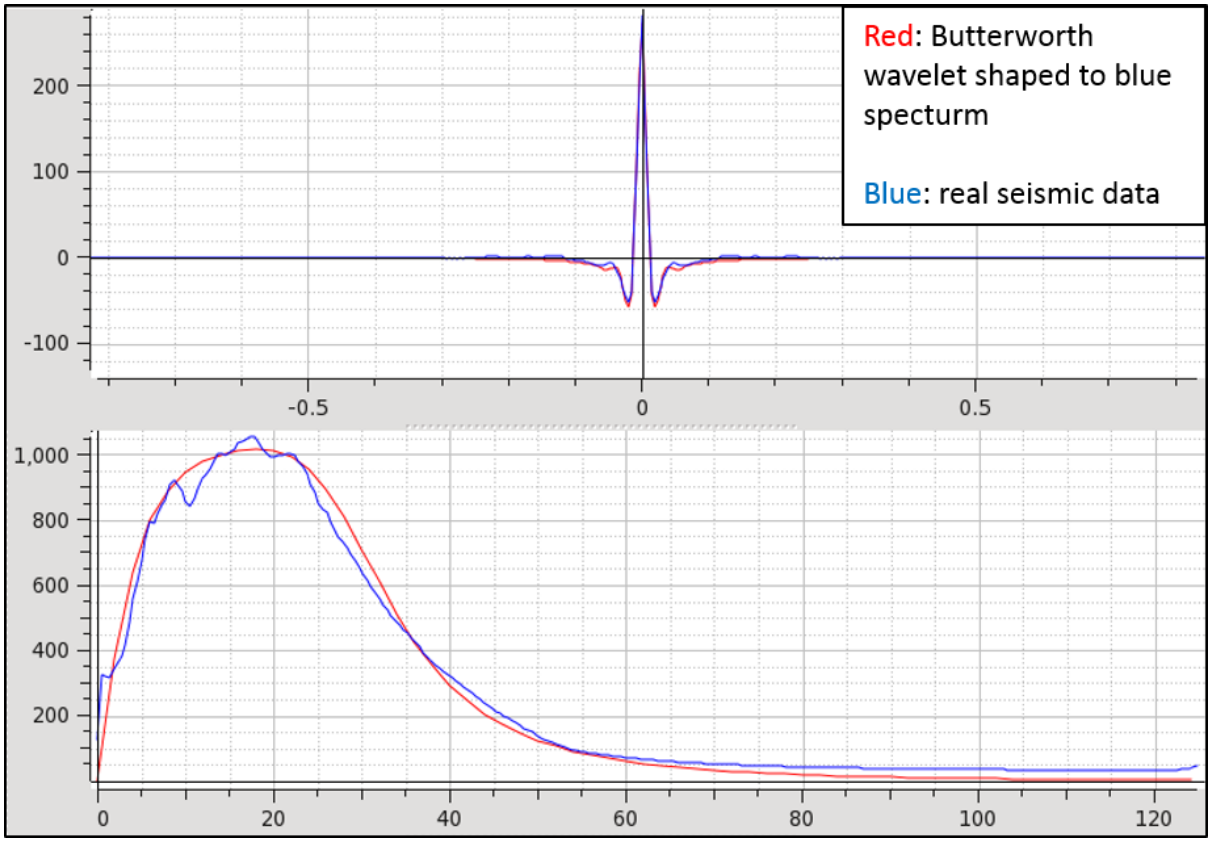

Figure 19: Butterworth wavelet used for seismic to well tie. The Butterworth wavelet is shaped to the frequency spectrum of the seismic data.

5.4 Cross Plotting of Rock Properties for Fluid and Lithology Discrimination

Before jumping into any AVA modelling, it is important to describe the Agat Formation in terms of its lithology and pore-fluid content. In this section, several cross plots have been created to determine the rock properties/attributes that better discriminate the reservoir. This creates a link between geophysical observations and geological parameters and provides an important part of reservoir characterisation (Golyan, 2012). For brevity, only examples from the 35/3-1 and 35/3-2 wells shall be shown as similar observations were found for each of the wells in this study.

The first cross plot (Figure 20a) displays *Density (Rho)* vs. *Vp* for the dry 35/3-1 well and illustrates the points from the Agat 70 and 80 Members highlighting the poor distinction between sand and shale intervals. A better discrimination was identified by cross plotting *Vp/Vs* vs. *Acoustic Impedance (AI)* (Figure 20b). This shows that although sand and shale intervals plot on a similar range of *AI* values their discrimination can be identified through

changes in the *Vp/Vs* ratio where sand units have lower *Vp/Vs* values than shale. Therefore, the *Vp/Vs* ratio is a good lithology discriminator. A similar plot is shown in Figure 20c for the 35/3-2 Agat discovery well which highlights not only the lithological discrimination from the *Vp/Vs* vs. *AI* cross plot, but also the fluid discrimination. Therefore, the *Vp/Vs* ratio is not only a great lithology but also a fluid discriminator for the Agat Formation, whereas *AI* shows little variation. These cross plots also show that the Agat Formation is not one simple homogenous sand unit but rather a series of sandy intervals interbedded with shales.

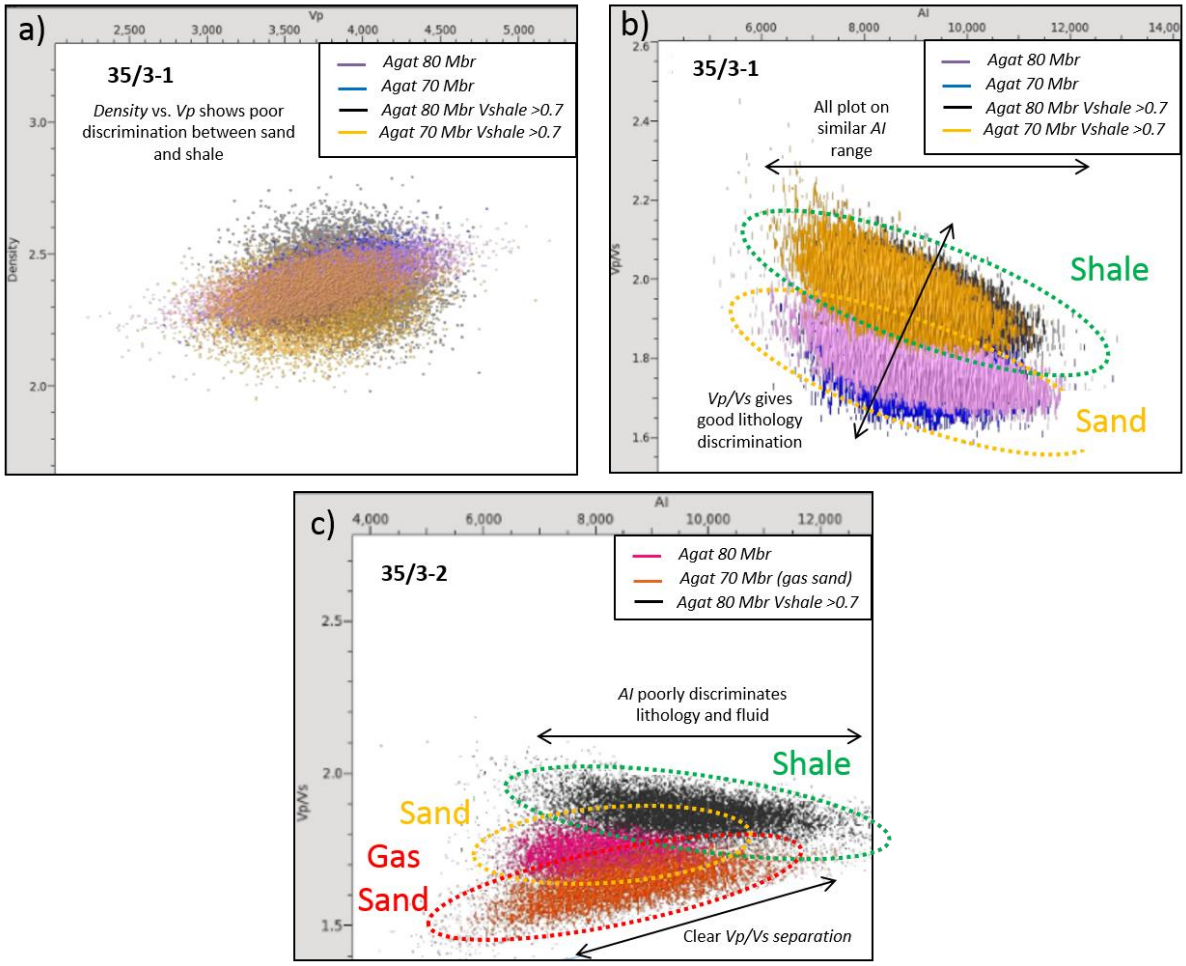

Figure 20: Cross plots of rock properties for fluid and lithology discrimination. a) Shows that density vs. Vp is a poor discriminator of lithology as both sands and shales plot on the same trend. b) Illustrates the clear lithology discrimination between sand and shale when cross plotting Vp/Vs vs. AI. However, this is primarily due to the separation on the Vp/Vs axis rather than the AI axis. c) Shows a similar trend to b) but for well 35/3-2, however it highlights not only a clear lithology discrimination but also fluid.

5.5 Amplitude versus Angle (AVO/AVA) Analysis

Before proceeding to the modelling of the Agat Formation an AVA analysis was first performed to define the AVA behavior of the Agat sand interval on real seismic data. Angle variations in amplitude for reflecting interfaces are represented as single points on the intercept vs. gradient cross plot (see Figure 21, Figure 22, Figure 23 and Figure 24). The advantage of this plot is that a great deal of information can be presented and trends can be observed in the data that would otherwise be impossible from standard offset versus amplitude plots. The cross plot is useful in understanding how variations in lithology and/or fluid impact the AVA response. In this case, the Top Agat sand is highlighted in grey on the cross plots for each well where a common theme of Class IV is observed for the 35/3-1, 35/3-4 and 35/3-7 S wells (Figure 21, Figure 23 and Figure 24, respectively) whereas the 35/3-2 shows a Class III (Figure 22). The reason for this discrepancy is further investigated later in section 5.8.2.

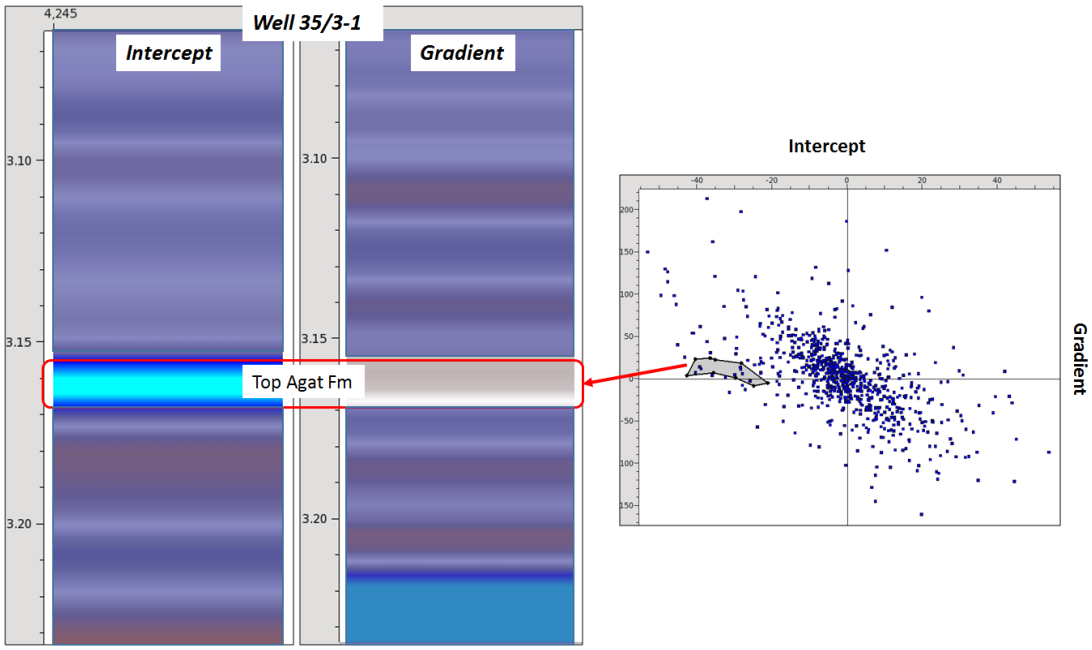

Figure 21: 35/3-1 intercept vs. gradient cross plot. The soft response of the Agat Formation plots as an AVA Class IV, defined as a negative intercept and positive gradient.

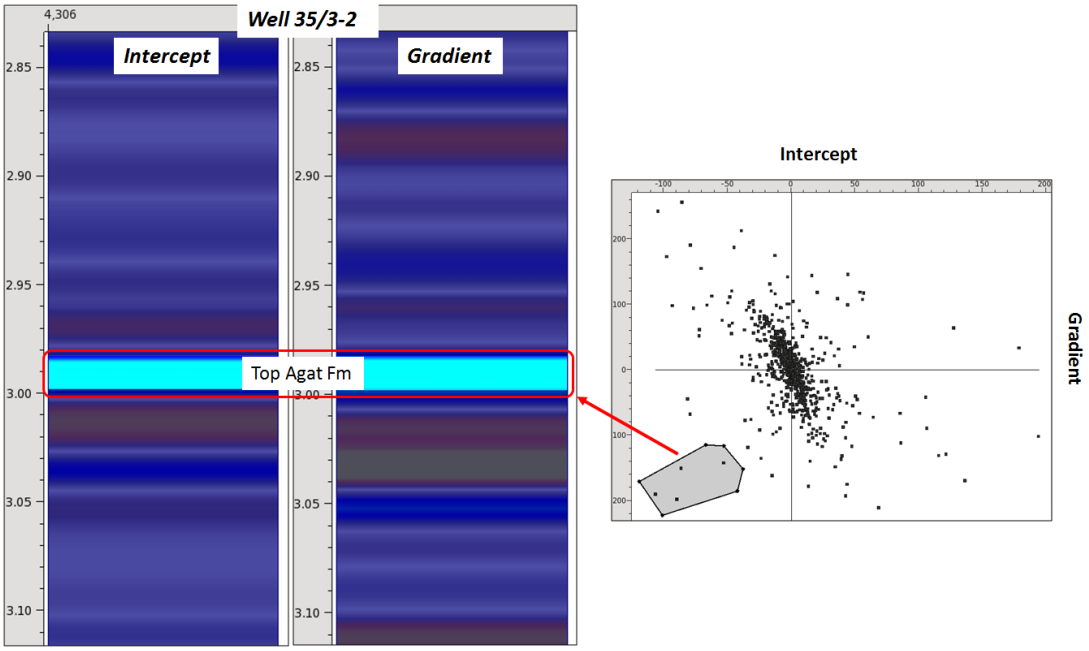

Figure 22: 35/3-2 intercept vs. gradient cross plot. The soft response of the Agat Formation plots as an AVA Class III, defined as a negative intercept and negative gradient. The 35/3-2 well is the only studied well not to show an AVA Class IV response.

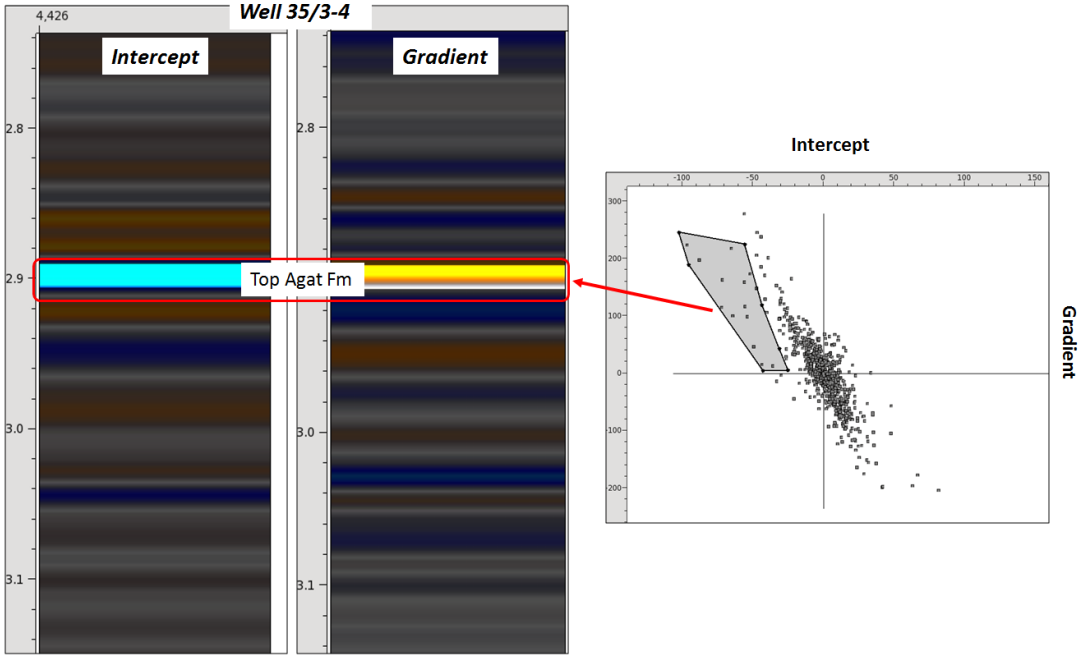

Figure 23: 35/3-4 intercept vs. gradient cross plot. The soft response of the Agat Formation plots as an AVA Class IV, defined as a negative intercept and positive gradient.

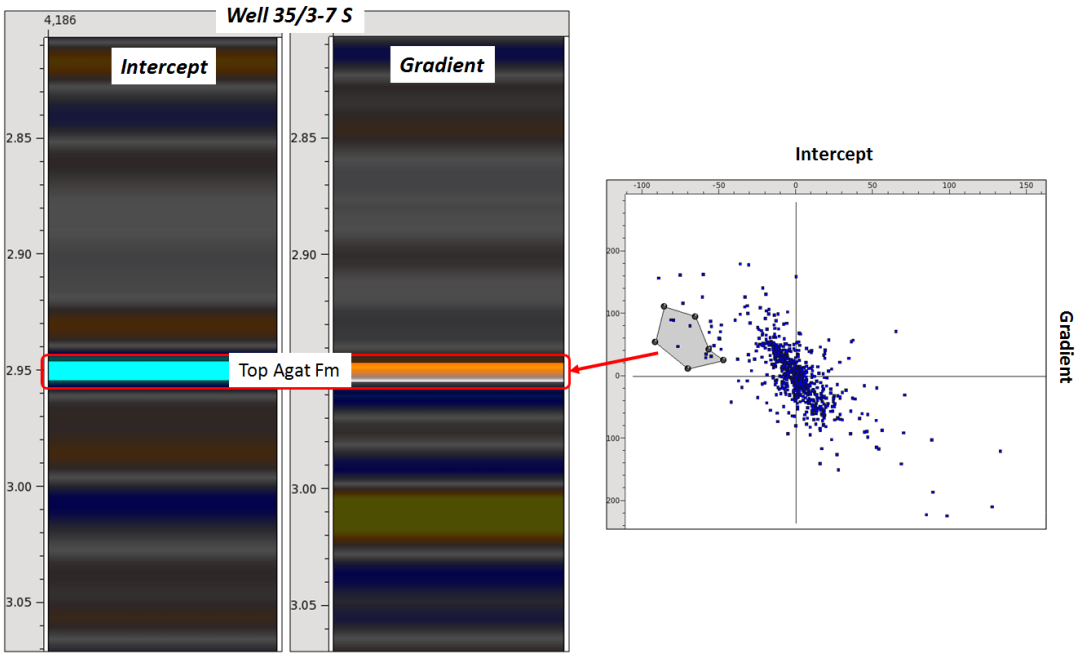

Figure 24: 35/3-7 S intercept vs. gradient cross plot. The soft response of the Agat Formation plots as an AVA Class IV, defined as a negative intercept and positive gradient.

5.6 Forward Modelling

The 3D Parametric Synthetic Model tool in *Pre-Stack Pro* is an advanced forward modelling tool that allows for 1, 2 or 3 parameters to be modelled simultaneously for e.g. water saturation, porosity and thickness. Firstly, layers are created from analysing log data, in this case acoustic impedance. These layers are representative of a much simpler geological model where properties such as *Vp*, *Vs*, and *Rho* are averaged for each layer. These layers are tested in the 3D Parametric Synthetic Model tool by specifying a wavelet and convolution method (e.g. Zoeppritz, 1919) and comparing the results with a gather and/or synthetic seismogram. Once the model is made, fluid substitution can be generated for a target layer – in this case the Agat reservoir. An example of the zone definition and modelled interval for the 35/3-1 is shown in Figure 25. A good match between the seismic gather, well synthetic and modelled synthetic can be observed showing the high robustness of the model. To see the modelled intervals for the other study wells please see section 9.1 of the appendix.

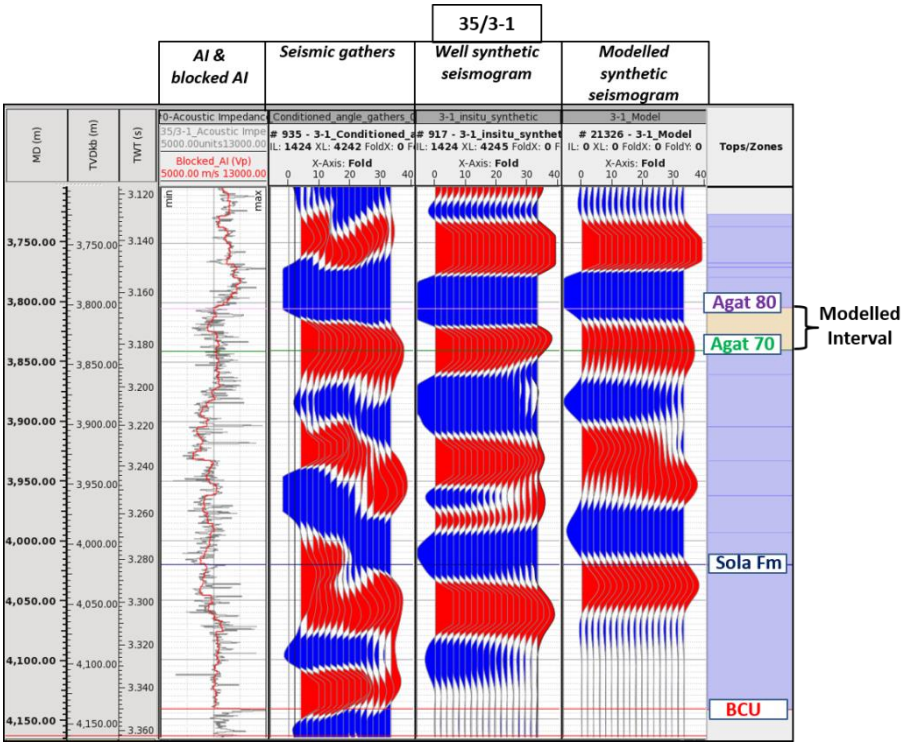

Figure 25: Zone definition and modelled interval of the 35/3-1 well. A comparison between the in situ seismic gather, in situ well synthetic seismogram and the in situ modelled synthetic seismogram is also shown and illustrates a good match between all three.

Figure 26 illustrates a further comparison between the real seismic gather, modelled parametric synthetic and well synthetic seismogram for well 35/3-4. Altogether, a good match is observed. Figure 26 also displays the "blocky" input logs used to create the models namely *Vp, Density* and *Vs* logs. These were created by specifying simple layers and averaging the log properties over that interval. The layers had to represent the seismic data and synthetic seismograms in order to be useful for modelling.

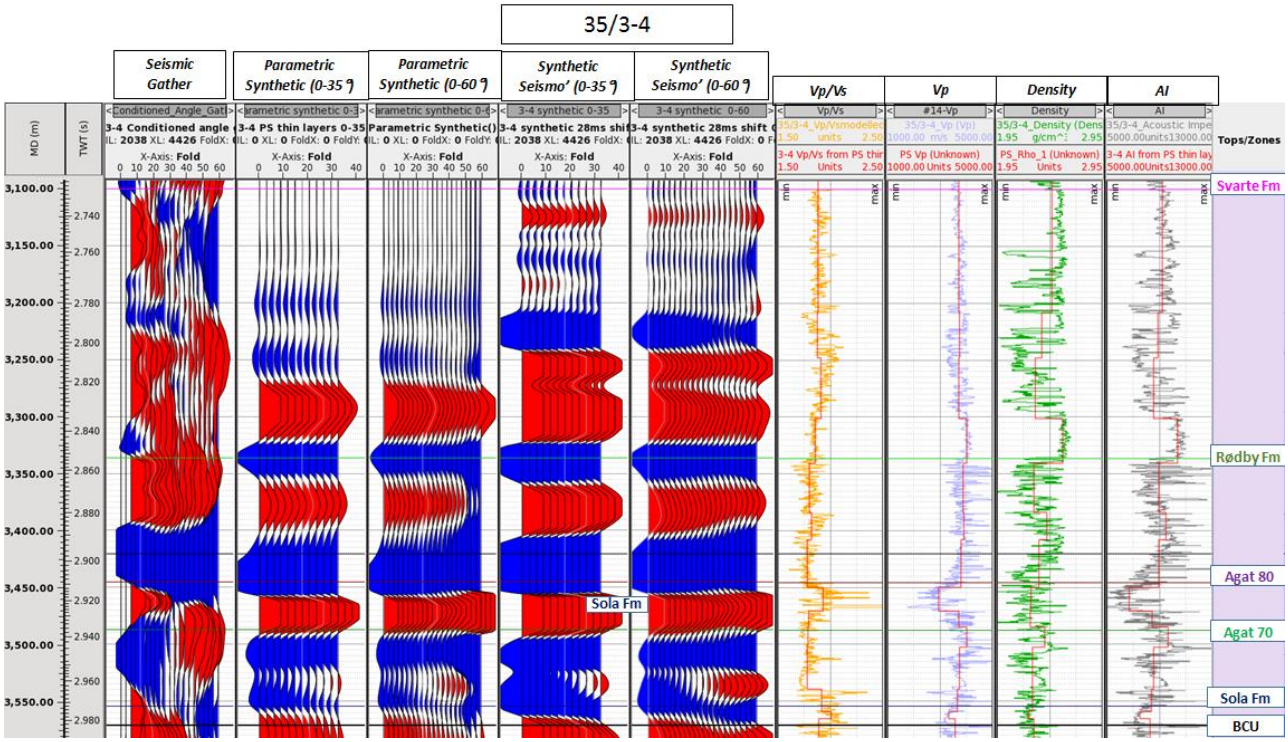

Figure 26: Comparison between seismic gather, modelled parametric synthetic and synthetic seismogram along with blocky log model inputs.

5.7 Fluid Substitution

Gassmann's fluid substitution was used as a fluid replacement method in *Pre-Stack Pro* where knowledge of the following input parameters was required:

- **Rock Properties:** in situ porosity, hydrocarbon saturation (HydroC-Percentage) and mineral bulk modulus (K-min)
- **Fluid Properties:** fluid bulk modulus (K-Brine and K-HydroC) and fluid density (Rho-Brine and Rho-HydroC)
- **Well Logs:** in situ *Vp, Vs and Rho*

With regards to the *Rock Properties* inputs for the modelled interval, average porosity values were estimated from effective porosity logs; hydrocarbon saturation values were derived from water saturation logs; and default sandstone mineral bulk modulus value was used: **K-min** (quartz) = 36.6 GPa. Example fluid substitution parameter inputs into *Pre-Stack Pro* are highlighted below in Figure 27.

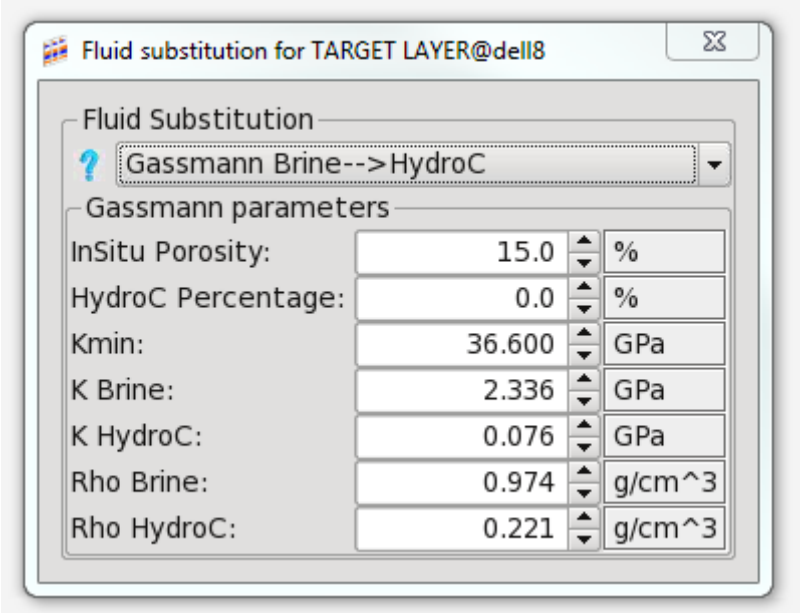

Figure 27: Pre-Stack Pro input fluid substitution parameter window.

Input values for the Batzle and Wang pore fluid calculation were taken from the publicly available completion reports of the Agat and Gjøa discovery wells, as described previously in section 4.5, and are summarized in Table 3. This resulted in accurate fluid bulk modulus and fluid density estimations of 2.336 GPa and 0.974 g/cm^3 for brine, and 0.076 GPa and 0.221 g/cm^3 for gas (Figure 27). For oil, the calculated fluid bulk modulus and density estimations were 1.356 GPa and 0.8 g/cm^3, respectively.

Temperature (°C)	108
Pressure (MPa)	31.2
Salinity	9000 ppm
Gas/Oil ratio (v/v)	222
Oil Density (g/cm^3)	0.63
Gas Gravity	0.75 (air = 1)

Table 3: Agat fluid parameters.

Gassmann's fluid substitution was performed on each well where the in situ response was firstly modelled to 100% water and then to 5%, 50% and 80% saturations of oil and gas. The 5% scenario was selected to illustrate fizz gas and residual oil effects. Figure 28, Figure 29, Figure 30 and Figure 31 show the oil and gas fluid substituted models for each of the studied wells.

A similar pattern is observed for each of the wells as the modelling shows a Class IV AVA response for the top of the Agat sands (soft amplitude becoming harder with offset), albeit subtle in some cases (well 35/3-7 S, Figure 31). Overall the amplitude increases from brine to gas and from brine to oil, therefore discriminating between water and hydrocarbons should be feasible. However, in most cases the 80% gas and 80% oil saturations give a similar response, therefore distinguishing phase from the seismic data is likely to be difficult. For the interpreted base Agat sand, a Class I AVA response is observed.

For the remainder of this thesis only the brine and gas saturated results will be included in the main part of this thesis. The oil results can be found in the appendix in section 9. This is to reduce the overall number of figures to avoid confusion and oversaturating the reader with too much information.

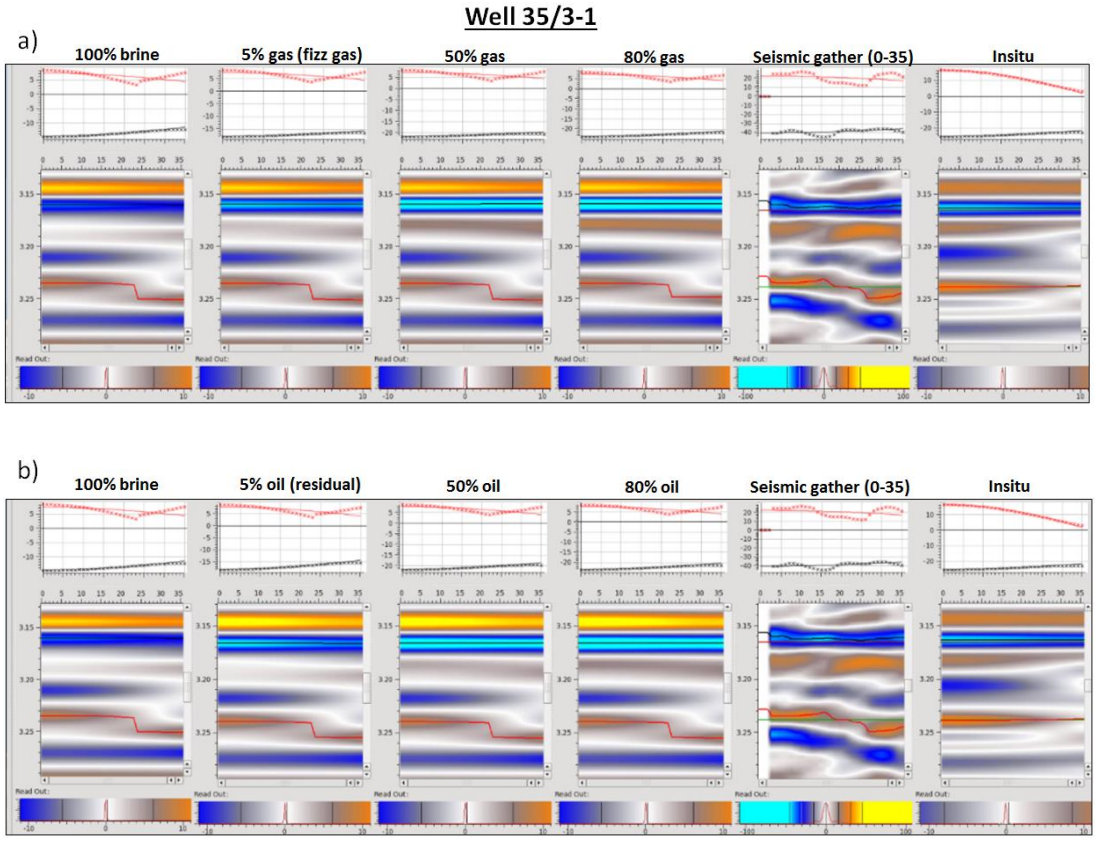

Figure 28: Comparison between synthetic fluid substituted response versus the real seismic gather response for well 35/3-1 a) Brine to gas-filled; and b) brine to oil-filled. AVA plots are displayed where the Top and Base Agat picks are highlighted by black and red lines, respectively. A Class IV Top Agat and Class I Base Agat AVA response is observed across all cases. The in situ (20% gas saturation) response is in agreement with the fluid substitution results.

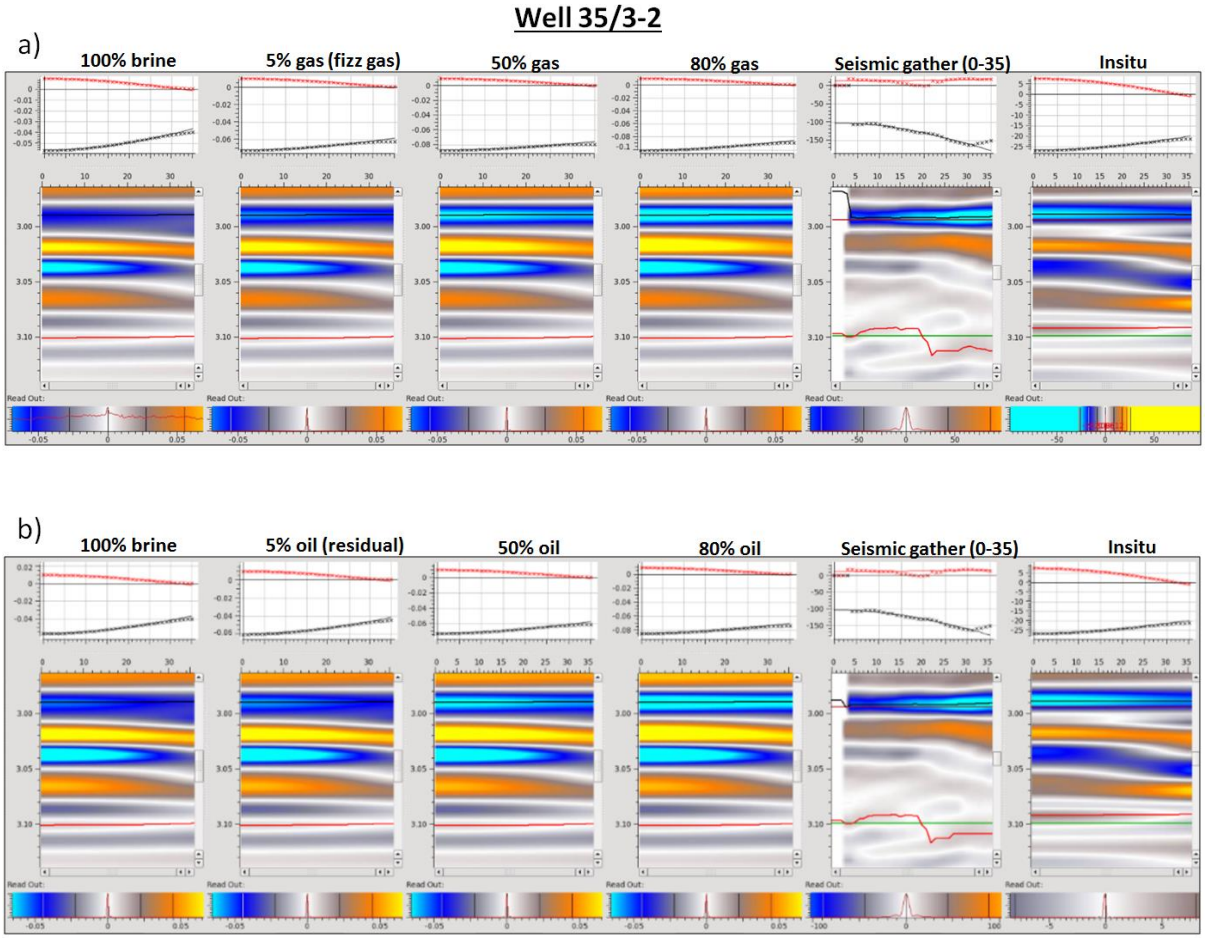

Figure 29: Comparison between synthetic fluid substituted responses versus the real seismic gather response for well 35/3-2. a) Brine to gas-filled; and b) brine to oil-filled. AVA plots are displayed where the Top and Base Agat picks are highlighted by black and red lines, respectively. A Class IV Top Agat response is observed in all fluid substituted cases and does not match the Class III observed by the in situ seismic gather. The in situ (50-60% gas saturation) response is in agreement with the fluid substitution results

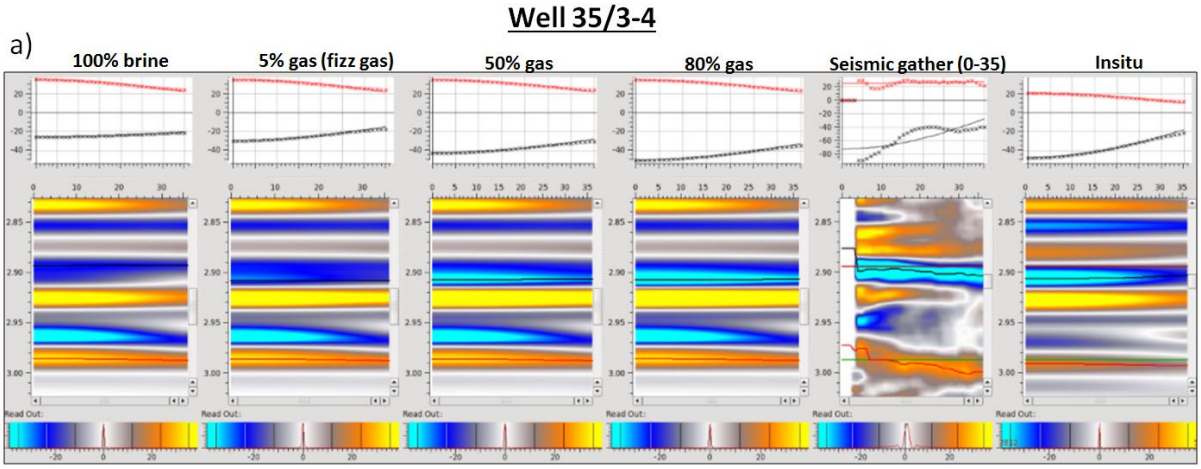

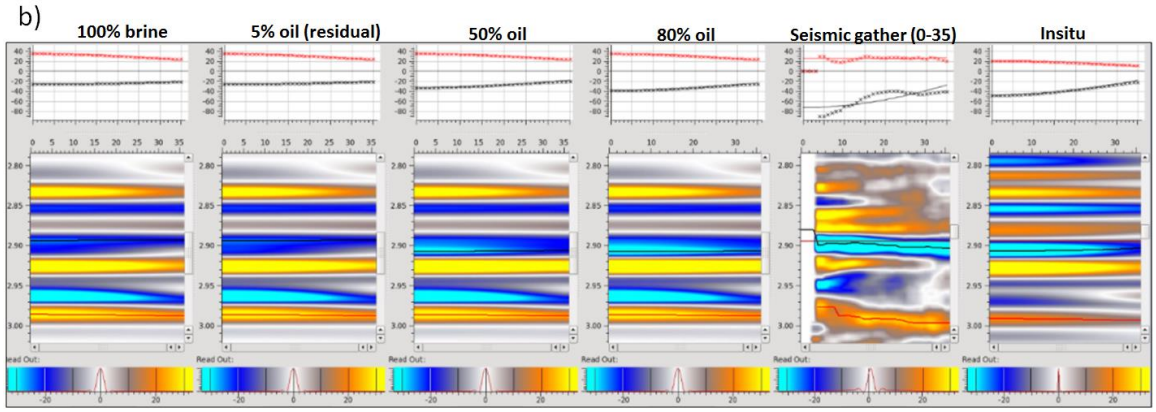

Figure 30: Comparison between synthetic fluid substituted responses versus the real seismic gather response for well 35/3-4. a) Brine to gas-filled; and b) brine to oil-filled. AVA plots are displayed where the Top and Base Agat picks are highlighted by black and red lines, respectively. A Class IV Top Agat and Class I Base Agat AVA response is observed across all cases. The in situ (50% gas saturation within the lowermost Agat 80Mbr) response is in agreement with the fluid substitution results.

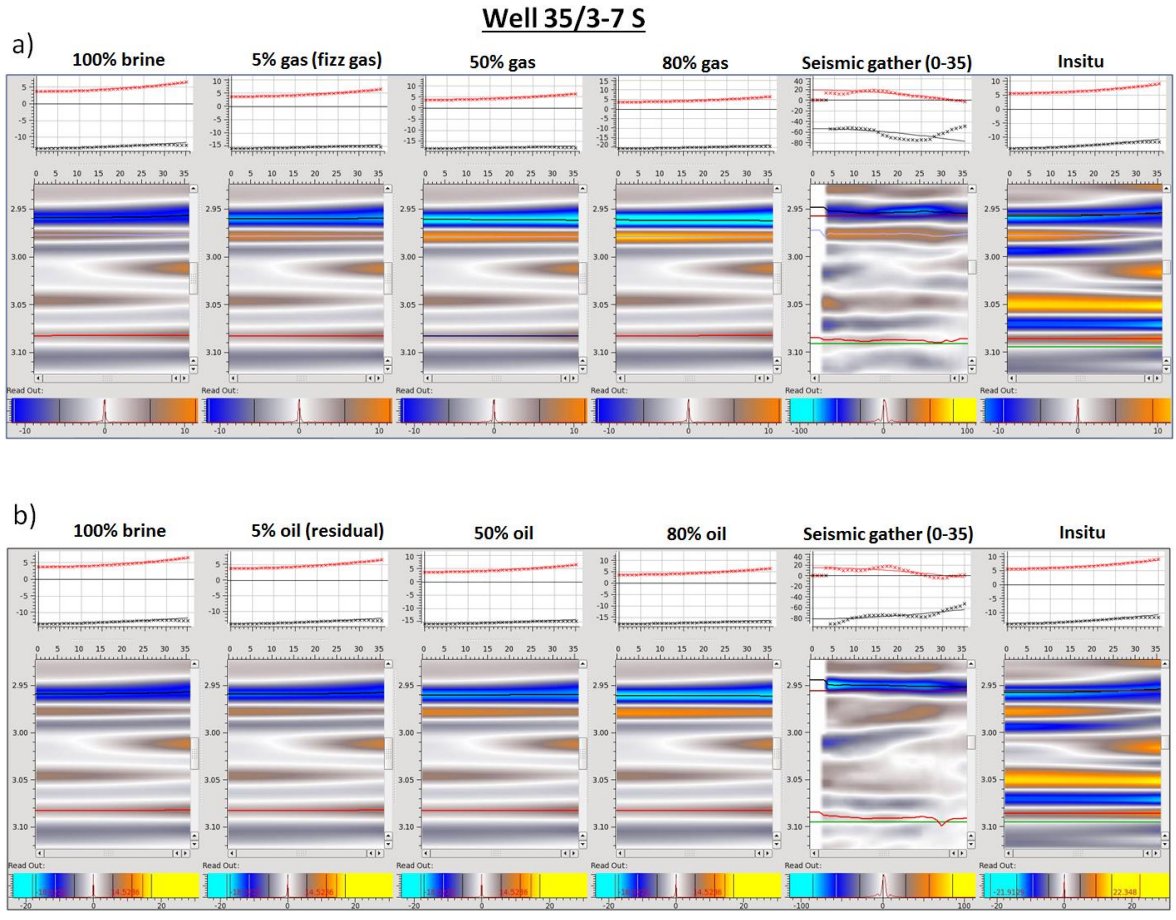

Figure 31: Comparison between synthetic fluid substituted responses versus the real seismic gather response for well 35/3-7 S. a) Brine to gas-filled; and b) brine to oil-filled. AVA plots are displayed where the Top and Base Agat picks are highlighted by black and red lines, respectively. A Class IV Top Agat and Class I Base Agat AVA response is observed across all cases. The in situ (20% gas saturation) response is in agreement with the fluid substitution results.

Observations from the AVA plots in (Figure 28, Figure 29, Figure 30 and Figure 31) are summarized in Table 4. This highlights that the in situ synthetic seismogram and real seismic gather responses for the Top Agat Formation in wells 35/3-1, 35/3-4 and 35/3-7 S all show a Class IV AVA character. Furthermore, a strong match is also observed for the Base Agat Formation where both the in situ synthetic seismogram and the real seismic gather have Class I responses for all wells. On the other hand, the Top Agat Formation of the 35/3-2 well does not have such a strong match as an inconsistency is observed between the modelled in situ and real seismic gather response. In this case the in situ synthetic seismogram response has a Class IV AVA character similar to wells 35/3-1, 35/3-4 and 35/3-7 S, however the real seismic gather displays a Class III AVA character. The difference between the two at this stage is not certain and may be due to an aspect of the seismic processing. However, this is further investigated later in *4.14.2 P-wave velocity vs. Hydrocarbon saturation* where it appears that an overlying shale with a high P-wave velocity may be the reason for the Class III observed in well 35/3-2.

Well	Level of Interest	In situ Synthetic Seismogram AVA Class	Real Seismic Gather AVA Class
35/3-1	Top Agat	Class IV	Class IV
	Base Agat	Class I	Class I
35/3-2	Top Agat	Class IV	Class III
	Base Agat	Class I	Class I
35/3-4	Top Agat	Class IV	Class IV
	Base Agat	Class I	Class I
35/3-7 S	Top Agat	Class IV	Class IV
	Base Agat	Class I	Class I

Table 4: Comparison of the in situ synthetic seismogram AVA class vs. real seismic gather AVA class for Top and Base Agat Formation. A strong match is clearly observed for the Top and Base Agat Formation in all wells except for the Top Agat Formation in well 35/3-2 where the in situ synthetic seismogram displays a Class IV and the real seismic gather a Class III.

5.8 3D Parametric Modelling

The 3D parametric modelling approach was first introduced by Russel et al (2000) where they created a 3D volume of modelled CDP gathers by varying two physical parameters at one time. This creates a cube of multi-offset AVA models, each with a different combination of physical parameters. This cube can be processed in a traditional fashion to compute two physical parameter attributes (for e.g. porosity vs. hydrocarbon saturation) and the results can then be displayed in a data slice format, where the inline direction relates to changes in the first parameter, and the cross-line relates to changes in the second parameter This thesis will look at numerous examples for this method where the following rock properties shall be varied against hydrocarbon saturation to investigate how changes in these parameters affects the variability of the Top Agat amplitude and AVA response for the studied wells:

- Porosity (ø)
- Thickness (*m*)
- Compressional velocity (*Vp*) (of overlying shale)
- Mineral bulk modulus (*Kmin*)

This thesis will also take Russel et al's (2000) AVA modelling approach one step further and explore not only two physical parameter variations but also three for e.g. porosity in the inline direction, thickness in the crossline direction and hydrocarbon saturation per volume.

5.8.1 Porosity vs. Hydrocarbon Saturation

In the first stage of AVA Modelling, two physical parameters were varied, porosity in the in-line direction and hydrocarbon saturation in the cross-line direction. The hydrocarbon saturation was modelled twice – firstly with gas (Figure 32) and secondly with oil (9 *Appendix*). Figure 32 show cross-lines from the 100% brine, 5% fizz gas and 80% gas models with porosity increasing from left to right for the 35/3-2 well.

The brine saturated response shows a subtle Class IV AVA effect and has a marked reduction in amplitude compared to its gas saturated counterparts. Amplitudes become increasingly softer with increasing hydrocarbon saturation and therefore discriminating between brine

and gas saturated sands using amplitudes alone is feasible. In the 80% gas saturated case the near angle amplitude is relatively constant across all porosities. However, the Class IV AVA anomaly becomes much more prominent with increasing porosity values and a similar observation is also found in the 5% gas saturated scenario. Porosity therefore has a strong impact on AVA when the target layer contains hydrocarbons; however, there is no impact in the 100% brine case.

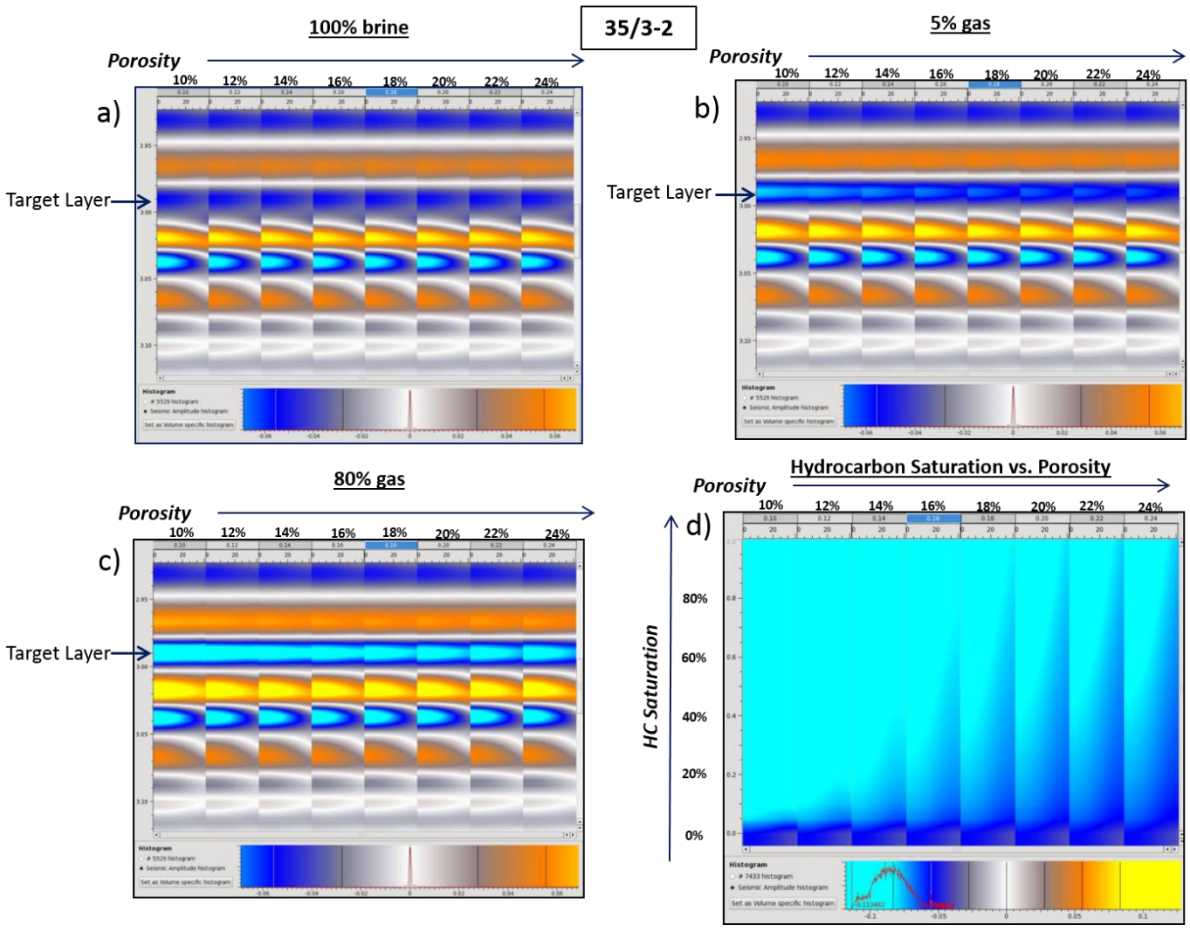

Figure 32: AVA modelling of porosity vs. gas saturation for the 35/3-2 Agat Discovery well. a) Brine saturated; b) 5% gas saturated; and c) 80% gas saturated with porosity increasing from left to right. d) Shows a 2D gather map of porosity vs. HC (gas) saturation.

The gather maps in Figure 32d and Figure 33 show porosity (x-axis) and gas saturation (y-axis) simultaneously with each of the studied wells displayed in Figure 33. This provides an overall summary of how their relationship affects the seismic response. An AVA Class IV response is observed for all the varied porosity values for each well. However, when the rock is saturated in brine there is a marked reduction in amplitude and AVA effect where the Class IV response becomes much more reduced and approaches the border between

Class III and Class IV (little change in amplitude with angle). This is particularly evident in the 35/3-4 well. A similar Class IV/Class III response can be observed in low porosity (10%) highly gas saturated scenarios where although the amplitudes are significantly softer, there is little variation with angle. It is however clear that when hydrocarbon saturations are equal to or greater than 5% there is a sharp increase in seismic amplitude which gradually becomes softer with increasing hydrocarbon saturation. Furthermore, the Class IV AVA effect becomes more prominent when porosities and hydrocarbon saturations are higher.

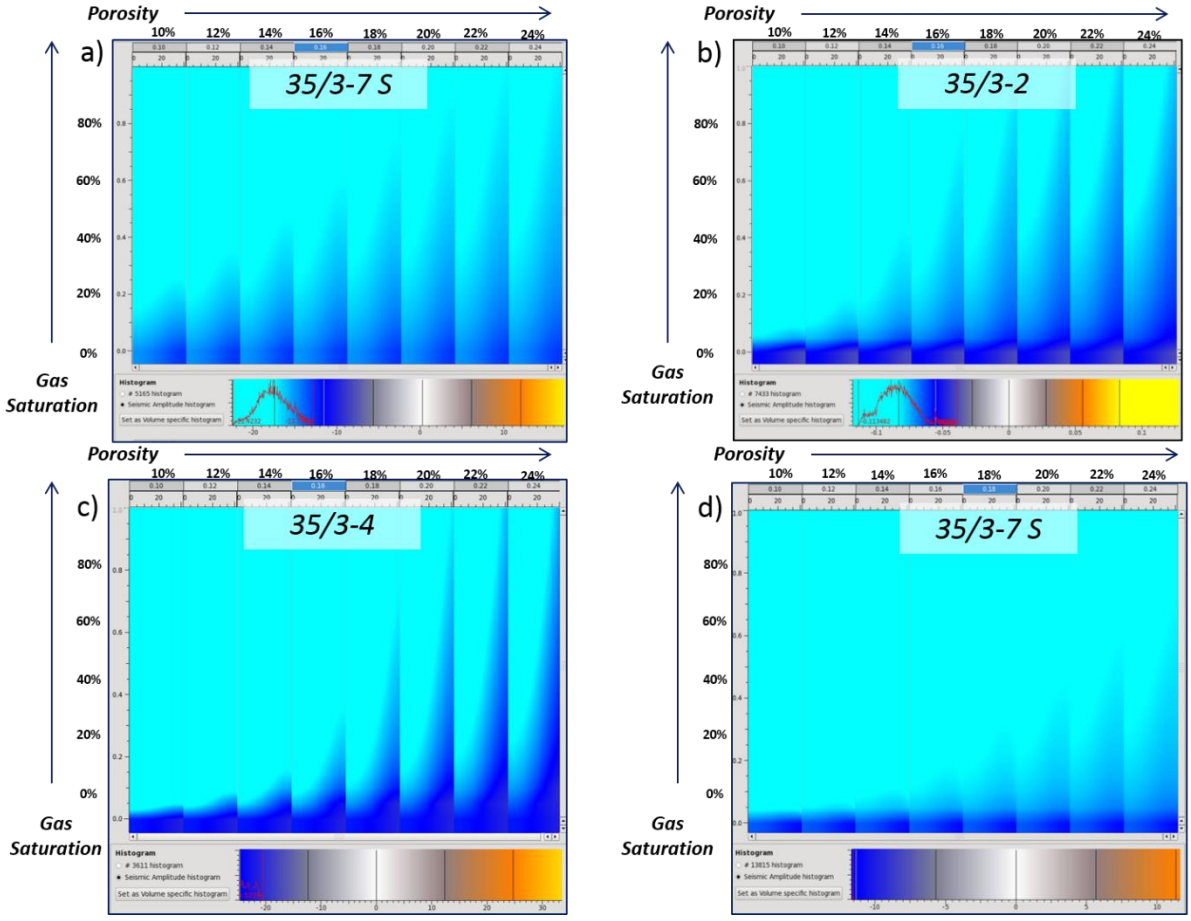

Figure 33: Porosity vs. gas Saturation 2D gather maps. For wells: a) 35/3-1; b) 35/3-2; c) 35/3-4 and; d) 35/3-7 S.

One can therefore conclude that the amplitude of a brine-filled Agat sand is relatively dim across all porosity values. The AVA response is also unaffected by porosity and contains a relatively flat Class III/Class IV to a very subtle Class IV response. On the other hand, hydrocarbon saturated sands are clearly brighter with a more prominent AVA Class IV particularly in high porosity circumstances. A summary of the brine and gas saturated results are highlighted in Table 5 and Table 6.

Brine Saturated				
Porosity (%)	AVA Class	Intercept	Gradient	AVA
Low (10)	Subtle IV	Negative	Positive	Trough decreasing in amplitude with offset
In situ (15)	Subtle IV	Negative	Positive	Trough decreasing in amplitude with offset
High (24)	Subtle IV	Negative	Positive	Trough decreasing in amplitude with offset

Table 5: Summary table of how varying porosity impacts the AVA, intercept and gradient of a brine saturated Agat sand.

Gas Saturated				
Porosity (%)	AVA Class	Intercept	Gradient	AVA
Low (10)	IV	Very Negative	Flat to Positive	Trough decreasing in amplitude with offset very subtly
In situ (15)	IV	Very Negative	Positive	Trough decreasing in amplitude with offset
High (24)	IV	Very Negative	Positive	Trough decreasing in amplitude with offset

Table 6: Summary table of how varying porosity impacts the AVA, intercept and gradient of a gas saturated Agat sand.

5.8.2 P-wave Velocity of Overlying Shale vs. Hydrocarbon Saturation

The Class IV AVA anomalies that have been thus far identified in the modelled Agat interval are a result of the Agat sand, in each of the wells, having lower impedance values than the overlying shale, for which the reflection coefficient becomes more positive with increasing offset. Therefore, the velocity of the overlying shale is a determining factor in the AVA response of the Top Agat Formation. To investigate varying shale *P-wave* velocities (*Vp*) and its impact on the Top Agat AVA response, a model was created where the two varied

physical parameters were *Vp* in the in-line direction and hydrocarbon saturation in the cross-line direction.

Cross-lines with varying gas saturations for the 35/3-2 well are shown in Figure 34, where *Vp* is centred at a value of *4000 ms^{-1}* (in situ average for modelled cap rock *Vp* was 4053 ms^{-1} and reservoir Vp 3834 ms^{-1}) and decreases to the left and increases to the right. In the brine saturated scenario, moving from the in situ value of *4053 ms^{-1}* to *3700 ms^{-1}*, results in a change of polarity and an increase in the Class IV AVO effect. A similar situation occurs in the 5% gas scenario but the polarity reversal is not as strong and diminishes in the 80% gas case. Increasing *Vp* values from 4000 ms^{-1} to 4300 ms^{-1} results in an overall increase in amplitude for all brine and gas saturated scenarios. However, the Class IV becomes much more reduced by 4300 ms^{-1} and it begins to become a Class III. It is also important to note that beyond 4300 ms^{-1} the amplitude and AVA responses are almost identical for both brine and gas.

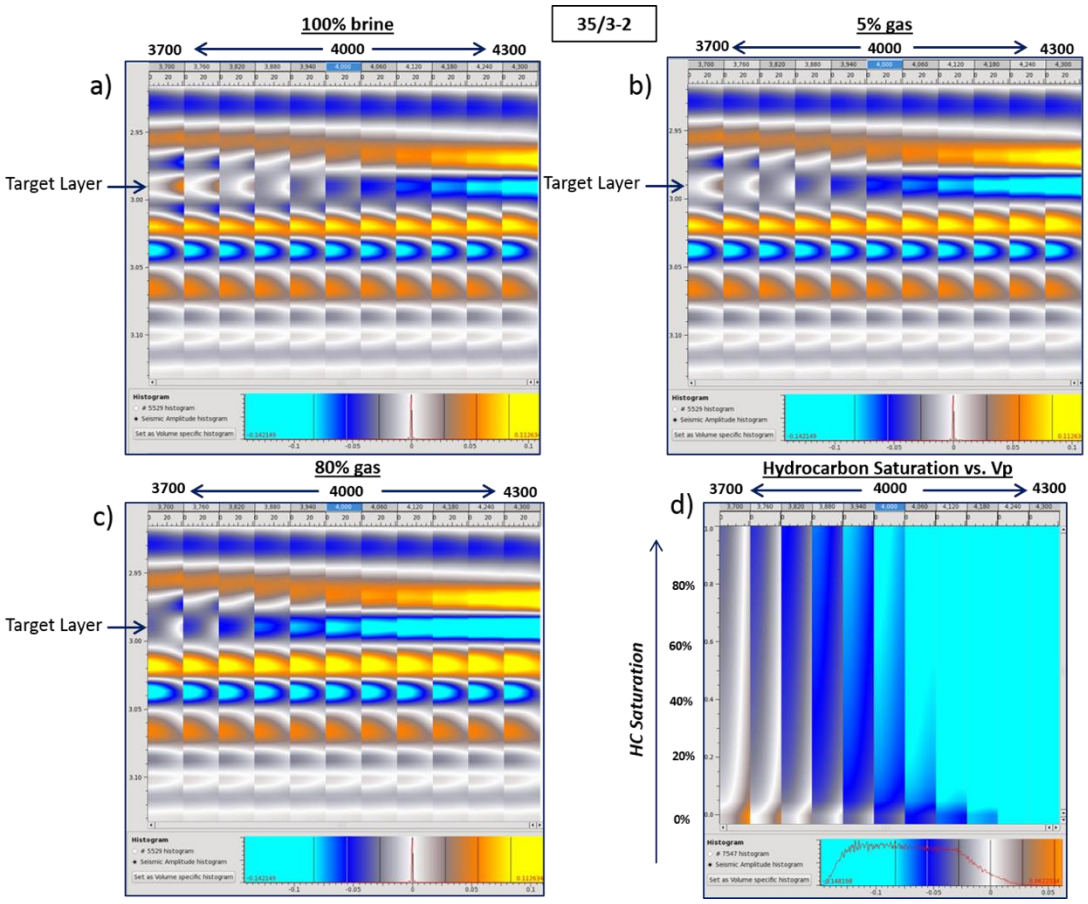

Figure 34: AVA modelling of P-wave velocity (Vp) of the overlying shale vs. gas saturation for the 35/3-2 Agat Discovery well.

The gather map in Figure 34d shows *P-wave velocity (Vp)* (x-axis) and gas saturation (y-axis). It is apparent that changing *Vp* has a significant impact on the AVA response, even more so than hydrocarbon saturation. Increasing *Vp* and hydrocarbon saturation results in a much softer Top Agat response. This was to be expected and is not out of the ordinary. However, what is interesting is the fact that a reduction in the P-wave velocity of the overlying shale by as little as 7.5% (300 ms^{-1}) can result in a complete polarity reversal whereas an increase by 7.5% (300 ms^{-1}) can result in a rapid increase in amplitude and a progression from Class IV to Class III AVA. It is therefore of great importance to understand *Vp*, and in turn *AI*, of the overlying shale as it has a significant impact on the AVA response. It also lets a seismic interpreter know that a hard Top Agat response that becomes harder with offset can be exclusively linked to a brine-filled sand overlain by a low velocity (<3700 ms^{-1}) shale.

Figure 35 summarises the significant changes in AVA Classes as a result of varying P-wave velocity of the overlying shale, which is elaborated in Table 7 and Table 8 for brine and gas saturated sands, respectively.

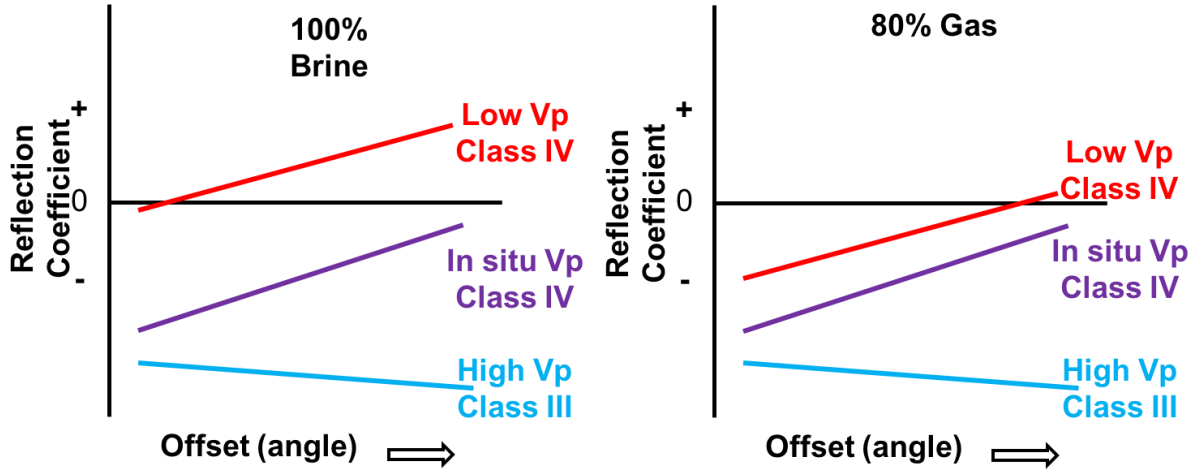

Figure 35: Reflection coefficient vs. angle for brine and gas Agat sands in relation to P-wave velocity changes of the overlying shale.

Brine Saturated				
P-wave velocity (m/s)	AVA Class	Intercept	Gradient	AVA
Low (3700)	IV	Near zero	Positive	Nearly transparent becoming a peak; amplitude increases with angle
In situ (4053)	IV	Negative	Positive	Trough decreasing in amplitude with offset
High (4700)	III	Negative	Negative	Trough increasing in amplitude with offset

Table 7: Summary table of how varying P-wave velocity of the overlying shale impacts the AVA, intercept and gradient characteristics of a brine saturated Agat sand.

Gas Saturated				
P-wave velocity (m/s)	AVA Class	Intercept	Gradient	AVA
Low (3700)	IV	Negative	Positive	Trough decreasing in amplitude with offset; Transparent at high angles
In situ (4053)	IV	Negative	Positive	Trough decreasing in amplitude with offset
High (4700)	III	Very Negative	Negative	Trough increasing in amplitude with offset

Table 8: Summary table of how varying P-wave velocity of the overlying shale impacts the AVA, intercept and gradient characteristics of a gas saturated Agat sand.

Referring to section 5.7 and Figure 22, the fluid substituted synthetic seismograms and real seismic gather for well 35/3-2 displayed different AVA responses. The former exhibited a Class IV and the latter a Class III. One explanation for this may be that, in the location of the 35/3-2 well, the overlying shale has a high P-wave velocity. This would result in a Class III response as demonstrated by the modelling above and also in Figure 36 below. Figure 36

shows the results of well 35/3-2 when the overlying shale has a high P-wave velocity of 4700 ms^{-1}. A clear Class III AVA response is observed across all fluid scenarios.

.

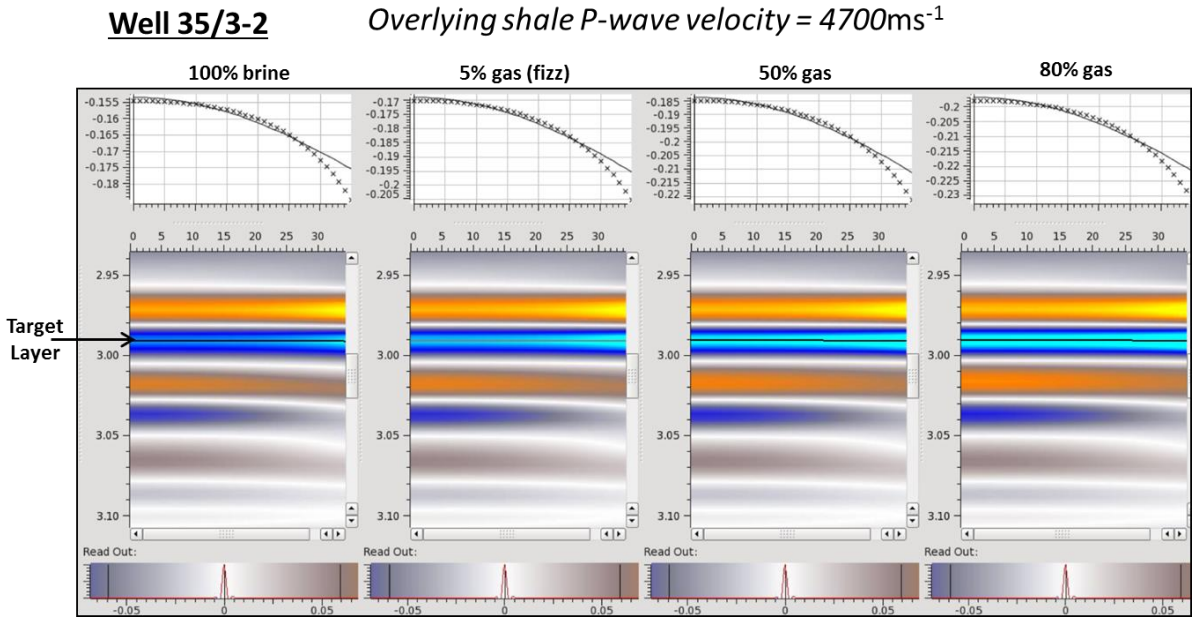

Figure 36: AVA modelling of P-wave velocity (Vp) of the overlying shale vs. gas saturation for the 35/3-2 Agat Discovery well. In this case the shale is modelled at 4700 ms^{-1} where a Class III is observed across all fluid responses.

5.8.3 Mineral Bulk Modulus (Kmin) vs. Hydrocarbon Saturation

Reservoir rocks consist of a variety of components, such as minerals, clays, cements, pores, pore fluids, etc. It can therefore be difficult to assume that a default sandstone bulk mineral modulus value of 36.6 GPa (Table 9; Mavko et al., 2009) is an accurate depiction of the reservoir as it actually contains considerable amounts of shale. Wang et al (2001) has shown that clay densities can vary between 2.2 g/cm^3 to 2.8 g/cm^3, therefore a sand with some shale fraction component is likely to have a lower mineral bulk modulus than a pure sand scenario in most cases. It is also clear from CPI data that the Agat Members are not homogeneous, isotropic sandstones but are in fact a complex sequence of sand-shale interbeds as well as shaley sands with some wells having drilled in the middle of the channel axis and others on its peripherals.

Complications can arise with regards to shaley sands as they violate the assumptions of the Gassmann's equation and further studies on this are suggested later in section *6*. However, in an attempt to understand the effect of shaley sands on the seismic response an AVA model has been created where mineral bulk modulus (*Kmin*) properties are varied in the inline direction and hydrocarbon saturation values are varied in the cross line direction (Figure 37). In this model, low mineral bulk modulus values represent a sandstone/shale mix.

	Bulk Modulus (GPa)	Density (g/cm^3)	Shear Modulus (GPa)	Vp (ms^{-1})	Vs (ms^{-1})
Quartz	36.6	2.65	45.0	6038	4121
K-feldspar	48.0	2.56	24.0	5600	3050
Dolomite	94.9	2.87	45.0	7347	3960
Calcite	76.8	2.35	32.0	5400	3700

Table 9: Bulk modulus, density, shear modulus, Vp and Vs values for mineral components. Wang et al (2001) has shown that clay densities vary between 2.2 g/cm^3 to 2.8 g/cm^3. Mavko et al., 2009.

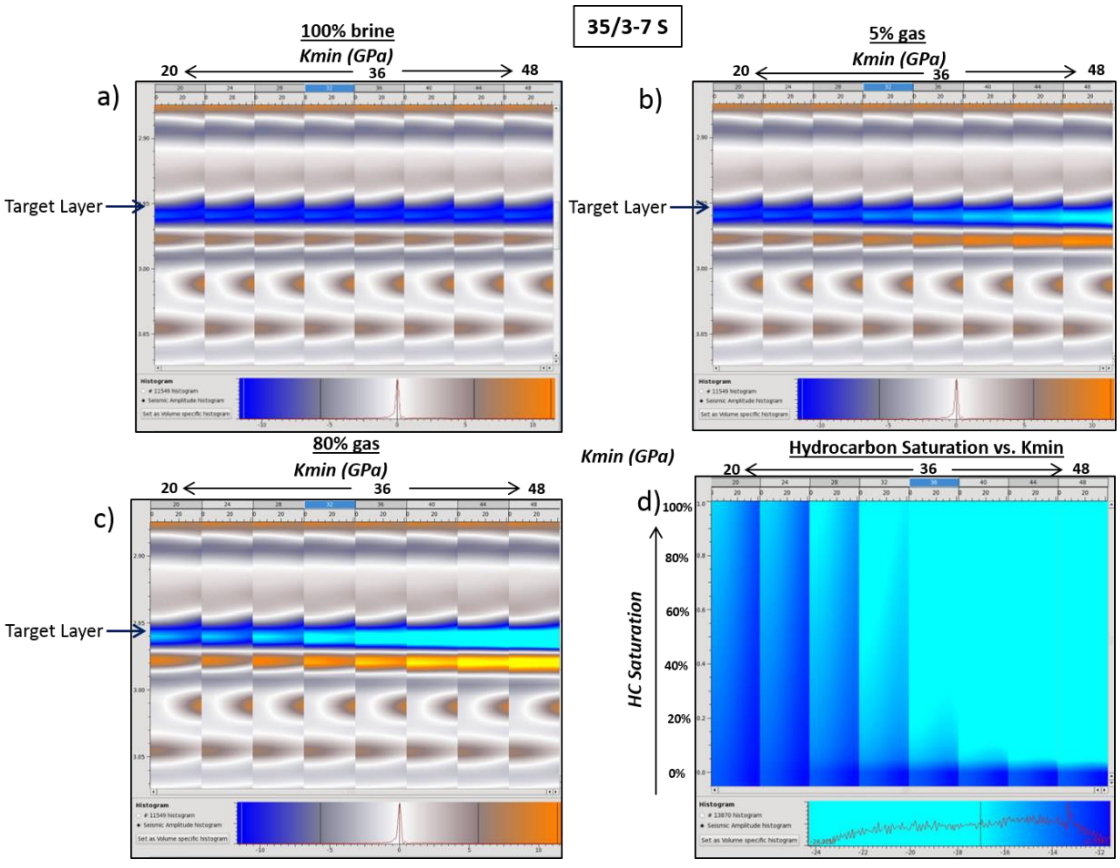

Figure 37: AVA modelling of bulk mineral modulus (Kmin) vs. gas saturation for the 35/3-7 S discovery well.

In the 100% brine cross line direction (Figure 37a) the mineral bulk modulus response has no impact on the Top Agat amplitude or AVA response. Whereas, the 5% gas and 80% gas cross lines clearly show a reduction in amplitude with decreasing mineral bulk modulus; or in other words shalier sands have reduced amplitudes. Extending the *Kmin* value beyond the standard 36.6 GPa of a sandstone is unlikely but it could occur if the sand body contains a percentage of shale that has greater mineral bulk modulus values than the sand itself. A consistent relationship can be found in all the studied wells (Figure 38) where high *Kmin* values do not show variation with offset but low *Kmin* values produce an increasingly prominent Class IV AVA character.

An interesting feature, and note of caution, is that in many cases an 80% gas saturated shaley sand, with a <26 GPa *Kmin* value, has a very similar response to a 10% gas-filled pure sandstone, with a typical 36 GPa *Kmin* value. This raises the point that although there is a clear correlation between amplitude and *Kmin* it can be difficult to discriminate between high and low gas saturations.

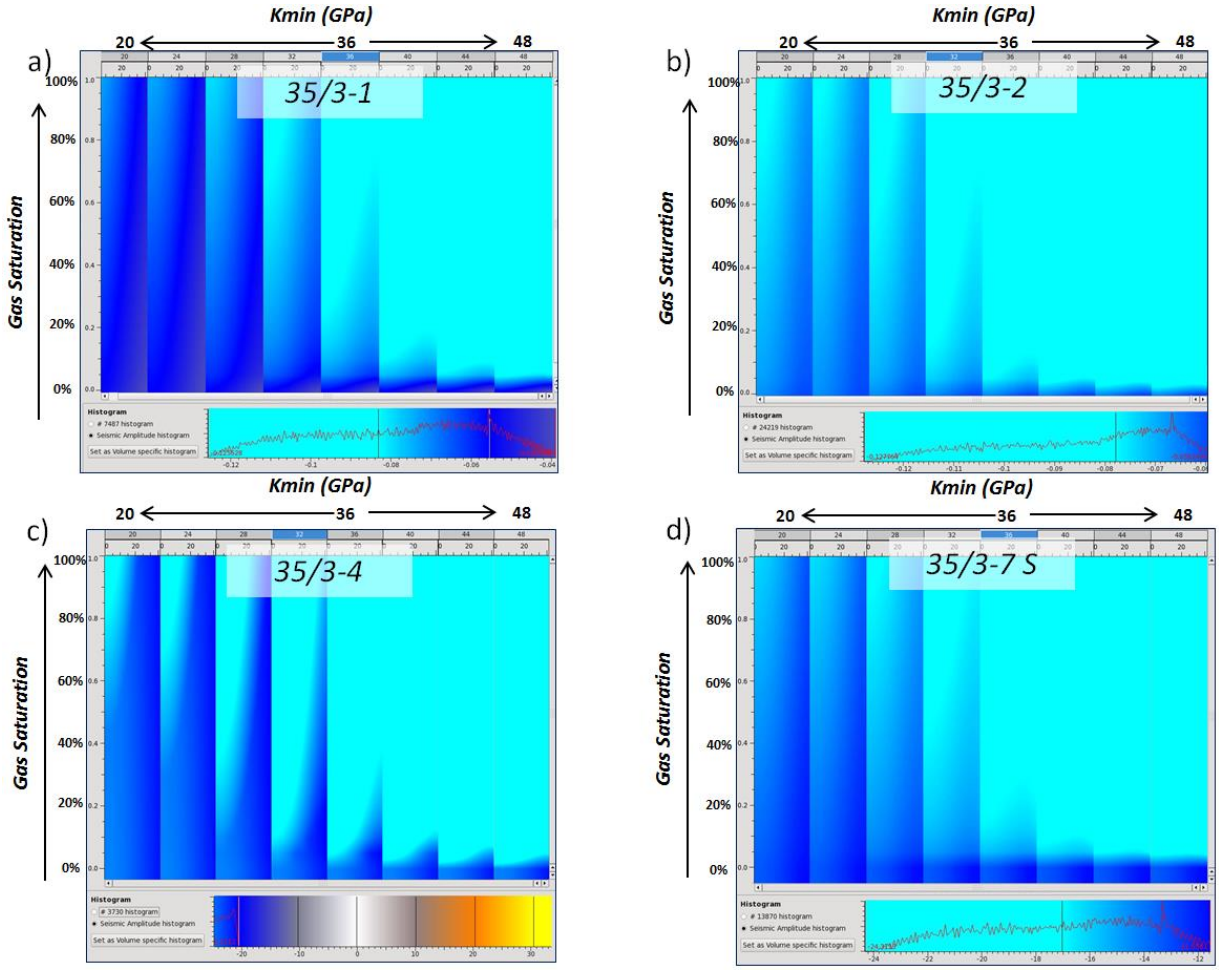

Figure 38: Mineral bulk modulus (Kmin) vs. gas saturation 2D gather maps. For wells: a) 35/3-1; b) 35/3-2; c) 35/3-4 and; c) 35/3-7 S.

A summary of the mineral bulk modulus versus hydrocarbon saturation AVA characteristic results are highlighted in Table 10 and Table 11.

Brine Saturated				
Mineral Bulk Modulus (GPa)	AVA Class	Intercept	Gradient	AVA
Low (20)	IV	Near zero	Positive (almost flat)	Trough decreasing in amplitude with offset very subtly
In situ (36,6)	IV	Near zero	Positive (almost flat)	Trough decreasing in amplitude with offset very subtly
High (48)	IV	Near zero	Positive (almost flat)	Trough decreasing in amplitude with offset very subtly

Table 10: Summary table of how varying mineral bulk modulus impacts the AVA, intercept and gradient characteristics of a brine saturated Agat sand.

Gas Saturated				
Mineral Bulk Modulus (GPa)	AVA Class	Intercept	Gradient	AVA
Low (20)	IV	Negative	Positive	Trough decreasing in amplitude with offset
In situ (36,6)	IV	Very Negative	Positive (almost flat)	Trough decreasing in amplitude with offset very subtly
High (48)	IV	Very Negative	Positive (almost flat)	Trough decreasing in amplitude with offset very subtly

Table 11: Summary table of how varying mineral bulk modulus impacts the AVA, intercept and gradient characteristics of a gas saturated Agat sand.

5.8.4 Thickness vs. Hydrocarbon Saturation

Although the overall Agat succession in the studied wells varies in thickness from 194 m to 402 m, it is in fact made up of numerous sand and shale intervals, which in many cases are thinly bedded and greatly influence the amplitude response. These thin beds are nicely illustrated in the correlation panel in Figure 6 (section 3.1), where the gamma ray response shows sub-seismic resolution sand beds interbedded with shales, particularly in the Agat 80

Member where the majority of the hydrocarbons have been found to date. It is therefore of great importance to understand and model how thickness variations affect the seismic response and whether this is further impacted by hydrocarbon saturation.

To investigate thickness and saturation changes and their effects on the seismic response, two models were generated. The first is illustrated in Figure 39 showing three modelled Agat thickness panels with varying gas saturations for well 35/3-4. Figure 39a illustrates that a 5 m modelled Agat thickness contains a Class IV AVA response across all saturations, with greater gas saturations showing an overall increase in amplitude. A similar story is also true for both the 50 m and 100 m modelled Agat scenarios. However, high gas saturations in the 50 m and 100 m scenarios have greater amplitudes than in the 5 m sand case. Furthermore, a doublet appears in the 50 m and 100 m scenarios where a reflector is introduced. It therefore appears that the marked increase in amplitude above 50% gas saturation in the 50 m and 100 m scenarios appears to be a result of interference/tuning.

The 2D gather maps for thickness vs. gas saturation are displayed in Figure 40 and summarizes some the points stated above. It illustrates that wells 35/3-4 and 35/3-7 S display similar amplitude and AVA characteristics when thickness is varied.

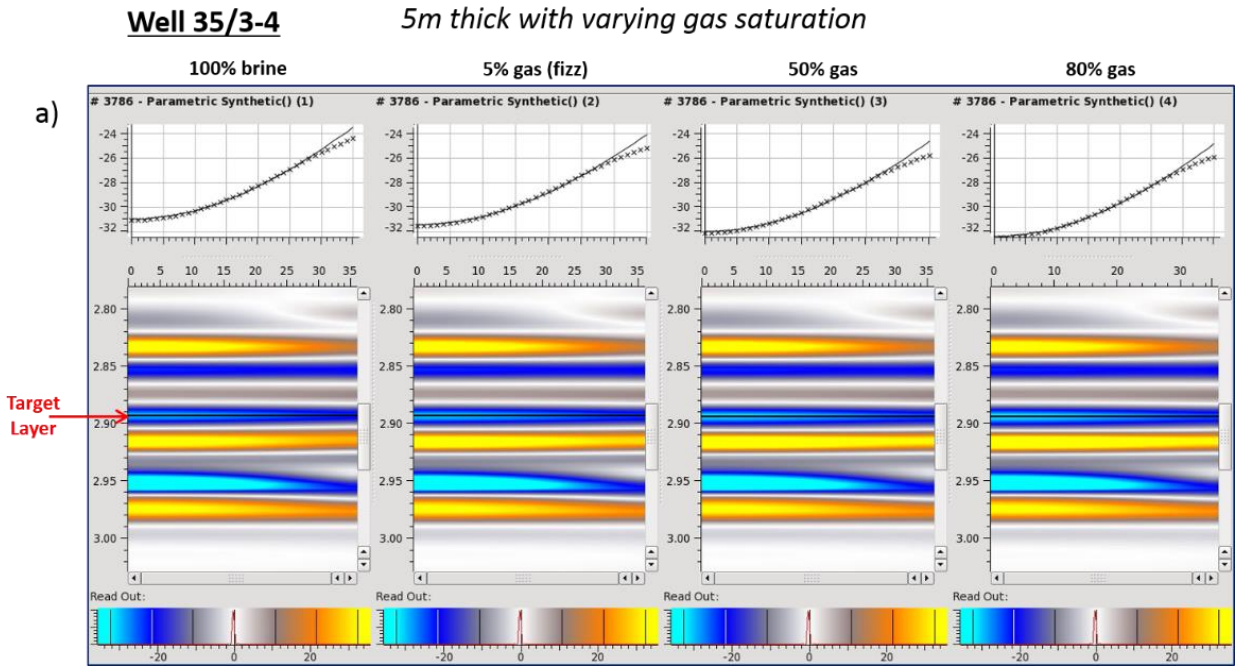

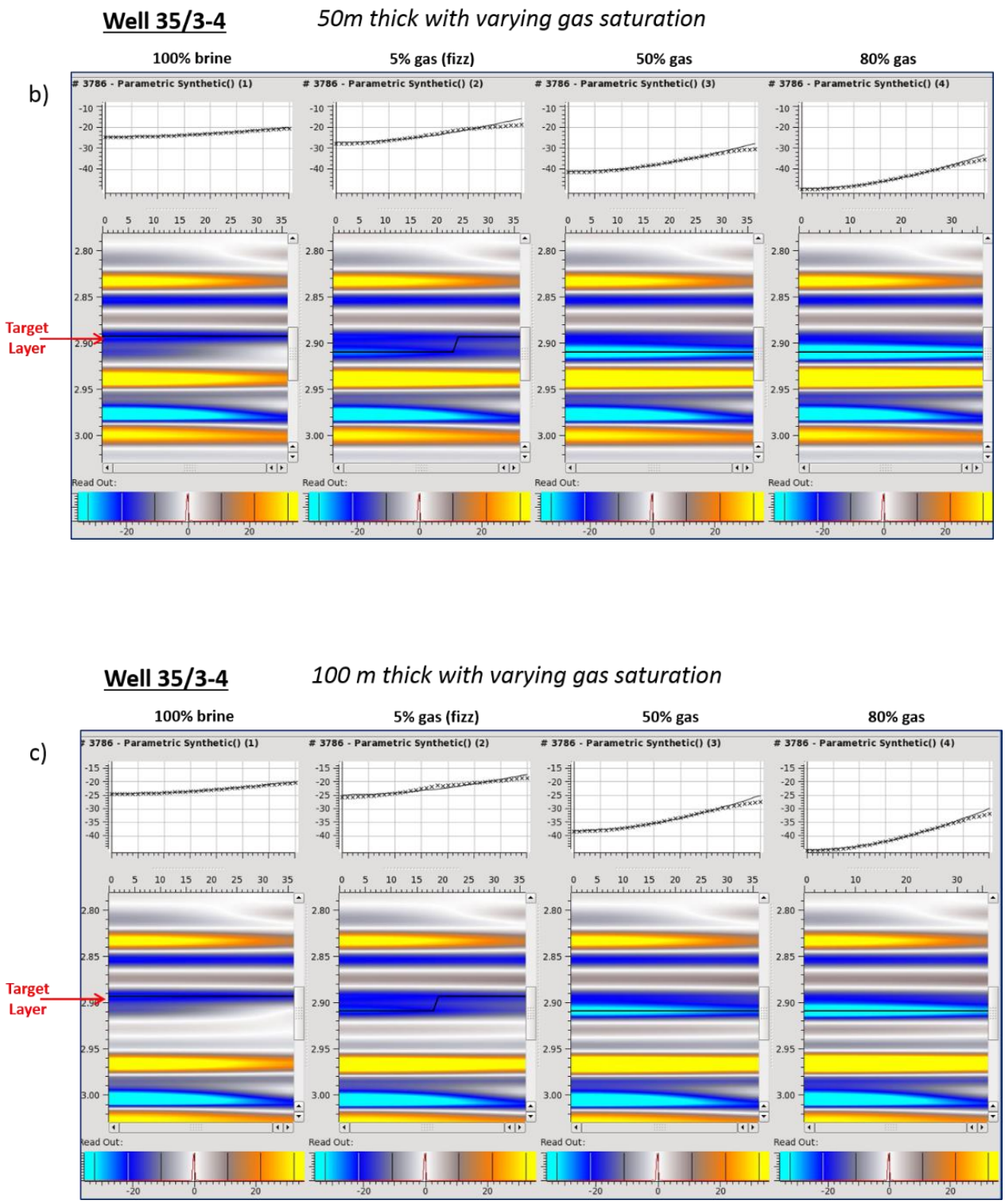

Figure 39: Agat thickness versus hydrocarbon (gas) saturation AVA modelling for the 35/3-4 well. a) 5 m thick; b) 50 m thick; and c) 100 m thick modelled Agat Formation's. 100% brine to 80% gas saturated scenarios are displayed from left to right.

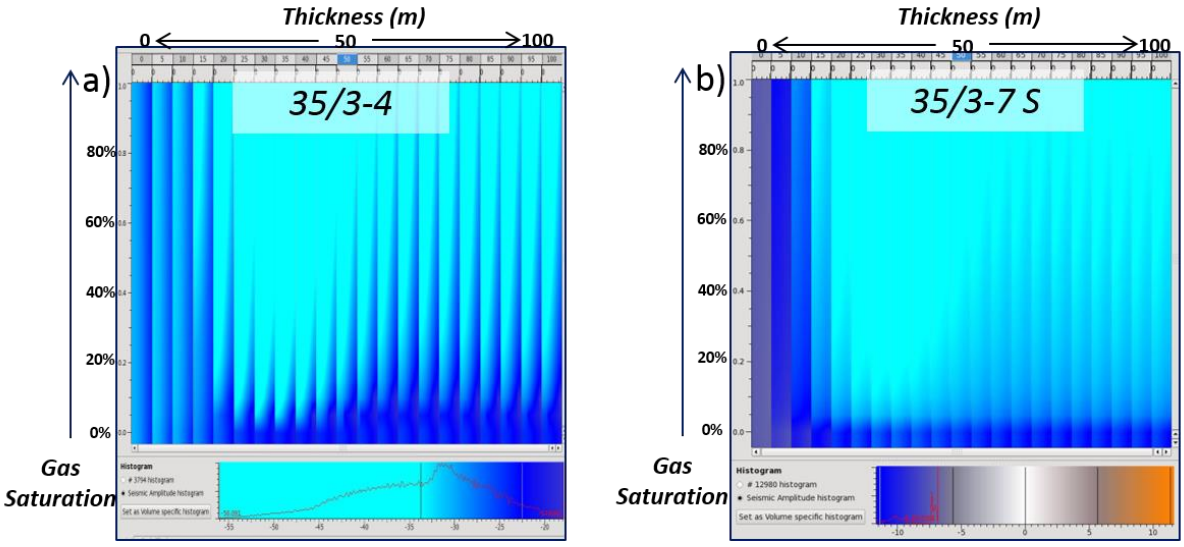

Figure 40: Agat thickness vs. gas saturation 2D gather maps. For wells: a) 35/3-4; and b) 35/3-7 S

To further examine the effects of tuning a series of wedge models were generated for each fluid case to illustrate the interference effects related to the top and base of the modelled Agat 80 Member sandstone. Figure 41 highlights an example from the 35/3-4 well with four different fluid saturations (100% brine, 5% fizz gas, 50% gas and 80% gas). Varying the hydrocarbon saturation demonstrates how increasing gas saturation can impact tuning and the overall seismic amplitude response. Figure 41a) clearly shows the brine Class IV AVA response of the Top Agat Formation which has an overall dimming effect with increasing thickness. Maximum amplitude/tuning effects occur at around 20 m. The 5% gas scenario (Figure 41b) shows a similar response to the 100% brine case, however there is much greater reflectivity in the soft seismic reflector immediately below the Top Agat which is beginning to cause interference. This interference is hugely exemplified in the 50% gas and 80% gas scenarios (Figure 41c and Figure 41d, respectively) where amplitudes are considerably softer and tuning occurs at a greater thickness: approximately 30 m. Below 30 m the amplitude decreases in response to the thinning of the sand.

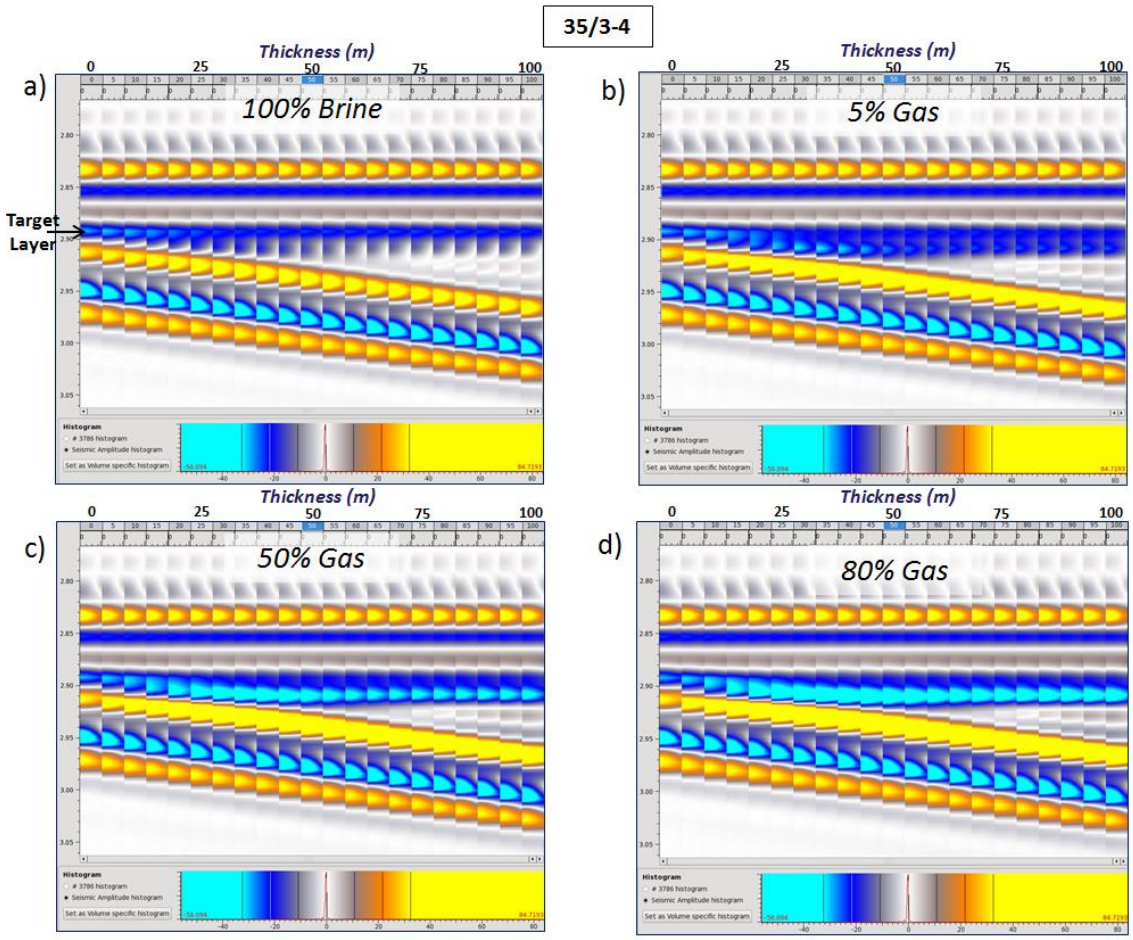

Figure 41: Wedge modelling of the Agat 80 Member in well 35/3-4 for Various Fluid Saturations.

5.9 Extended Elastic Impedance

Extended Elastic Impedance (EEI) logs were created by inputting *Vp*, *Vs* and *density* logs and selecting optimum chi angles for each well respectively. The most suitable chi angle was established by performing a cross-correlation between the log of interest and EEI logs which ranged from -90° to +90° (Figure 42). The best chi angle is represented by the highest correlation coefficient. This process was done for a combination of elastic and petrophysical parameters but only three logs showed strong correlations: *GR*, *Sw* and *Vp/Vs* (Table 12). The EEI correlation scan for well 35/3-2 in Figure 42 shows that the EEI log best fits the *Vp/Vs* ratio log at 36° with the highest correlation coefficient of 1. Furthermore, comparing the EEI curve for *Vp/Vs* with the real *Vp/Vs* log shows striking similarity and provides confidence in the use of the EEI logs at particular angles (note that there is a scaling factor since EEI log units are impedance). However, EEI logs of some wells demonstrated ambiguity, particularly with respect to *VClay* and porosity (*PHIE*), and were therefore

excluded altogether. After establishing reliable chi angles, EEI lithology and fluid volumes were generated along with respective maps relating to the Top Agat Formation.

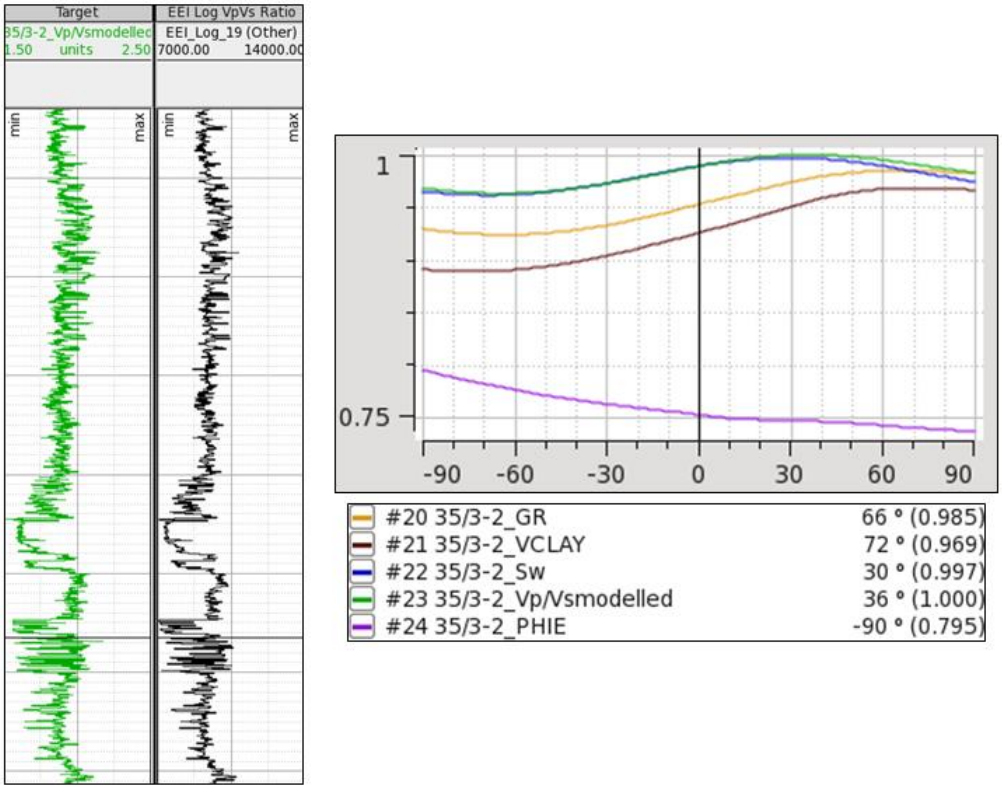

Figure 42: EEI Log Correlation. To the left the green Vp/Vs log is displayed next to the EEI Vp/Vs Log where a strong correlation is observed. The right displays chi angle (x-axis) vs. correlation coefficient (y-axis) where the highest correlation coefficient is 1.

Well Log	Best Match Between Log & EEI Log	Angle (°)
Gamma Ray (GR)	35/3-2	66
Volume Clay (VClay)	-	Too Variable
Water Saturation (Sw)	35/3-1	28
Velocity Ratio (Vp/Vs)	35/3-1 and 35/3-2	36
Effective Porosity (PHIE)	-	No Good Correlation

Table 12: EEI correlation table.

Figure 43 is a composite seismic section through all the studied wells and represents a chi angle of 28° and highlights the fluid effects. Lamé's constant, Lambda, which corresponds to

a chi angle of 20°, is also often implemented as the optimum fluid angle (Goodway et al., 1997) but *Sw* was used since the EEI correlation coefficients were high. Well 35/3-2, which was the Agat discovery well, clearly shows the brightest and most negative amplitudes, giving high confidence in the results. Discovery well 35/3-7 S also shows bright amplitudes, albeit slightly dimmer than the 35/3-2 well. On the other hand, wells 35/3-1 and 35-3-4, which have very low hydrocarbon saturations and are actually classified as dry on NPD, show a very dim to almost neutral amplitude signature, further highlighting the robustness of the results. The attribute map of the Top Agat (Figure 43) shows clusters of bright negative anomalies particularly surrounding the discovery wells. Most of the area nearby well 35/3-4 is in a dim zone and similarly with well 35/-1. Pertaining to the issue of connectivity of reservoirs between wells, there is an evident disconnect of amplitudes between well 35/3-2 and 35/3-7S S.

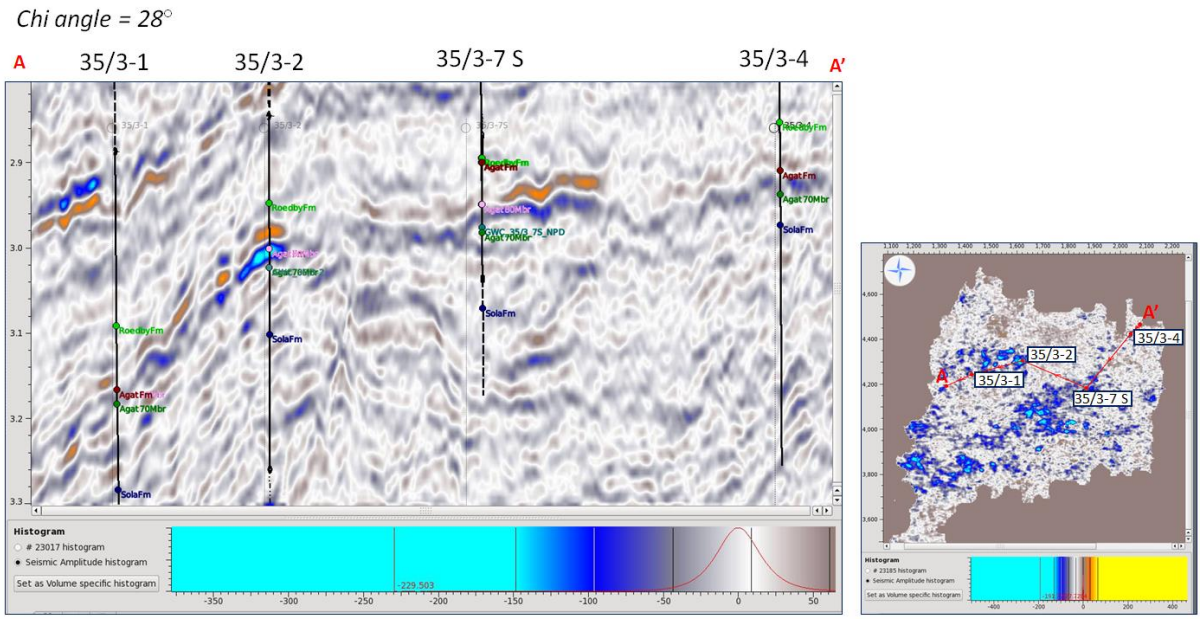

Figure 43: W-E Arbitrary Seismic Section Representing Chi Angle 28°. Soft amplitudes indicate the presence of hydrocarbons which is most strongly observed in the 35/3-2 and 35/3-7 S discovery wells. Dim to transparent amplitudes are observed in the dry 35/3-1 and 35/3-4 wells.

Similarly, Figure 44 demonstrates the *Vp/Vs* ratio given by chi angle 36°. The commonly used chi angle is 45°, especially if no well data is available (Whitcombe et al., 2002). *Vp/Vs* ratio has been proven to be a reliable fluid discriminator in siliciclastic environments since P-wave velocity is sensitive to fluid change in comparison to S-wave velocity (Avseth et al., 2005). The presence of gas will cause a drop in the P-wave velocity relative to the S-wave

velocity and therefore low values allude to the presence of hydrocarbon-bearing reservoirs. However, reservoir quality also affects the ratio where high values correspond to a poor reservoir and low values to a favourable reservoir. The cross-section shows very similar results to chi angle 28° where the discovery wells contain high negative anomalies compared to the dry wells. Both chi angles correlate to the well data but the *Vp/Vs* ratio highlights zones of interest better. An important point to come out of these results are the undrilled fluid indications southwest of the 35/3-7 S that could hold further prospectivity in the area (see chi angle 35° map in Figure 44).

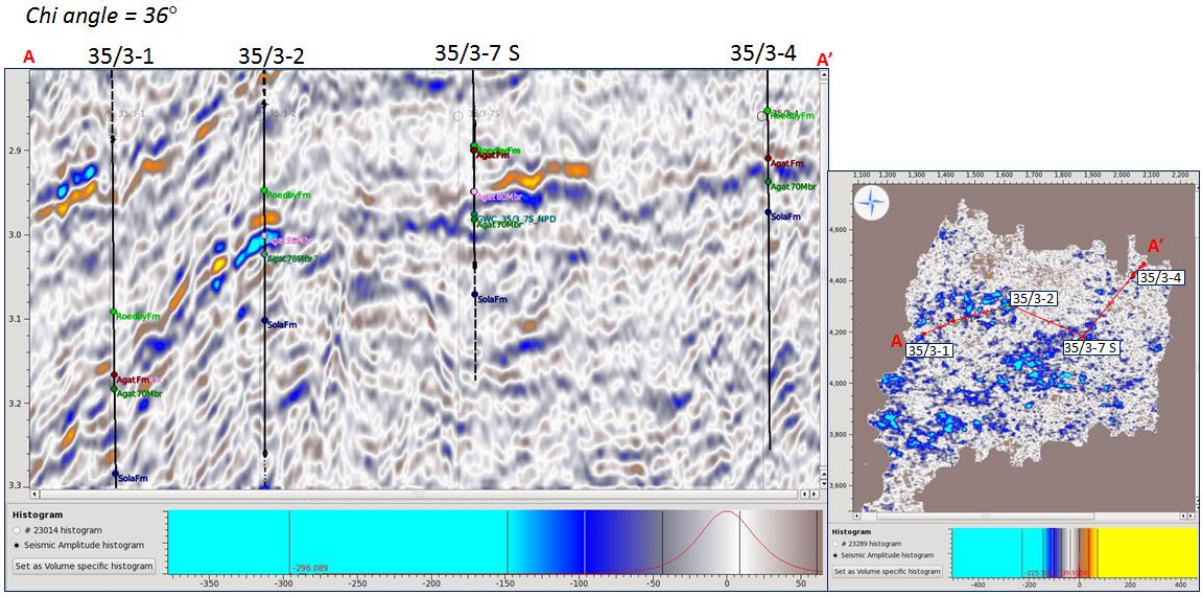

Figure 44: W-E Arbitrary Seismic Section Representing Chi Angle 36°. Shows very similar results as chi angle 28° which is expected since both Sw (chi angle 28°) and Vp/Vs (36°) are used to highlight fluid effects.

Chi angle 66° corresponds to lithology where negative values are sandy portions and positive values are shale. The seismic section in Figure 45 suggests shale is the dominant lithology with interspersed, isolated sand bodies. This also reiterates what is observed in the previous chi angles where well 35/3-2 and 35/3-7S are not linked by fluid or lithology. The attribute map indicates that sand distribution is widespread but does not form a consistent or geological pattern to predict structure or direction of sand bodies. This could be owed to poor seismic data or the nature of the Agat formation or a combination of the two.

A comprehensive view of the three EEI's suggests that extrapolating away from the wells based on the chi angles could be a practical predictive tool. The connection of sand bodies, however, is not compelling but improved seismic data could prove otherwise.

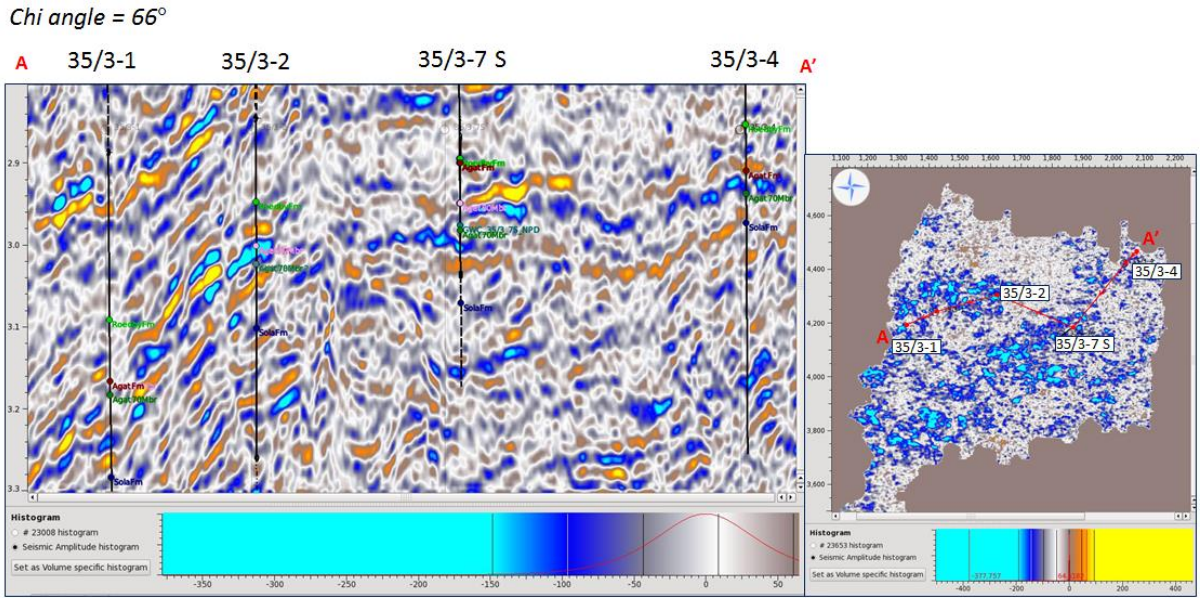

Figure 45: W-E Arbitrary Seismic Section Representing Chi Angle 66°. This is correlated with the Gamma Ray (GR) log with strong negative (soft) amplitudes representing sand.

The Base Agat was mapped in *Pre-Stack Pro*. The method available is a seed point based auto-tracker that can interpret 3D stack or pre-stack data. Picking an event can be controlled by choosing a tracking method and the quality of growing of horizons away from seed points by adjusting various parameters so as to control and guide the horizon. The rationale for interpreting the base was tracking a pervasive hard event that also matches a strong increase in acoustic impedance observed from the logs. An isochron map was created between Top and Base Agat and this gave insight into which areas the formation was thinning or thickening and how it relates to connectivity between wells (see Figure 46). The isochron map shows similarities to the 66° chi angle lithology map (Figure 45) where thick deposits are identified around the 35/3-7 S well and continuing to the southwest. The thin area to the south of the 35/3-1 well is also indicated in both the isochron and chi angle 66° lithology maps. However, to the east there is a miss-match between the isochron map and the chi angle 66° lithology map where thick deposits are expected. This could be due to the eastern portion being more dominated by shale than sand and hence was not identified on the lithology cube. Altogether, it further highlights the potential southwest of 35/3-7 S

where thick deposits coincide with sand deposition from the 66° chi angle lithology map (Figure 45) and fluids from both chi angles 28° (Figure 43) and 36°(Figure 44). This could therefore be an underexplored part of Block 35/3 and could provide additional hydrocarbon volumes to the area.

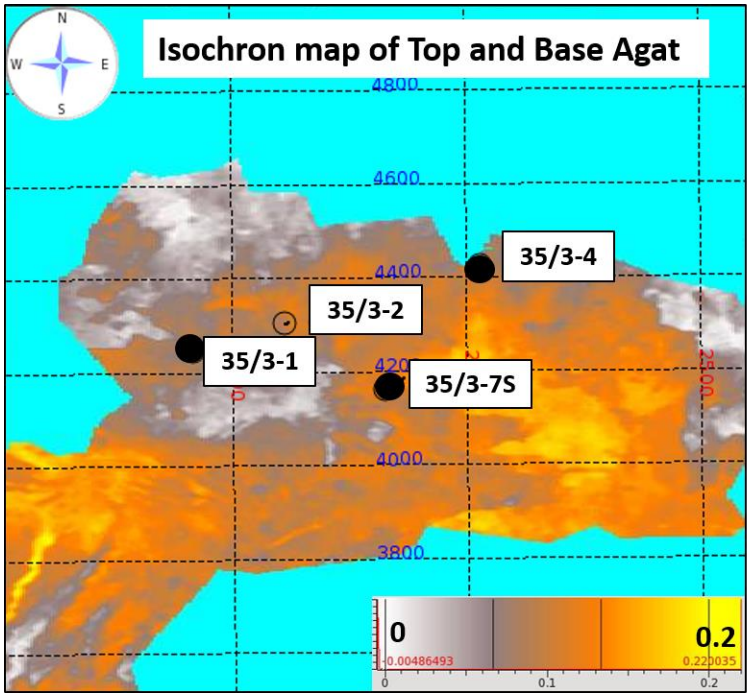

Figure 46: Isochron map from the Top to Base Agat Formation (seconds).

6 Discussion

This thesis compares the amplitude and AVA characteristics of the Agat Formation between 3D AVA models and real seismic data. It also presents a comprehensive Extended Elastic Impedance study which extrapolates fluid and lithology effects away from wells. Major findings show that the modelled in situ AVA responses for wells 35/3-1, 35/3-4 and 35/3-7 S were conformant to a Class IV AVA response. This was consistently observed not only on the modelled response but also on well synthetic seismograms and real seismic gathers for brine, oil and gas cases. However, one exception was identified when comparing the 35/3-2 well. In this case, the modelled Class IV AVA response of the 35/3-2 well matched the well synthetic seismogram but not the real seismic gather, which on the contrary revealed a Class III. The reason for the discrepancy is not fully known, however, the modelled results showed that an anomalously high cap rock P-wave velocity can result in a Class III Agat

Formation and this may be the reason for why it was observed in well 35/3-2 on real seismic data. Therefore, there is likely a discrepancy between the P-wave velocities recorded in the overlying shale in the well data compared to the seismic velocities.

Additional findings from the thesis show that a hydrocarbon-filled Agat Formation should consist of a Class IV AVA response with softer amplitudes correlating to increased hydrocarbon saturations. These should be distinguishable from a brine-filled sand response, which according to the varying physical parametric multi-angle AVA models, should be starkly dimmer and with a flatter AVA Class IV response that is close to the Class III/IV boundary. Furthermore, the effect of porosity is clearly observed in the hydrocarbon saturated scenarios, particularly when porosity values are greater than 14%, as a prominent class IV AVA response becomes evident. A further generality can be made regarding the P-wave velocity of the cap rock; a hard Agat response can be solely linked to a 100% brine-filled sand underlying a soft shale – thus a prospect with a hard Agat response is unfortunately most likely to be dry or at least containing <5% hydrocarbon saturation. Modelling the mineral bulk modulus had negligible impact on the brine-filled scenario. However, variations of mineral bulk modulus with hydrocarbon saturation showed that shaley sands (low *Kmin* values) contained dimmer amplitudes than default sandstone mineral bulk modulus values. On the other hand, shaley sands did show a more pronounced positive gradient, and thus Class IV AVA response, than its sandy counterpart.

The Extended Elastic Impedance studies recapitulates the complexities of the Agat Formation and the imaging thereof. The fluid and lithology maps indicate poor connectivity surrounding the wells and between the wells. Distinct geological patterns of sand bodies, such as channels and lobe structures, were not visible from these maps even though they are often accentuated by EEI studies of 3D seismic datasets. The EEI maps concur with the isochron map for the most part in that thicker areas relate to brighter amplitudes on both the fluid and lithology cubes, particularly southwest of well 35/3-7 S. In areas where the isochron thins, a disconnect of EEI amplitudes was observed. These finding reiterate the fact that already drilled wells have shown no pressure connection and hence compartmentalization and/or poor connectivity of sand bodies is prevalent. However, there may also be other reasons for the sporadic distribution of amplitudes such as seismic image quality. This raises the question if reprocessing is necessary to enhance seismic imaging

along with an improved velocity model which could potentially homogenize the AVA character of well 35/3-2 to that of the rest of the wells which all show a class IV AVA response.

No geophysical current research or literature exists in the public domain today and therefore it is impossible to demonstrate whether the results are broadly consistent or contradictory with existing research or not. This is therefore, the first study, to my knowledge, to examine the AVA characteristics of the Agat Formation. Although this study is conducted in one region around the Agat Field, the results can be generalizable to other areas, particularly to the south in the surrounding area of the recent 36/7-4 Cara discovery well where similar reservoir and cap rock properties are expected. It also provides exploration geophysicists with a thorough analysis of how varying elastic properties impact the amplitude and AVA response of the Agat Formation.

Limitations of this study primarily relate to seismic image quality, geological complexity and constraints of only having *Pre-Stack Pro* at hand. Seismic image quality is critical for direct hydrocarbon indicator (DHI) analysis and although *Sharp Reflections* undertook a comprehensive seismic data conditioning procedure prior to this study, the data still proved challenging as internal imaging of the Agat Formation remained discontinuous and noisy. Regarding geological complexity, this is something that cannot be altered and the aim of a geologist and/or geophysicist is to unravel such complexities. In the case of the Agat Formation, the channel sands, their connectivity, and reservoir properties resulted in a very intricate depositional system. This coupled with limited seismic quality is one of the reasons why the Agat Formation has remained so enigmatic and underexplored and may also be the reason for some of the variations in amplitude and AVA effects between wells. Although such complexities and ambiguities were present, this study has attempted to maximise the AVA information from the dataset. Lastly, even though *Pre-Stack Pro* is a state-of-the-art software that enables the combined use of pre-stack visualisation, processing, and interpretation in one platform, it does still have its limitations particularly with regards to fluid substitution. Fluid substitution in *Pre-Stack Pro* is relatively simplified and does not allow for a rigorous quality control or detailed thin bed analysis, which leads nicely on to the topic of further studies.

Future studies are recommended particularly regarding thin beds and shaley sand analysis of the Agat Formation. Although shaley sand AVA effects were investigated in this thesis by reducing mineral bulk modulus values, a more detailed analysis could be done. This is because tight sands and shaley sands are scenarios in which it is possible that Gassmann's assumptions are violated. A common pitfall in the fluid substitution of shaley sands is an exaggerated substitution effect on the compressional velocity and Poisson's ratio logs in low porosity shale-prone zones (e.g. Skelt, 20014; Simm, 2007). The Thomas Stieber (1975) algorithm could be one approach to overcome this as it can be used to determine the amount of dispersed, structural and laminated shale and the porosity and *Vshale* of the sand layers. The results can then be incorporated in the dry rock modelling stage of fluid substitution. Also, the creation of intercept and gradient volumes from models could be one avenue of development as it allows for the generation and interpretation of time slices through the target layer enabling a comparison to real seismic data.

Future research applications following the work done in this research could be implemented by using different pairs of reservoir parameters such as pressure verses hydrocarbon saturation changes as a use for AVA methods to determine time-lapse changes in 4D seismic and production related geophysics.

7 Conclusion

For the first time, a comparison between well derived 3D AVA synthetic models and real seismic data has been documented along with its sensitivity to varying physical parameters for the Agat Formation. A Class IV AVA character is evident in all of the 3D synthetic models within Block 35/3 and a similar response is expected out with the study area. This modelled Class IV response was observed on real seismic data for 3 out of the 4 studied wells.

The generation of multi-angle AVA models with different combinations of physical parameters plotted against hydrocarbon saturation, in a data slice format, allowed for key relationships to be distinguished:

- Variations in porosity in gas-filled sands had little impact on near angle amplitudes but an increasingly prominent AVA Class IV response was observed with increasing porosity values. With regards to brine saturated sands, porosity had no impact on

the overall amplitude response and the AVA effect was altogether reduced to a relatively flat response between Class III and Class IV.

- Subtle variations of the P-wave velocity of the overlying shale unit by as little as +/- 300 ms^{-1} (7.5%) showed a significant impact on the amplitude response. The brine-fill scenario in particular shows a clear polarity reversal at low P-wave velocity values whereas high values make brine and hydrocarbons sands impossible to discriminate and very high values show transitioning from a Class IV to a Class III AVA response.
- Low mineral bulk modulus values (i.e. shaley sands), revealed lower amplitudes than high mineral bulk modulus values (i.e. clean sands – 36.6 GPa). However, similar to porosity, mineral bulk modulus had negligible impact on brine-filled sands and the Class IV AVA character was much reduced in comparison to hydrocarbon cases.
- Lastly, variations in thickness highlighted subtle thin bed and tuning effects associated with the Agat Formation. It also confirmed the textbook thickness versus composite amplitude relationship for the 35/3-4 and 35/3-7 S wells and raised the point that below tuning thickness the brine and gas responses were all comparable.

The AVA models demonstrate that minor changes in physical parameters result in relatively large changes in amplitude and AVA character, thus highlighting the sensitivity and complexity of the Agat Formation. This was further portrayed in the EEI modelling where chi angle cubes of lithology and fluid showed isolated sand bodies and isolated hydrocarbon responses, however, further exploration potential was identified southwest of well 35/3-7 S.

8 References

Aki, K, and Richards, P.G. (1980). Quantitative seismology: Theory and methods: W.H. Freeman and Co.

Avseth, P., Mukerji, T., and Mavko, G. (2005). Quantitative seismic interpretation: Applying rock physics tools to reduce interpretation risk: Cambridge University Press.

Badley, M. E, and L. C. Backshall. (1989). Inversion, reactivated faults and related structures: Seismic examples from the southern North Sea, *Geol. Soc. London Spec. Publ.,* **44**, 201–21.

Badley, M. E, Price, J.D, Rambech D.C, and Agdestein, T. (1988), The structural evolution of the northern Viking Graben and its bearing upon extensional modes of basin formation, *J. Geol. Soc.,* **145**, 455–472.9.

Batzle., M. L., and Wang, Z. (1992). Seismic properties of pore fluids. *Geophysics.*, **57**, 1396–1408.

Bell, R. E, Jackson, C. A. L, Elliott, G.M, Gawthorpe, R. L, Sharp, I. R., and Michelsen, L. (2014), Insights into the development of major rift-related unconformities from geologically constrained subsidence modelling: Halten Terrace, offshore mid Norway, *Basin Res,* **26**, 203–224.

Brown., A. R. (2011). Interpretation of three dimensional seismic data. 7th Edition, AAPG Memoir 42, SEG Investigation No. 9.

Bugge, T, Tveiten, B, and Bäckström, S. (2001). The depositional history of the Cretaceous in the northeastern North Sea. In: Martinsen, O. & Dreyer, T. (eds.) Sedimentary Environments Offshore Norway – Paleozoic to Recent. *Norwegian Petroleum Society Special Publication,* **10,** 279-291.

Castagna, J.P., Batzle, M.L. and Eastwood, R.L. (1985). Relationships between compressional wave and shear-wave velocities in clastic silicate rocks. *Geophysics.*, **50**, 571-581.

Castagna, J.P., and Swan, H.W. (1997). Principles of AVO crossplotting. *The Leading Edge.*, **16**(4), 337-344.

Castagna, J.P, Swan, H.W, and Foster, D.J. (1998). Framework for AVO gradient and intercept interpretation. Geophysics, Vol 63, No. 3. 948-956.

Chiburis, E., Franck, C., Leaney, S., McHugo, S., and Skidmore, C. (1993). Hydrocarbon detection with AVO. *Oilfield Review*., **6**, 42– 50.

Connolly, P. (1998). Calibration and inversion of non-zero offset seismic: 68th SEG Annual Meeting, New Orleans, USA. *Expanded Abstracts.*, 182-184.

Connolly, P. (1999). Elastic Impedance, *The Leading Edge* **18**(4), 438-352.

Fatti, J.L., Smith, G.C., Vail, P.J., Strauss, P.J., and Levitt, P.R., 1994, Detection of gas in sandstone reservoirs using AVO analysis: A 3-D seismic case history using the Geostack technique. *Geophysics*., **59**, 1362-1376.

Færseth, R.B. (1996) Interaction of Permo–Triassic and Jurassic extensional fault-blocks during the development of the northern North Sea. J. Geol. Soc., **153**, 931–944

Færseth, R. B, and R. Ravnås. (1998). Evolution of the Oseberg fault-block in context of the northern North Sea structural framework, *Mar. Pet. Geol*, **15**, 467–490.

Gassmann, F. (1951). Uber die elastizitat poroser medien: Vierteljahrsschrift der Naturforschenden Gesselschaft., **96**, 1–23.

Gabrielsen, R.H, Kyrkjebø, R, Faleide, J.I, Fjeldskaar, W, and Kjennerud, T. (2001). The Cretaceous post-rift basin configuration of the Northern North Sea. *Petroleum Geoscience*, **7**, 137-154.

Gabrielsen, R. H, Færseth, R. B, Steel, R. J, Idil, S, & Klovjan, O. S. (1990). Architectural styles of basin fill in the northern Viking Graben. Unknown Journal, 158-179.Færseth, R. B. 1996, Interaction of Permo-Triassic and Jurassic extensional fault-blocks during the development of the northern North Sea, *J. Geol. Soc.*, **153**, 931–944.

Geertsma, J., and Smit, D. C.(1961). Some aspects of elastic wave propagation in fluid saturated porous solids, *Geophysics*., **26**, 169-181.

Gulbrandsen, A. (1987). Agat Field. In: Spencer, M.A. (ed.) Geology of the Norwegian oil and gas fields: Graham and Trotman, London, 363-370.

Greenberg, M. L., and Castagna, J.P. (1992). Shear-wave velocity estimation in porous rocks: Theoretical formulation, preliminary verification and applications. *Geophysical Prospecting.*, **40**, 195–209.

Han, D.H., and Batzle, M. L. (2004). Gassmann's equation and fluid-saturation effects on seismic velocities. *Geophysics.*, **69,** 398-405.

Hilterman, F. (1990). Is AVO the seismic signature of lithology? *The Leading Edge.*, **9** (6), 15-22.

Isaksen, D., and Tonstad, K. (1989). A revised Cretaceous and Tertiary lithostratigraphic nomenclature for the Norwegian North Sea. *Norwegian Petroleum Directorate Bulletin,* **5**, 1-59.

Lee, M.W. (2008). Comparison of the modified Biot-Gassmann theory and the Kuster-Toksöz Theory in Predicting Elastic Velocities of Sediments. *Scientific Investigations Report.*, 2008-5196

Martinsen, O.J., and Dreyer, T. (2001). Sedimentary environments offshore Norway—Palaeozoic to Recent, *Norwegian Petroleum Society Special Publication*, **10**, 490 pp.

Martinsen, O.J., Lien, T,, and Jackson, C.A.L. (2005). Cretaceous and Palaeogene turbidite systems in the North Sea and Norwegian Sea Basins: source, staging area and basin physiography controls on reservoir development. *In* Doré, A.G. & Vining, B.A (eds.): Petroleum geology: North-West Europe and global perspectives, Proceedings of the 6th petroleum geology conference, *Geological Society of London,* 1147–1164.

Mavko, G., T. Mukerji, and J. Dvorkin, 2009, The rock physics handbook: Cambridge University Press.

Miller, K.G., Kominz, M.A., Browning, K.V., Wright, J.D., Mountain, G.S., Katz, M.E., Sugarman, P.J., Crames, B.S., Christie-Blick, N., and Pekar, S.F. (2005). The Phanerozoic record of global sea-level change. *Science*., **310**, 1293-1298.

Nystuen, J.P. (1999). Submarine sediment gravity flow deposits and associated facies: core examples from the Agat Member. Extended Abstracts Bergen Conference. *Norwegian Petroleum Society,* 211-215.

Øvrebø, L.K., Kjennerud, T., Lippard, S.J., Rivenæs, J.C., and Hamborg, M. (2001). Forward depositional modelling of the Cretaceous post-rift deposits in the northern North Sea, *Norsk Geol. Tidskr.,* **81**, 169-178.

Rattey, R. P, and Hayward, A. B. (1993). Sequence stratigraphy of a failed rift system: the Middle Jurassic to Early Cretaceous basin evolution of the Central and Northern North Sea. In Parker, J. R. (ed.): Petroleum Geology of Northwest Europe: Proceedings from the 4th Conference, *Geol. Soc. London.*, 215-249.

Reeve, M.T., Bell, R.E., Duffy, O.B,, Jackson, C.A.L, and Sansom, E. (2015). The growth of non-collinear normal fault systems; what can we learn from 3D seismic reflection data? *Journal of Structural Geology.*, **70**, 141-155.

Ross, C.P., and Kinman, D.L. (1995). Nonbright-spot AVO; two examples. *Geophysics*., **60**, 1398- 1408.

Royle, A.J. , Logel, J.D., and Lines, L.R. (2002). Hebron/Ben Nevis rock property analysis and modelling study. *CREWES Research Report.,* **14.**

Russel, B.H., Lines, L.R., Hirsche, K.W., and Peron, J. (2000). The AVO modelling volume. *CREWES Research Report.*, **12**.

Rutherford, S.R., and Williams, R.H. (1989). Amplitude-versus-offset variations in gas sands. *Geophysics*., **54**(6), 680-688.

Shanmugam, G., Bloch, R.B., Mitchell, S.M., Beamish, G.W.J., Hodgkinson, R.J., Damush, J.E., Straume, T., Syvertsen, S.E., and Shields, K.E. (1995). Basin-floor fans in the North Sea: sequence stratigraphic models vs. sedimentary facies. *American Assoc. Pet. Geol. Bull.,* **79**, 477-512.

Shanmugam, G., Lehtonen, L.T., Straume, T., Syversten, S.E., Hodgkinson, R.J., and Skibeli, M. (1994). Slump and debris flow dominated upper slope facies in the Cretaceous of the

Norwegian and Northern North Seas (61º–67º N): implications for sand distribution. *AAPG Bulletin.*, **78**, 910–937.

Sheriff, R.E. (1997). Seismic resolution: A key element. *AAPG December Explorer.*

Simm, R.W. (2009). Simple net pay estimation from seismic: a modelling study. *First Break*., **25** (12), 39-46.

Simm, R., and Bacon, M. (2014). Seismic amplitude an interpreter's handbook. UK: Cambridge University Press.

Simm, R. (2007). Practical Gassmann fluid substitution in sand/shale sequences. *First Break*., **25**(12), 61-68.

Skelt, C. (2004). Fluid substitution in laminated sands. *The Leading Edge*., **23**, 485-493

Smith, G.C., and Gidlow, P.M. (1987). Weighted stacking for rock property estimation and detection of gas: *Geophysical Prospecting.*, **35**, 993-1014.

Shuey, R.T. (1985). A simplification of the Zoeppritz equations: Geophysics, **50**, 609-614.

Skibeli, M., Barnes, K., Straume, T., Syversen, S.E: and Shanmugam, G. (1995). A sequence stratigraphic study of Lower Cretaceous deposits in the northernmost North Sea. In: Steel, R. et al. (eds.) *Norwegian Petroleum Society Special Publication,* **5**, 389-400.

Thomas, E. C., and Stieber, S.J. (1975). The distribution of shale in sandstones and its effect upon porosity: 16th Annual Logging Symposium, SPWLA, Paper T.

Underhill, J. R, and Partington, M. A. (1993). Jurassic thermal doming and deflation in the North Sea: implications of the sequence stratigraphic evidence. In Parker, J. R. (ed.): Petroleum Geology of Northwest Europe: Proceedings of the 4th Conference, *The Geological Society, London,* 337-345.

Underhill, J. R, and Partington, M. A. (1994). Use of genetic sequence stratigraphy in defining and determining a regional tectonic control on the "mid-Cimmerian unconformity": Implications for North Sea basin development and the global sea-level chart. *In* Weimer, P, and Posamentier, H, eds, Siliciclastic sequence stratigraphy: *AAPG Memoir*, **58**, 449-484.

Vergara, L., Brunstad, H., Nordlie, T., Charnock, M.A., and Gradstein, F.M. (2006). Agat Formation. RWE-DEA Norge.

Wang, Z., and Nur, A. (1992). Seismic and acoustic velocities in reservoir rocks, 2: Theoretical and model studies. *Soc. Expl. Geophys.*

Whitcombe, D. (2002). Elastic impedance normalization. *Geophysics.*, **67**(1), 60–62.

Whitcombe, D.N., P.A. Connolly, R.L. Reagan, and T.C. Redshaw. (2002). Extended elastic impedance for fluid and lithology prediction. *Geophysics*., **67**(1), 63-67.

Widess, M.B., 1973, How thin is a thin bed?. *Geophysics.,* **38**, 1176-1180

Ziegler, P.A. (1975). Geological evolution of the North Sea and its tectonic framework, *AAPG Bulletin,* **59**, 1073-1097.

Zoeppritz, K. (1919). VIIb. Über Reflexion und Durchgang seismischer Wellen durch Unstetigkeitsflächen. [VIIb. On reflection and transmission of seismic waves by surfaces of discontinuity], Nachrichten von der Königlichen Gesellschaft der Wissenschaften zu Göttingen, *Mathematisch-physikalische Klasse.*, 66–84.

9 Appendix

The appendix mainly consists of the 3D parametric modelling results of all the studied wells that were not incorporated into the main body of the thesis. Since the thesis showed example figures from individual wells rather than all wells at once, it is important to highlight the same results for all wells. These are shown in section 9.2.1 to 9.2.3.

Furthermore, the main body of the thesis primarily showed brine and gas saturated results to avoid oversaturating the reader with figures and information. The oil saturated results are therefore displayed in the appendix from section 9.2.4 to 9.2.7. The reader will notice that the oil scenarios produce similar results to that of the gas scenarios described in the main text. It is also noted that the amplitude response for both oil and gas are very similar and therefore discriminating between the two appears to be very difficult.

9.1 Forward Modelling

The modelled Agat 80 interval for wells 35/3-2, 35/3-4 and 35/3-7 S are displayed below in Figure 47, Figure 48 and Figure 49, respectively. Note that the modelled interval for the 35/3-1 well is displayed in the main body of the thesis in Figure 25, section 5.6.

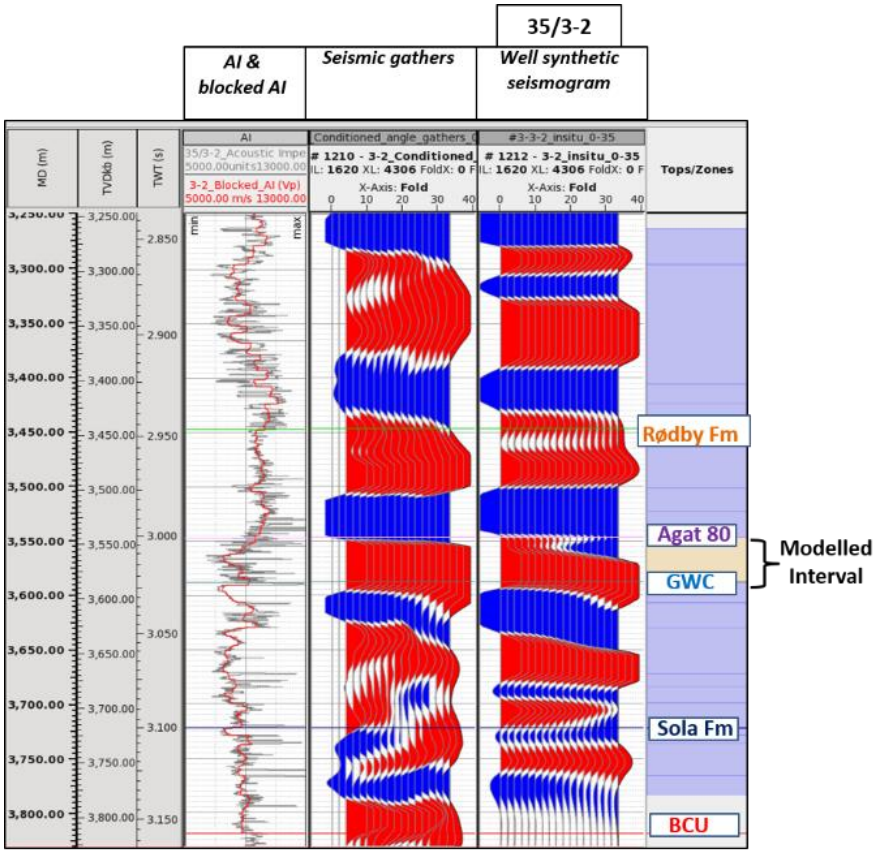

Figure 47: Zone definition and modelled interval of the 35/3-2 well. A comparison between the in situ seismic gather and in situ well synthetic seismogram is shown and illustrates a good match between the two.

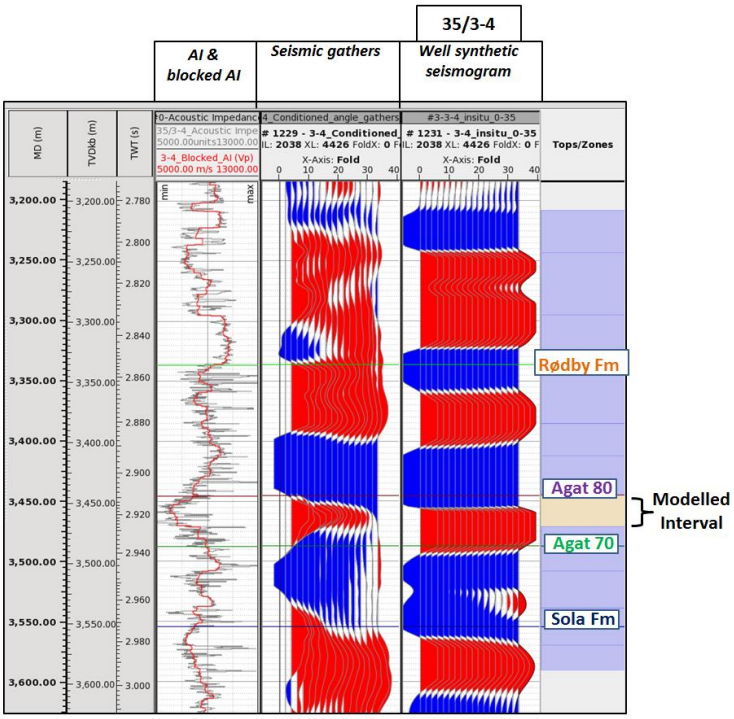

Figure 48: Zone definition and modelled interval of the 35/3-4 well. A comparison between the in situ seismic gather and in situ well synthetic seismogram is shown and illustrates a good match between the two.

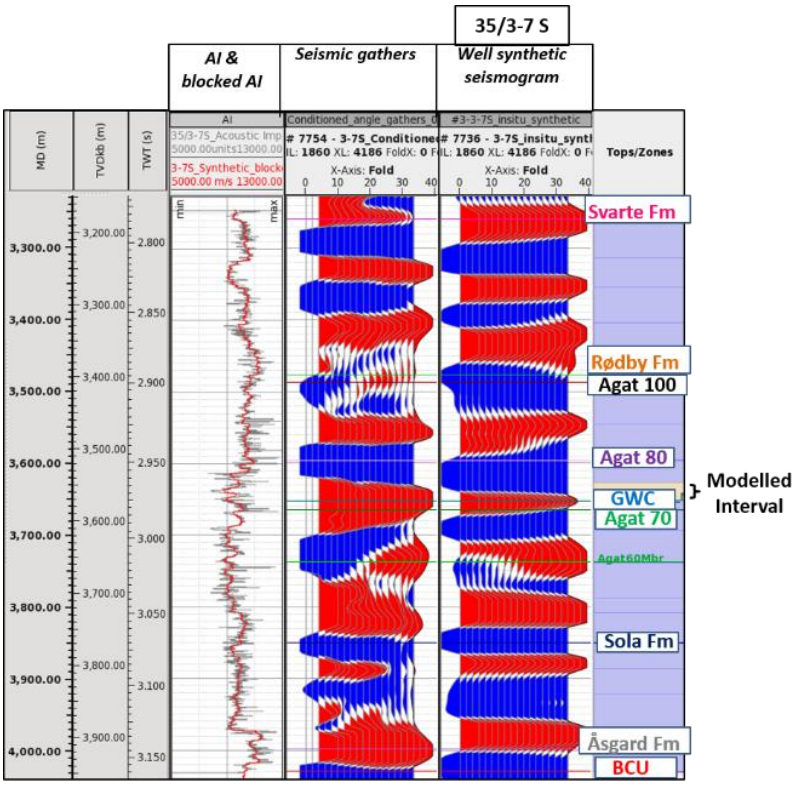

Figure 49: Zone definition and modelled interval of the 35/3-7 Swell. A comparison between the in situ seismic gather and in situ well synthetic seismogram is shown and illustrates a good match between the two.

9.2 3D Parametric Modelling

9.2.1 Porosity vs. Hydrocarbon Saturation (Gas Case)

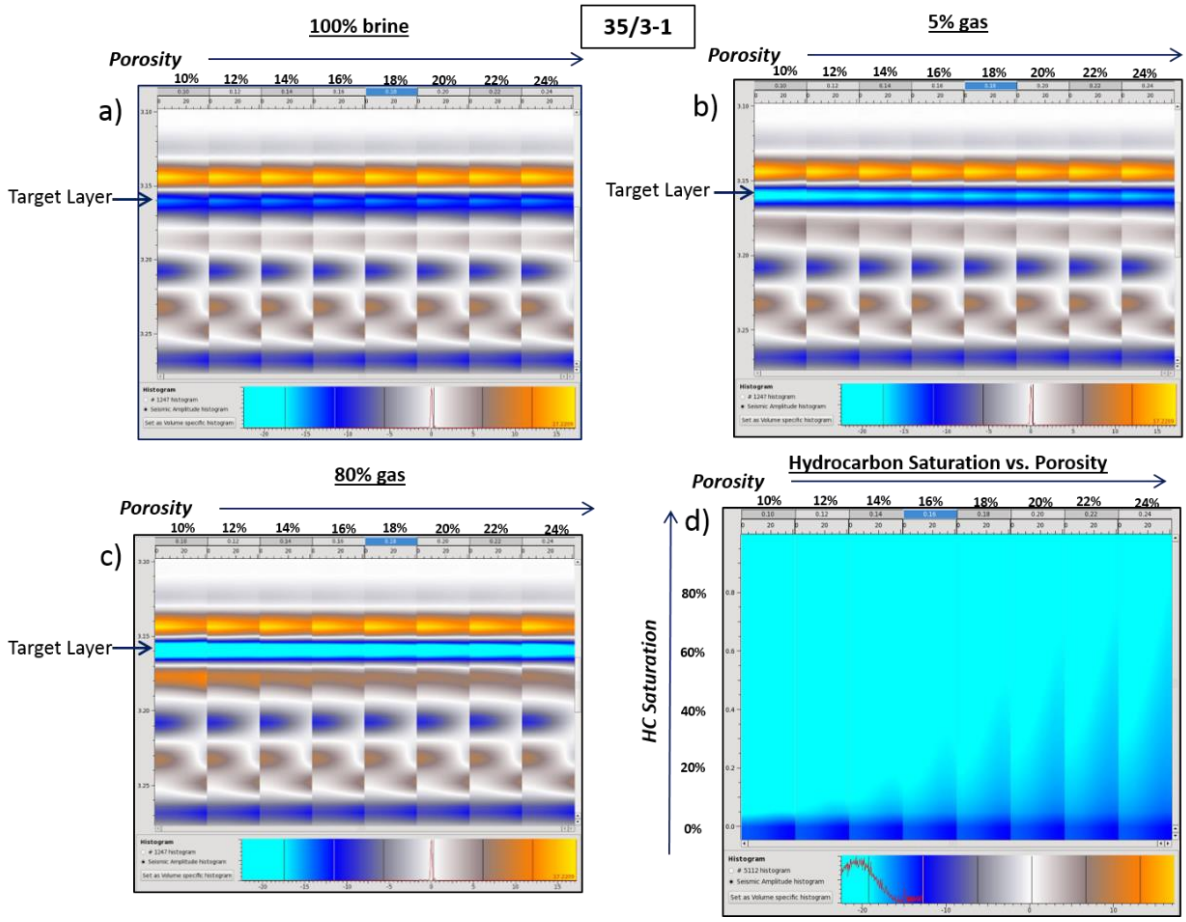

Figure 50: AVA modelling of porosity vs. gas saturation for the 35/3-1 well. a) Brine saturated; b) 5% gas saturated; and c) 80% gas saturated with porosity increasing from left to right. d) Shows a 2D gather map of porosity vs. HC (gas) saturation.

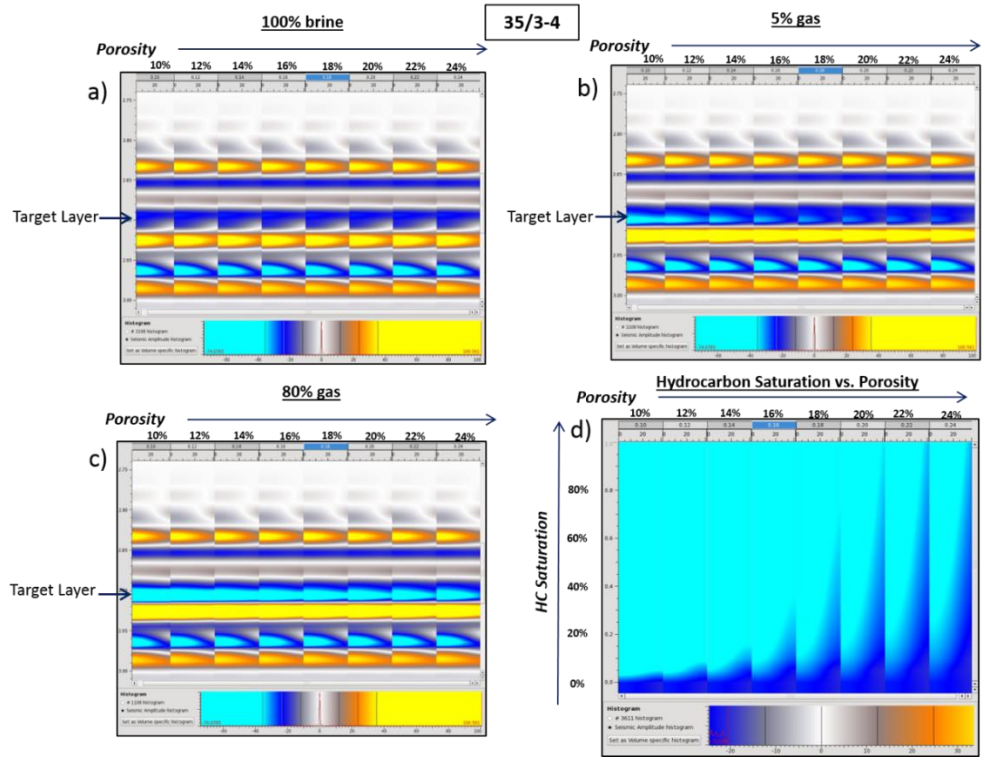

Figure 51: AVA modelling of porosity vs. gas saturation for the 35/3-4 well. a) Brine saturated; b) 5% gas saturated; and c) 80% gas saturated with porosity increasing from left to right. d) Shows a 2D gather map of porosity vs. HC (gas) saturation.

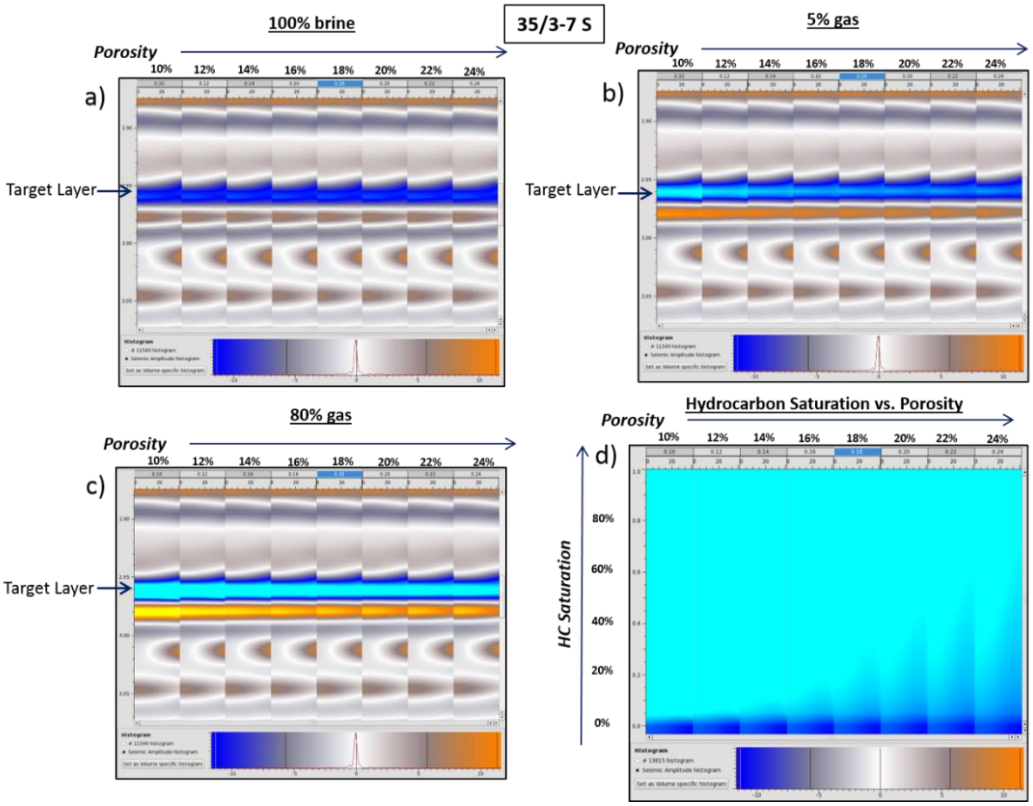

Figure 52: AVA modelling of porosity vs. gas saturation for the 35/3-7 S well. a) Brine saturated; b) 5% gas saturated; and c) 80% gas saturated with porosity increasing from left to right. d) Shows a 2D gather map of porosity vs. HC (gas) saturation.

Figure 50, Figure 51 and Figure 52 above, displays the 3D parametric models of porosity vs. hydrocarbon saturation for wells 35/3-1, 35/3-4 and 35/3-7 S. All the studied wells show similar amplitude and AVA effects as the 35/3-2 described in section 5.8.1 (Figure 32 and Figure 33). The reader is therefore diverted back to this section for further explanation of the results.

9.2.2 P-wave Velocity vs. Hydrocarbon Saturation (Gas Case)

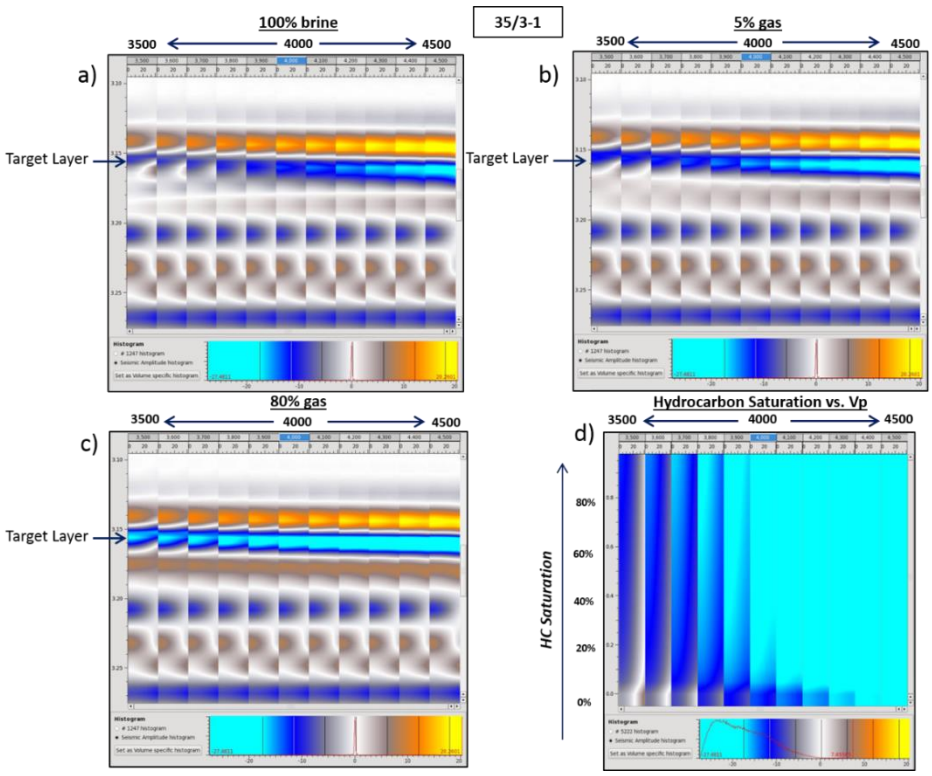

Figure 53: AVA modelling of P-wave velocity (Vp) of the overlying shale vs. gas saturation for the 35/3-1 well.

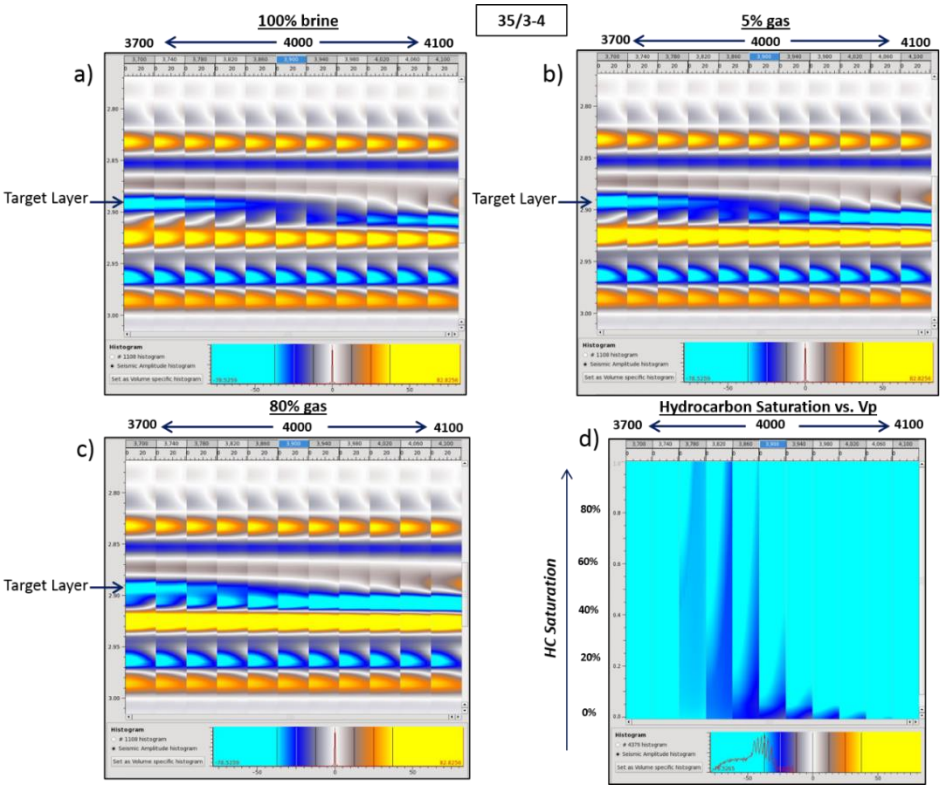

Figure 54: AVA modelling of P-wave velocity (Vp) of the overlying shale vs. gas saturation for the 35/3-4 well.

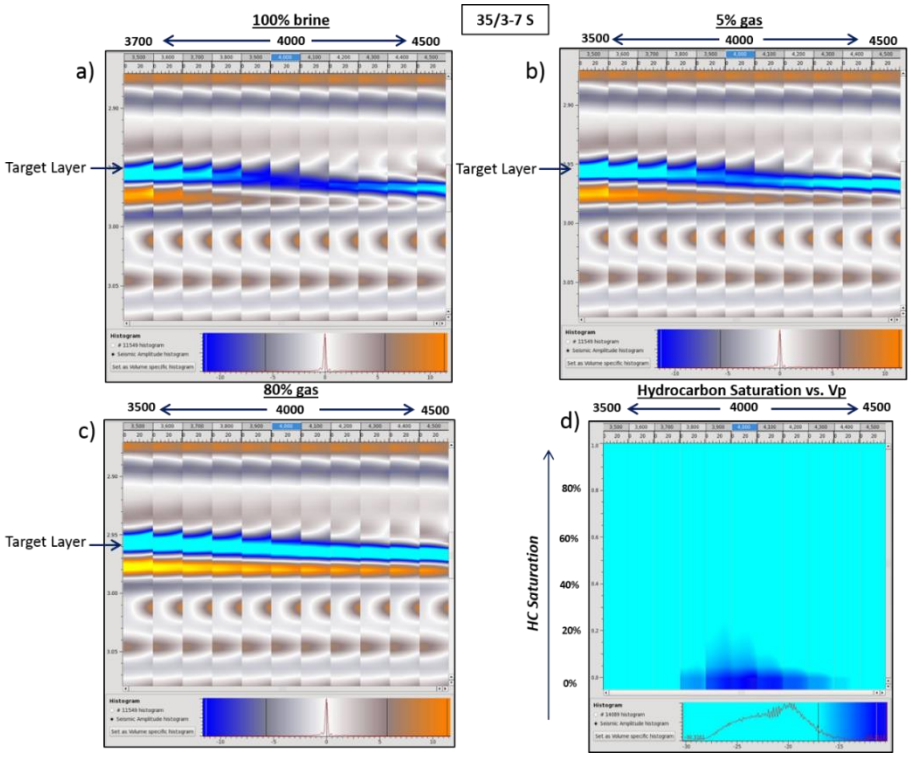

Figure 55: AVA modelling of P-wave velocity (Vp) of the overlying shale vs. gas saturation for the 35/3-7 S well.

Wells 35/3-1 and 35/3-2 both show a polarity reversal when the P-wave velocity of the overlying shale is reduced by 7.5% (300 ms^{-1}), particularly in the brine cases (Figure 53 and Figure 34). This is the same result as observed in section 5.8.2 (Figure 34 and Figure 35). The 35/3-4 and 35/3-7 S wells, however, show different results that are not yet fully understood. It appears that below 4000 ms^{-1} the amplitudes become increasingly softer (Figure 54 and Figure 55). This is opposite to that observed in wells 35/3-1 and 35/3-2. The reason for this needs further investigation, however it appears that there is interference between the reflector at the target layer and the reflector directly below where tuning appears to occur around 3800 ms^{-1}. This may be causing spurious results in the P-wave velocity cases.

On the other hand, the event immediately below the target layer in the 80% gas case follows the same relationship as the other wells; where the amplitude gets harder with lower *Vp* values and greater with higher *Vp* values. This makes much more sense, as a soft shale should make the reservoir appear “harder”. Given that the 35/3-1 and 35/3-2 show no interference of reflectors and their results are consistent to what was expected they are deemed more reliable.

9.2.3 Mineral Bulk Modulus vs. Hydrocarbon Saturation (Gas Case)

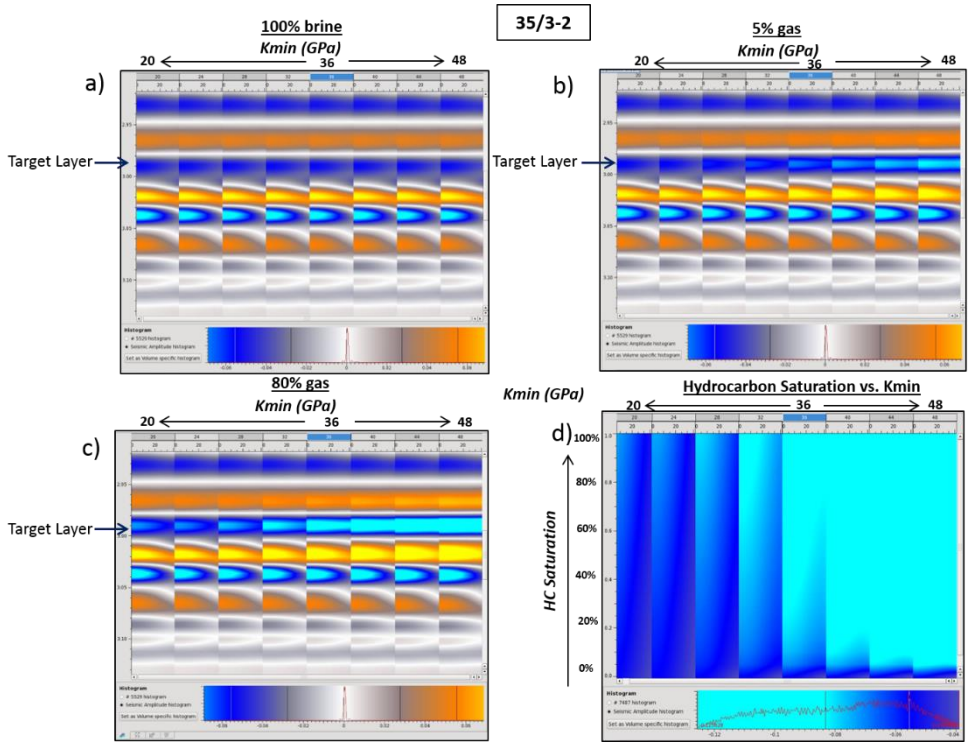

Figure 56: AVA modelling of bulk mineral modulus (Kmin) vs. gas saturation for the 35/3-2 Agat discovery well.

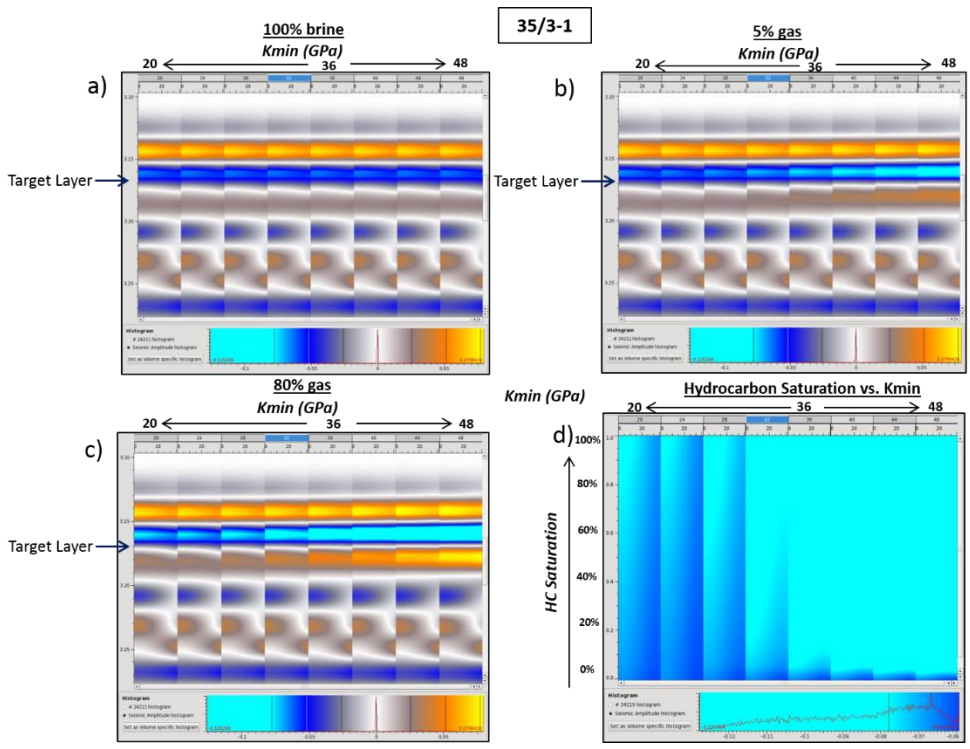

Figure 57: AVA modelling of bulk mineral modulus (Kmin) vs. gas saturation for the 35/3-1 well.

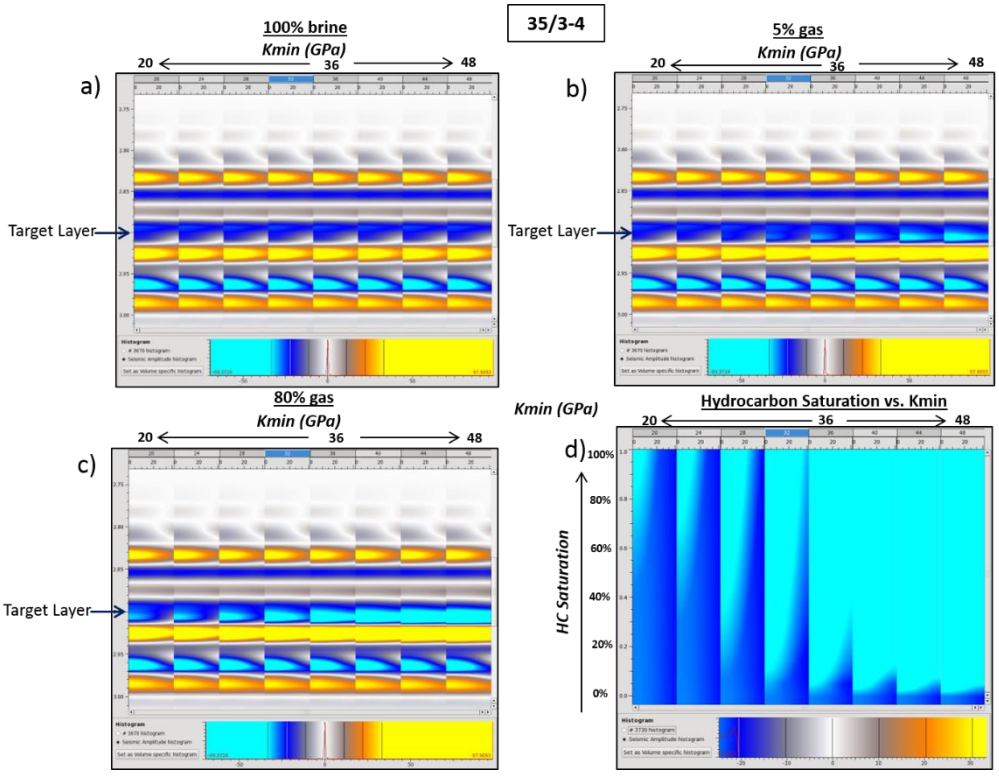

Figure 58: AVA modelling of bulk mineral modulus (Kmin) vs. gas saturation for the 35/3-4 well.

Wells 35/3-1, 35/3-2 and 35/3-4 (Figure 56, Figure 57 and Figure 58) all display consistent results with the results of well 35/3-7 S described in section 5.8.3 (Figure 37 and Figure 38). See section 5.8.3 for a full description.

9.2.4 Porosity vs. Hydrocarbon Saturation (Oil Case)

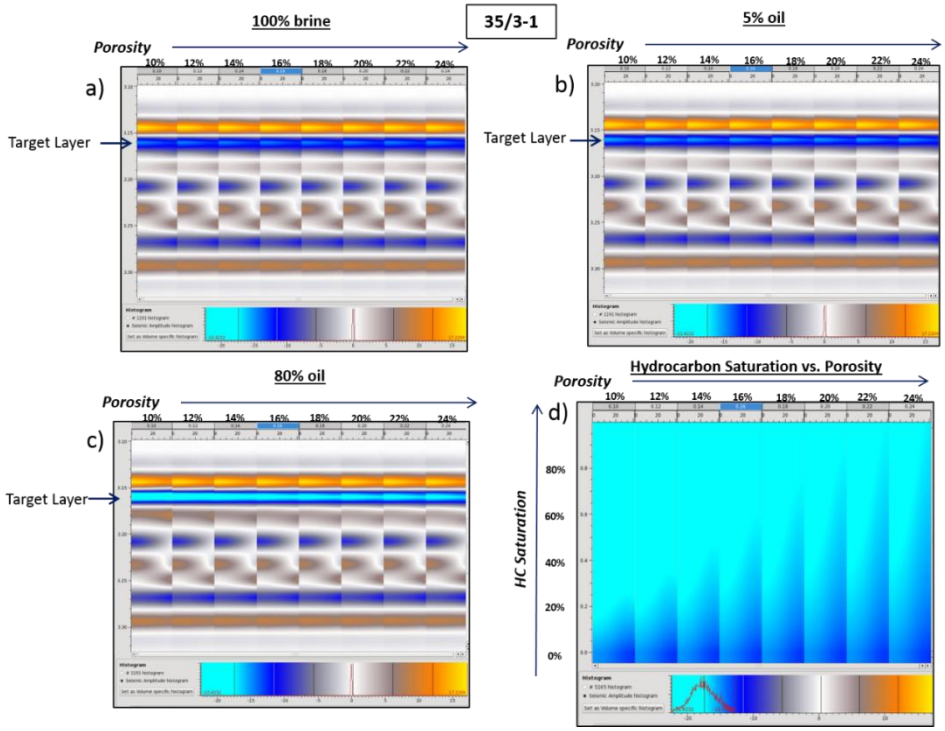

Figure 59: AVA modelling of porosity vs. oil saturation for the 35/3-1 well. a) Brine saturated; b) 5% oil saturated; and c) 80% oil saturated with porosity increasing from left to right. d) Shows a 2D gather map of porosity vs. HC (oil) saturation.

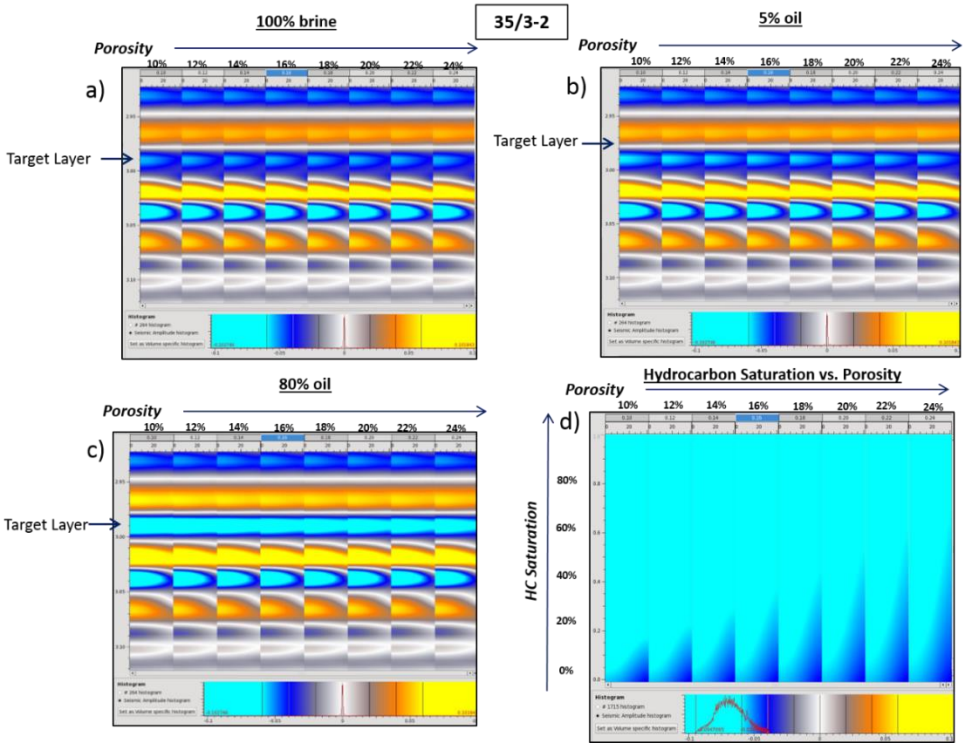

Figure 60: AVA modelling of porosity vs. oil saturation for the 35/3-2 well. a) Brine saturated; b) 5% oil saturated; and c) 80% oil saturated with porosity increasing from left to right. d) Shows a 2D gather map of porosity vs. HC (oil) saturation.

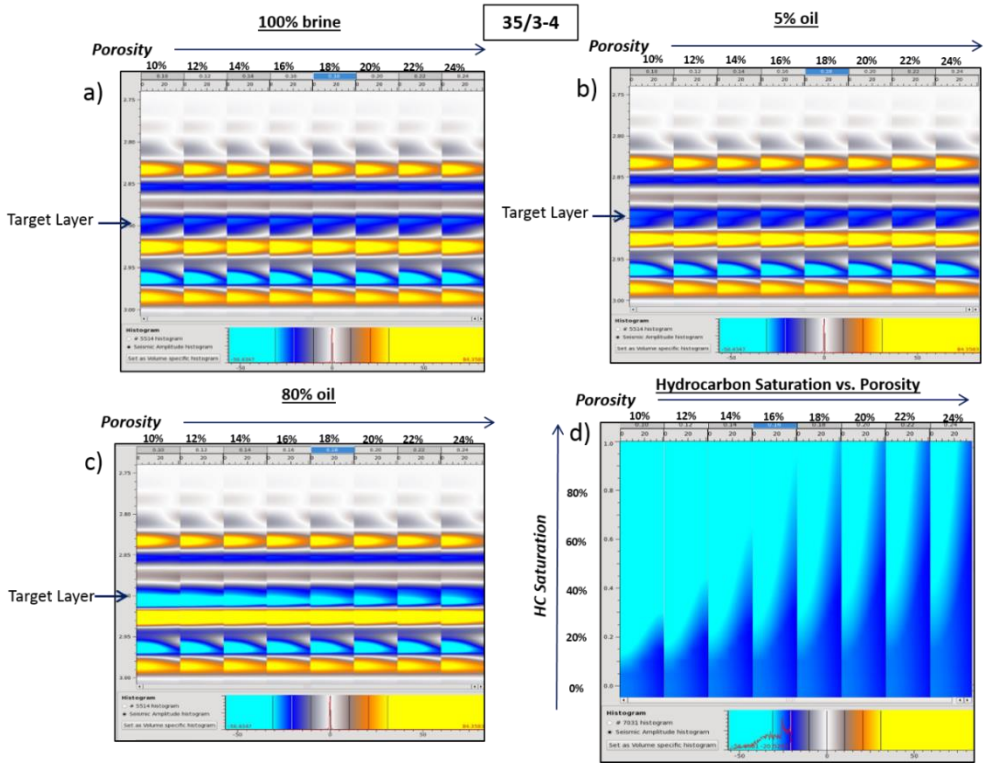

Figure 61: AVA modelling of porosity vs. oil saturation for the 35/3-4 well. a) Brine saturated; b) 5% oil saturated; and c) 80% oil saturated with porosity increasing from left to right. d) Shows a 2D gather map of porosity vs. HC (oil) saturation.

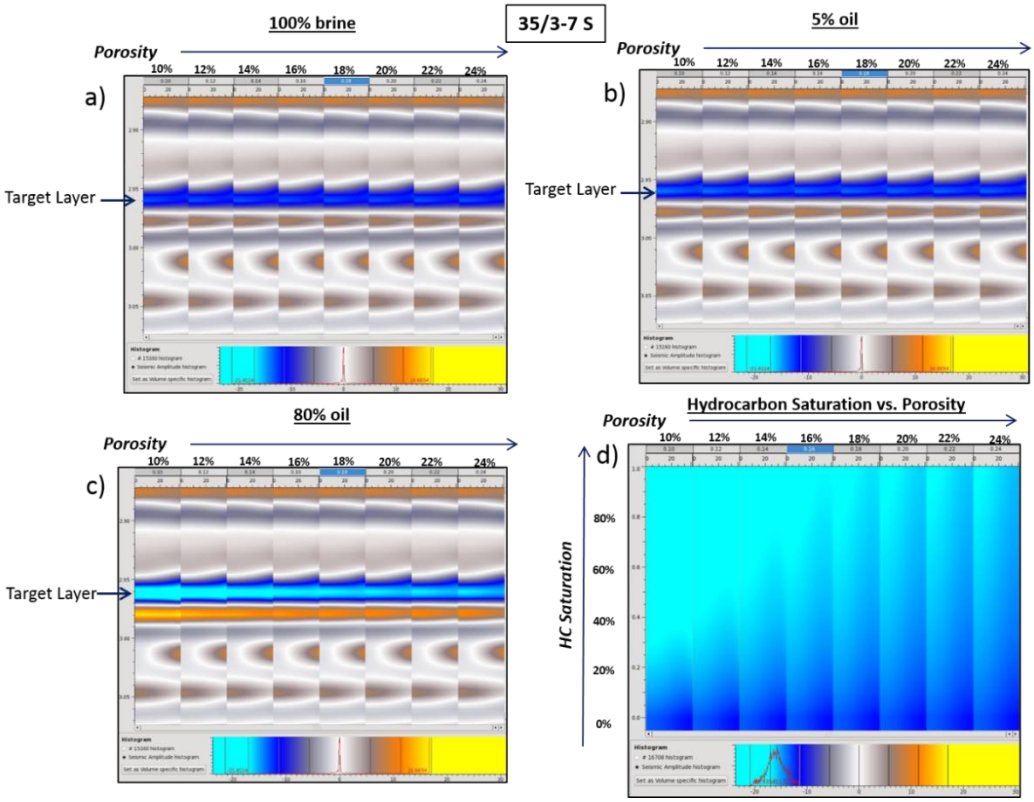

Figure 62: AVA modelling of porosity vs. oil saturation for the 35/3-7 S well. a) Brine saturated; b) 5% oil saturated; and c) 80% oil saturated with porosity increasing from left to right. d) Shows a 2D gather map of porosity vs. HC (oil) saturation.

The oil response for porosity vs. hydrocarbon saturation for all of the studied wells (Figure 59, Figure 60, Figure 61 and Figure 62) show similar effects as the gas responses described previously in section 5.8.1 and 9.2.1. High saturated oil responses give similar increased AVA Class IV effects as described in the high saturated gas scenarios. Brine sands also show little to no amplitude and AVA changes when porosity is varied. This is also consistent with the gas modelled scenarios described previously. Looking at amplitude response alone, it appears difficult to discriminate between oil and gas as both show similar amplitude values.

9.2.5 P-wave velocity vs. Hydrocarbon Saturation (Oil Case)

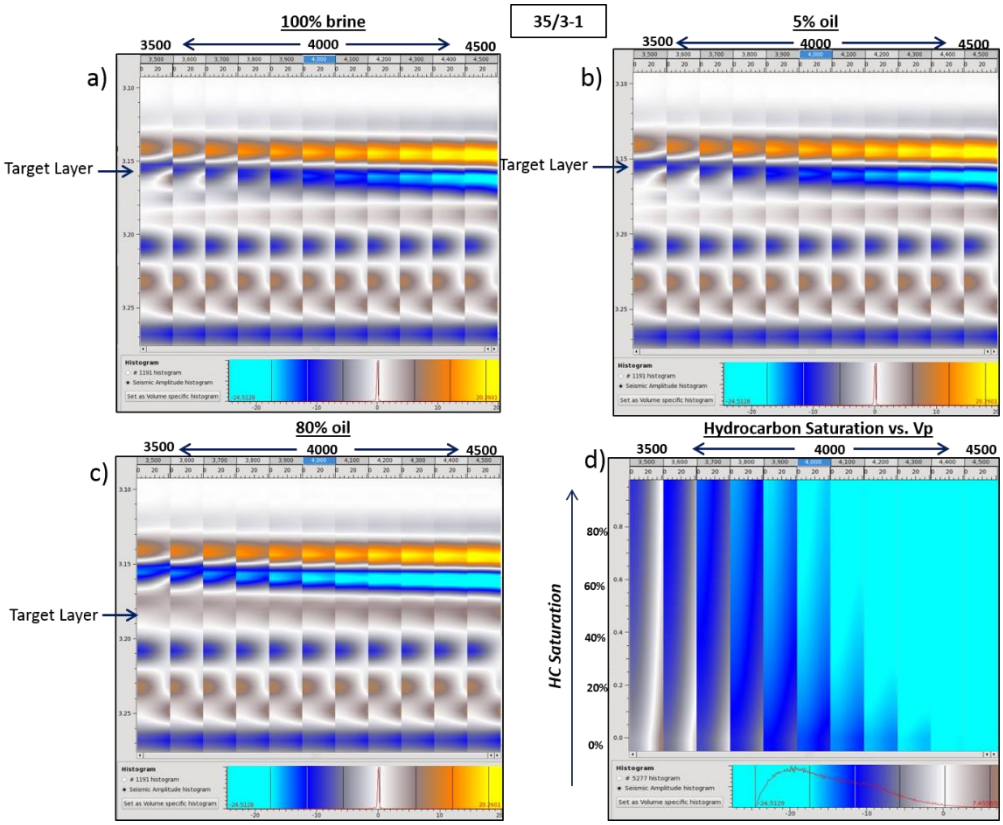

Figure 63: AVA modelling of P-wave velocity (Vp) of the overlying shale vs. oil saturation for the 35/1 well.

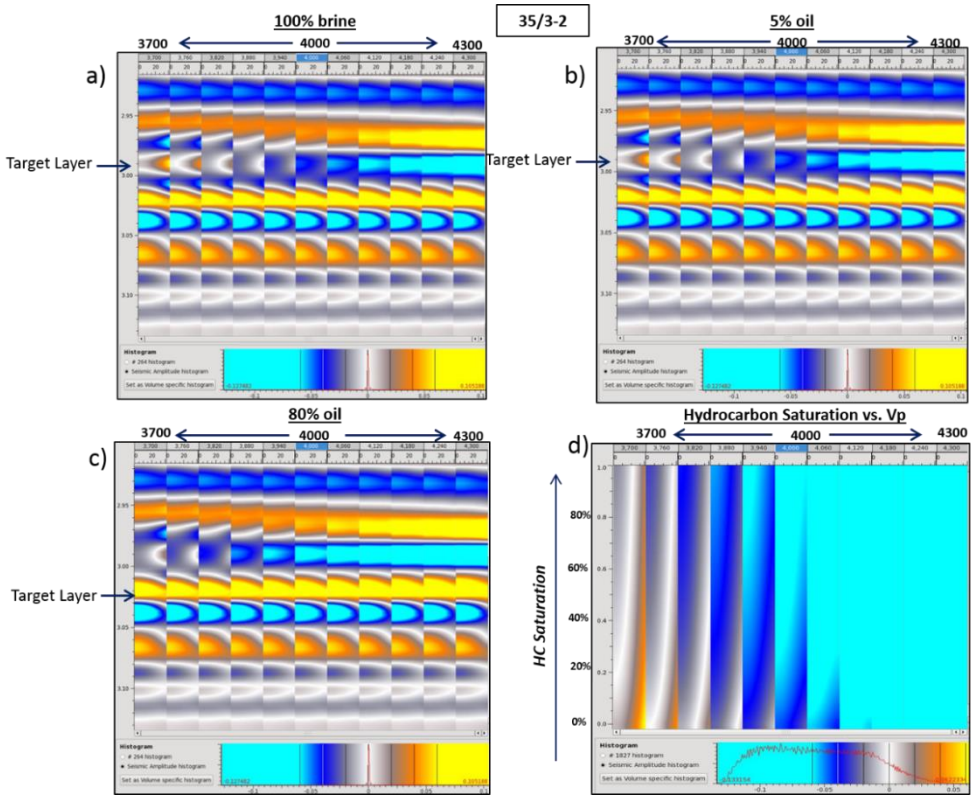

Figure 64: AVA modelling of P-wave velocity (Vp) of the overlying shale vs. oil saturation for the 35/3-2 Agat discovery well.

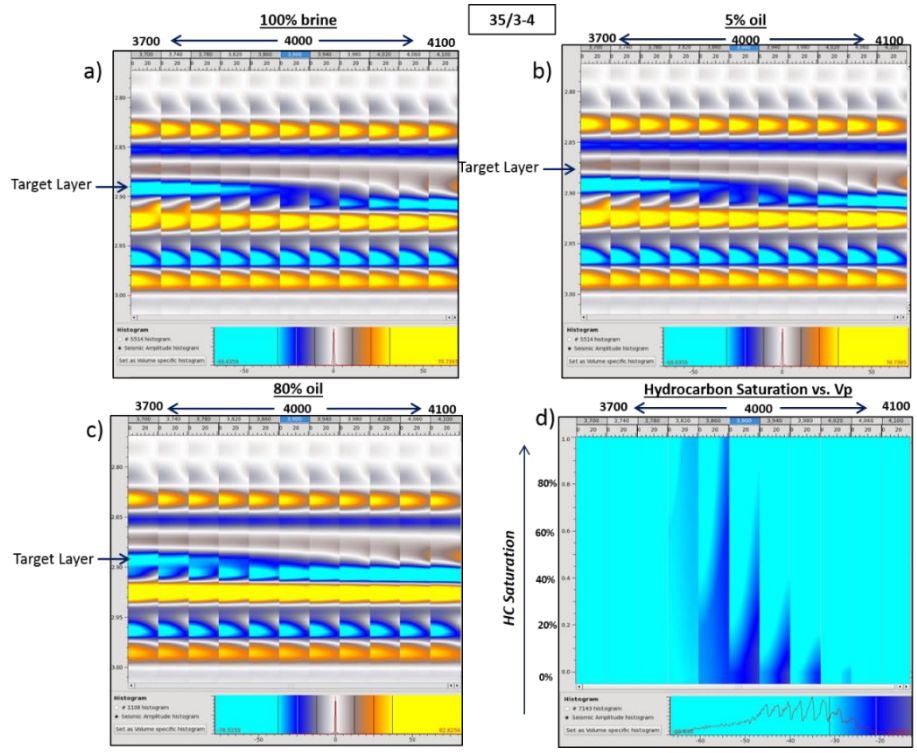

Figure 65: AVA modelling of P-wave velocity (Vp) of the overlying shale vs. oil saturation for the 35/3-4 well.

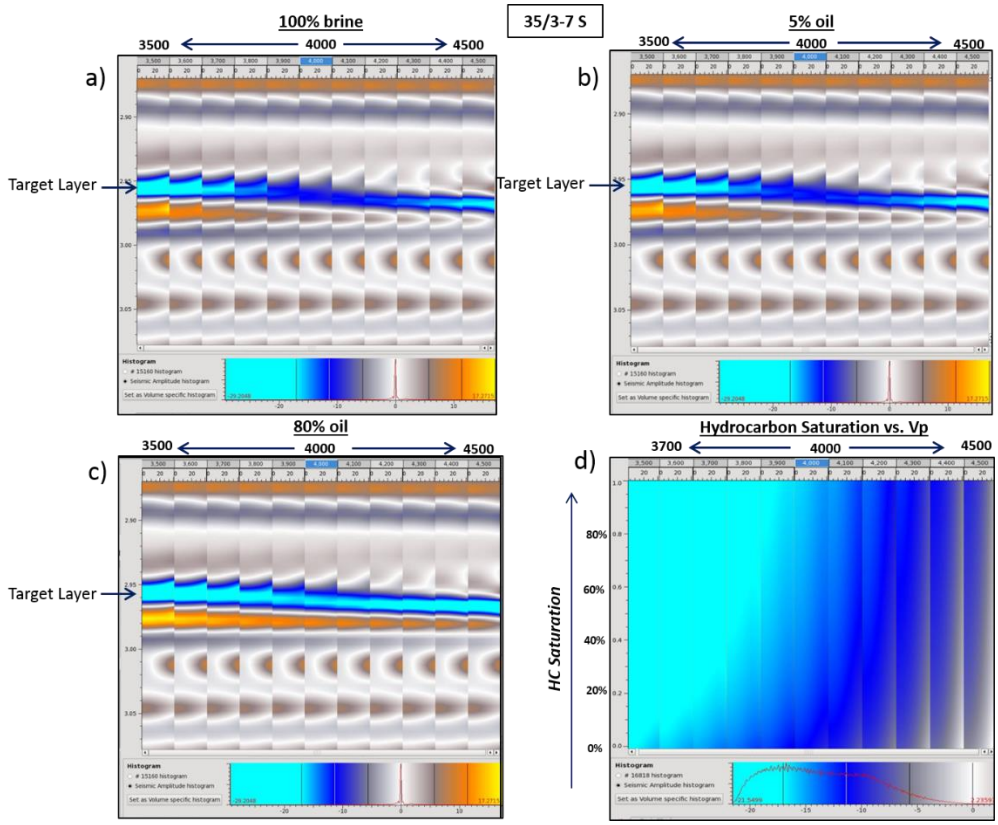

Figure 66: AVA modelling of P-wave velocity (Vp) of the overlying shale vs. oil saturation for the 35/3-7 S discovery well.

The oil response for all of the studied wells (Figure 63, Figure 64, Figure 65 and Figure 66) show similar effects as the gas responses described previously in section 5.8.2. Polarity reversals are evident in the 35/3-1 and 35/3-2 wells when the P-wave velocity is reduced by only 7.5%.

9.2.6 Mineral Bulk Modulus vs. Hydrocarbon Saturation (Oil Case)

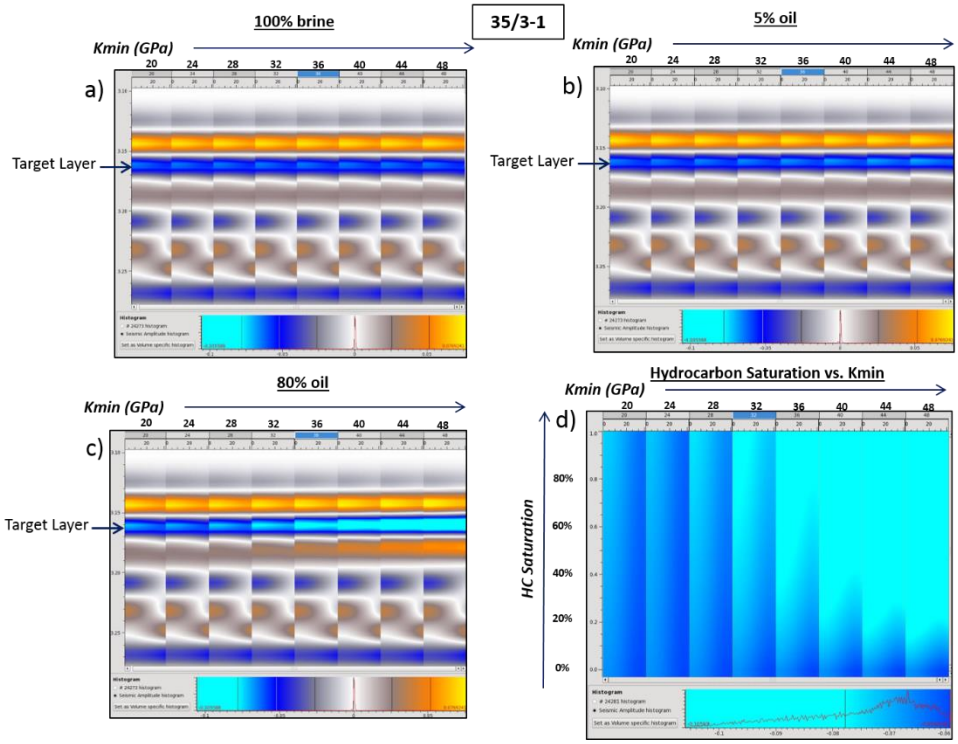

Figure 67: AVA modelling of bulk mineral modulus (Kmin) vs. oil saturation for the 35/3-1 well.

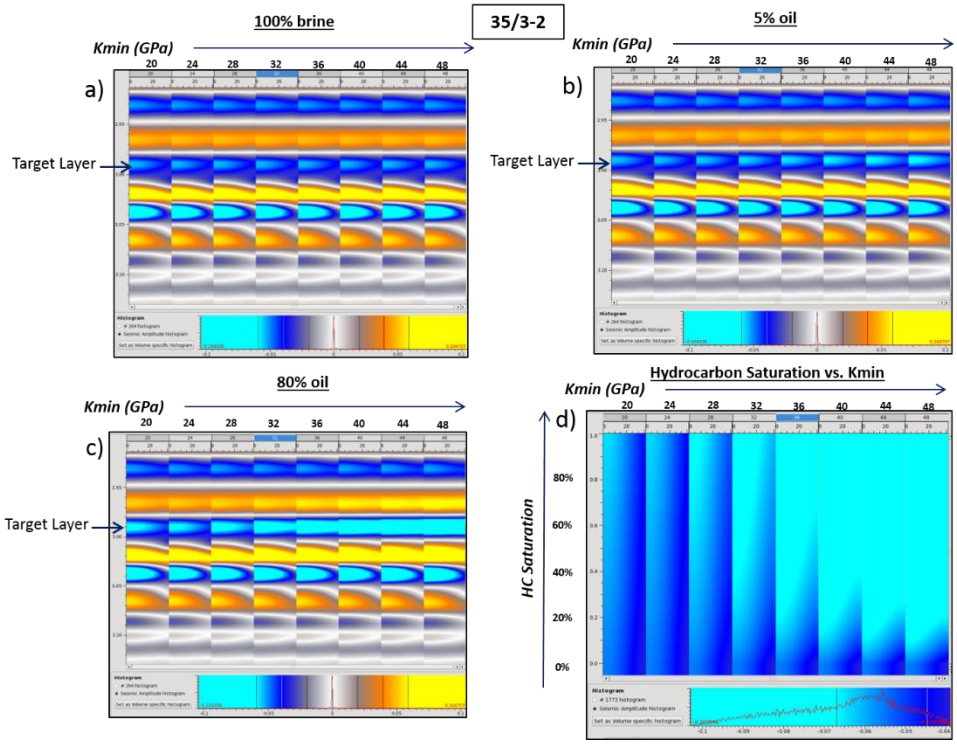

Figure 68: AVA modelling of bulk mineral modulus (Kmin) vs. oil saturation for the 35/3-2 well.

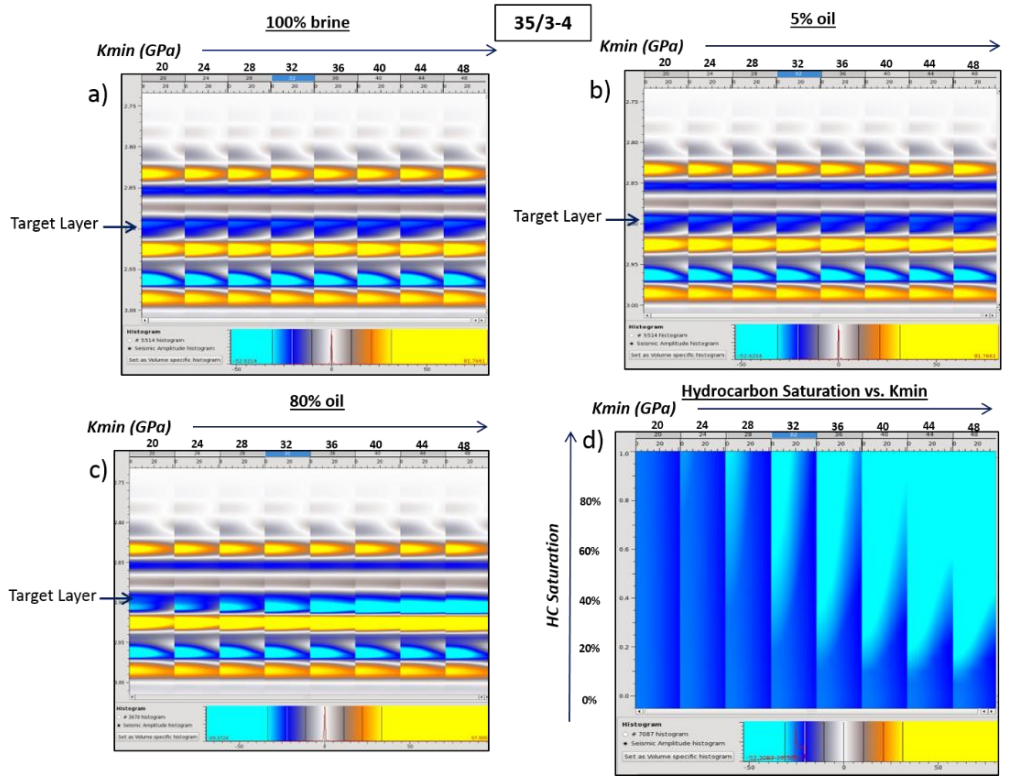

Figure 69: AVA modelling of bulk mineral modulus (Kmin) vs. oil saturation for the 35/3-4 well.

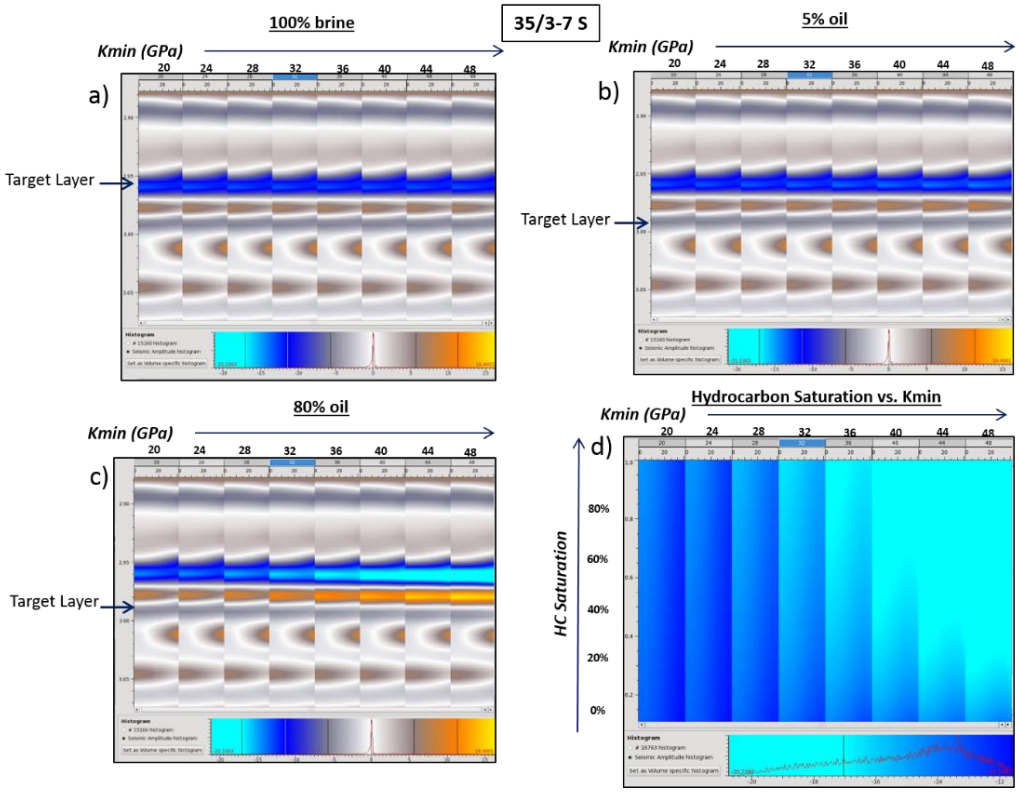

Figure 70: AVA modelling of bulk mineral modulus (Kmin) vs. oil saturation for the 35/3-7 S well.

The oil response for all of the studied wells (Figure 67, Figure 68, Figure 69 and Figure 70) show similar effects as the gas responses described previously in section 5.8.3 and 9.2.3.

9.2.7 Thickness vs. Hydrocarbon saturation (Oil Case)

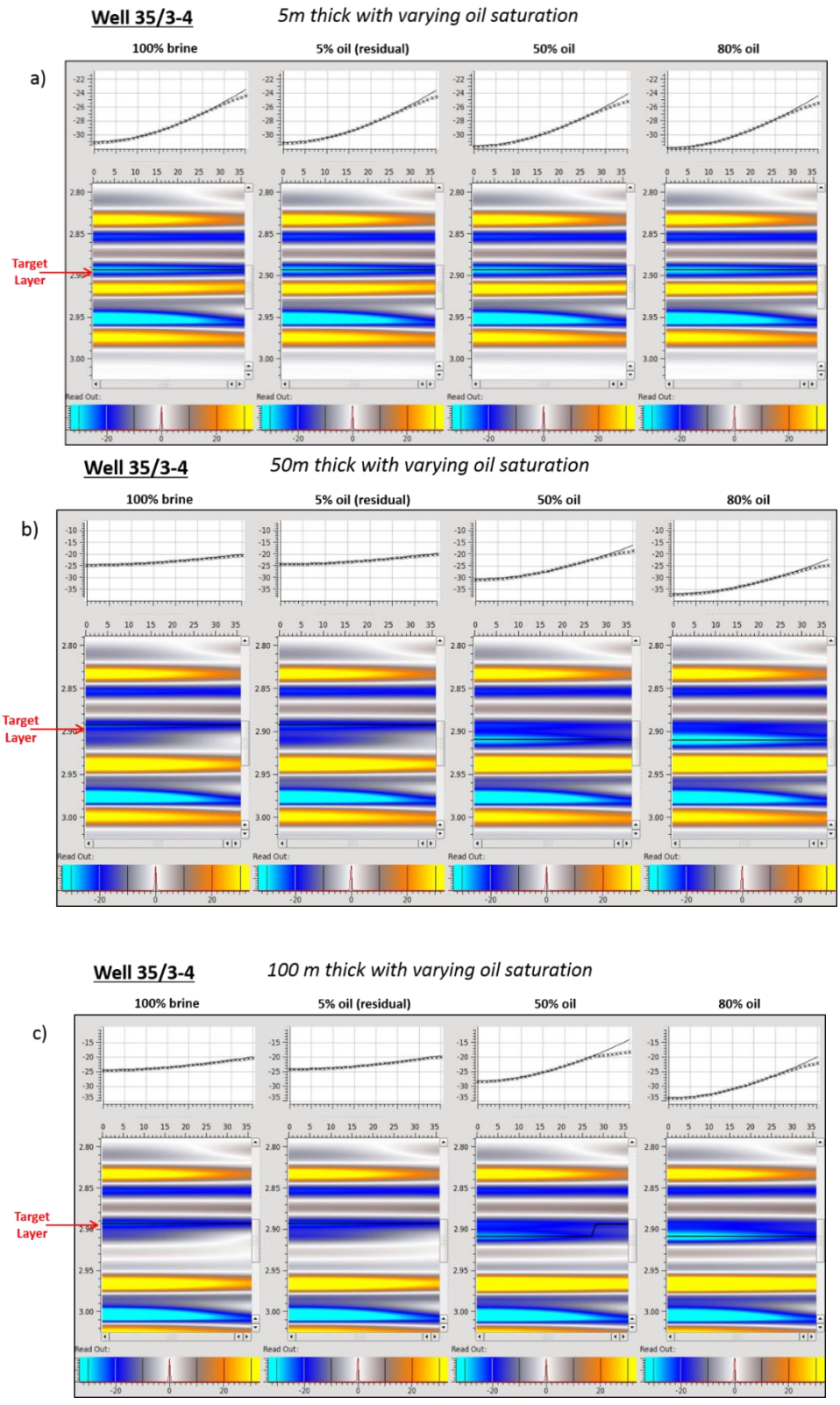

Figure 71: Agat thickness versus hydrocarbon (oil) saturation AVA modelling for the 35/3-4 well. a) 5 m thick; b) 50 m thick; and c) 100 m thick modelled Agat Formation's. 100% brine to 80% oil saturated scenarios are displayed from left to right.

Figure 71 above shows the oil response for the 35/3-4 well, where all thicknesses show a Class IV AVA character as demonstrated by the AVA plots. This shows the same relationship as the gas case described in section 5.8.4. Therefore, the reader is referred to section 5.8.4 for further explanation. The same is also true for Figure 72 below.

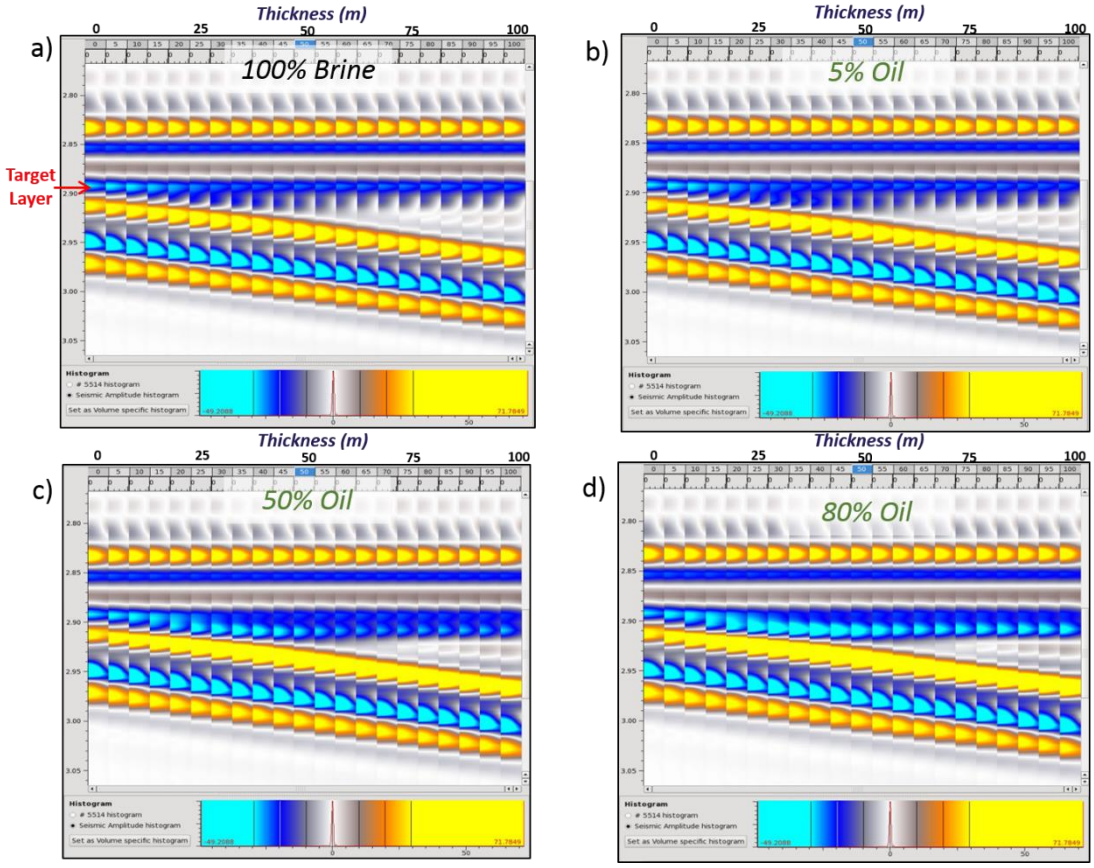

Figure 72: Wedge Modelling of the Agat 80 Member in well 35/3-4 from 100% brine to 80% oil saturations.